1-1-2017

Analysis of Near-Surface Relative Humidity in a Wind Turbine Array Boundary Layer Using an Instrumented Unmanned Aerial System and Large-Eddy Simulation

Kevin Allan Adkins

Recommended Citation

Adkins, Kevin Allan, "Analysis of Near-Surface Relative Humidity in a Wind Turbine Array Boundary Layer Using an Instrumented Unmanned Aerial System and Large-Eddy Simulation" (2017). *Theses and Dissertations*. 649.
https://scholarsjunction.msstate.edu/td/649

Analysis of near-surface relative humidity in a wind turbine array boundary layer using an instrumented unmanned aerial system and large-eddy simulation

By

Kevin Allan Adkins

A Dissertation
Submitted to the Faculty of
Mississippi State University
in Partial Fulfillment of the Requirements
for the Degree of Doctor of Philosophy
in the Department of Aerospace Engineering

Mississippi State, Mississippi

August 2017

Analysis of near-surface relative humidity in a wind turbine array boundary layer using an instrumented unmanned aerial system and large-eddy simulation

By

Kevin Allan Adkins

Approved:

Adrian Sescu
(Major Professor)

David S. Thompson
(Committee Member)

Manav Bhatia
(Committee Member)

J. Mark Janus
(Committee Member/Graduate Coordinator)

Jason M. Keith
Dean
Bagley College of Engineering

Name: Kevin Allan Adkins

Date of Degree: August 11, 2017

Institution: Mississippi State University

Major Field: Engineering

Major Professor: Adrian Sescu

Title of Study: Analysis of near-surface relative humidity in a wind turbine array boundary layer using an instrumented unmanned aerial system and large-eddy simulation

Pages in Study: 153

Candidate for Degree of Doctor of Philosophy

Previous simulations have shown that wind farms have an impact on the near-surface atmospheric boundary layer (ABL) as turbulent wakes generated by the turbines enhance vertical mixing of momentum, heat and moisture. These changes alter downstream atmospheric properties. With the exception of a few observational data sets that focus on the impact to near-surface temperature within wind farms, little to no observational evidence exists with respect to vertical mixing. These few experimental studies also lack high spatial resolution due to their use of a limited number of meteorological sensors or remote sensing techniques. This study utilizes an instrumented small unmanned aerial system (sUAS) to gather high resolution in-situ field measurements from two state-of-the-art Midwest wind farms in order to differentially map downstream changes to relative humidity. These measurements are complemented by numerical experiments conducted using large eddy simulation (LES). Observations and numerical predictions are in good general agreement around a single wind turbine and show that downstream relative humidity is altered in the vertical, lateral, and downstream directions. A suite of LES is then performed to determine the effect of a turbine array on the relative humidity distribution in compounding wakes. In stable and neutral conditions, and in the presence of a positive relative humidity lapse rate, it is found that the humidity decreases below the turbine hub height and increases above the hub height. As the array is transitioned, the magnitude of change increases, differentially grows on the left-hand and right-hand side of the wake, and move slightly upward with downstream distance. In unstable conditions, the magnitude of near-surface decrease in relative humidity is a full order of magnitude smaller than that observed in a stable atmospheric regime.

DEDICATION

I dedicate this work to my family, friends and many teachers along the way. I owe a special debt of gratitude to my parents, Larry and Kitty Adkins, who always taught me to believe in myself and instilled in me the belief that I can accomplish anything. To my wife, Jennifer, thank you for your continued support, encouragement and belief in me during this long journey. To my daughters, Maya and Julia, you are each the most special gifts that I have ever received and it is my hope that this work inspires both of you to pursue your dreams, however daunting they may seem.

ACKNOWLEDGEMENTS

I would like to express my sincere thanks to my major professor, Dr. Adrian Sescu, whose patient approach and guidance throughout my formal coursework and dissertation process has been of immeasurable value. In addition, I would like to thank my committee members, Dr. Mark Janus, Dr. David Thompson, and Dr. Manav Bhatia, for taking time out of their busy schedules and providing additional guidance and invaluable feedback.

Conducting the experimental measurements contained within this work required the assistance of several individuals during the preparation and execution of the field campaign. Specifically, I would like to thank Joshua Olds and Charles Ellis for their assistance during both phases.

Finally, I would like to thank Embry-Riddle Aeronautical University for their continued support, especially that of Dr. Dan Macchiarella, Dr. Leo Murphy, and Professor Colleen Conklin.

TABLE OF CONTENTS

CHAPTER

APPENDIX

LIST OF TABLES

LIST OF FIGURES

LIST OF ACRONYMS

ABL:	Atmospheric boundary layer
ADM:	Actuator disc method
ADM-R:	Actuator disc method with rotation
AGL:	Above ground level
CFR:	Code of federal regulations
COA:	Certificate of authorization
CS:	Control station
CWEX:	Crop/wind-energy experiment
DALR:	Dry adiabatic lapse rate
DGPS:	Digital global positioning system
DNS:	Direct numerical simulation
DOE:	U.S. Department of Energy
FAA:	Federal Aviation Administration
FAR:	Federal Aviation Regulation
GCM:	Global climate model or General circulation model
GCS:	Ground control station
GE:	General Electric
GPS:	U.S. global positioning system
HDOP:	Horizontal dilution of precision

IEO2016:	International Energy Outlook 2016
LES:	Large-eddy simulation
LST:	Land surface temperature
MPI:	Message passing interface
MSL:	Mean sea-level
MW:	Megawatt
NMEA:	National Marine Electronics Association
NOTAM:	Notices to airman
NWP:	Numerical weather prediction
PIC:	Pilot in command
RAMS:	Regional atmospheric modeling system
RANS:	Reynolds-averaged Navier Stokes
R/C:	Remote controlled
RTD:	Resistor temperature detector
SBL:	Stable boundary layer
SGS:	Subgrid-scale
sUAS:	Small unmanned aerial system
TFR:	Temporary flight restriction
TKE:	Turbulent kinetic energy
UA:	Unmanned aircraft
UAS:	Unmanned aerial system
UAV:	Unmanned aerial vehicle
USI:	Unmanned Safety Institute

VFR: Visual flight rules

VLOS: Visual line of sight

VMC: Visual meteorological conditions

VO: Visual observer

WTABL: Wind turbine array boundary layer

LIST OF NOMENCLATURE

A_{rotor}: Rotor swept area

a: Induction factor

C_s: Smagorinsky constant

C_T: Thrust coefficient

C_T': Modified thrust coefficient

C_P: Power coefficient

C_P': Modified power coefficient

c_L: Lift coefficient

c_D: Drag coefficient

D: Turbine diameter

$\bar{d}$: Mean difference

F_A: Axial force

F_D: Drag force

F_L: Lift force

F_T: Tangential force

F_θ: Temperature forcing term

f_C: Coriolis parameter

F_i: Wind turbine forcing term

g: Acceleration due to gravity

l:	Length scale
L:	Obukhov length
n:	Number of paired observations
p:	Dynamic pressure
q:	Specific humidity
r:	Radial coordinate of blade element
Re:	Reynolds number
S_d:	Standard deviation of the differences
S_{ij}:	Strain-rate tensor
$SE(\bar{d})$:	Standard error of the mean difference
T:	t-statistic
$u_i (i = 1,2,3)$	u, v, w velocity components
u_*	Friction velocity
V_f:	Locally filtered horizontal velocity at first vertical grid point
V_{rel}:	Relative velocity of blade segment
V_{tan}:	Tangential velocity
$w'\theta'$:	Surface heat flux
$x_i (i = 1,2,3)$	x, y, z coordinates (streamwise, lateral, vertical)
z_0:	Roughness length
δ:	Kronecker delta
Δ:	Filter width
Δr:	Annulus spanwise width
ε:	Alternating unit tensor

κ: von Karman constant (0.4)

Ψ_H: Heat flux stability correction function

Ψ_M: Momentum stability correction function

π: SGS flux of heat/humidity

ρ: Air density

φ: Scalar quantity or the Angle between the rotor plane and flow velocity

θ: Potential temperature

θ_0: Reference potential temperature

θ_s: Surface potential temperature

τ: SGS Reynolds stress

ν_T: Eddy viscosity

~: Spatial filtering

$(\overline{\ \ })$: Time averaging

$< >$: Horizontal average

$< >_d$: Disk average

CHAPTER I

INTRODUCTION

1.1 Background

In 2008, the U.S. Department of Energy (DOE) issued a report [1] that laid out a vision for 20% of the nation's electricity supply to be fulfilled by wind energy by the year 2030. A 2015 DOE update [2] to this report demonstrated the viability of wind power supplying 10% of the nation's electricity supply in 2020, 20% in 2030, and 35% in 2050. In May 2016, the U.S. Energy Information Administration issued their *International Energy Outlook 2016* (IEO2016) [3] for international energy markets through 2040. The IEO2016 reference case forecasts that the total world energy consumption will increase by 48% from 2012 to 2040. The report documents that non-hydropower renewables accounted for 5% of total world electricity generation in 2012 and prognosticates that it will grow to supply 14% of the increased electricity demand in 2040, with much of the growth coming from wind power. Most recently, on June 29, 2016, in Ottawa, Canada, leaders from the United States, Canada, and Mexico pledged their commitment to the North American continent receiving 50% of its electricity supply from clean energy sources by 2025 [4]. In addition, the cost of wind based generation has dropped by 30% since 2013 while the capacity factor of wind turbines doubled from 25% to 50% in the last decade [5]. These technology improvements, coupled with the DOE's strategic vision, and the commitment of the world's industrialized nations to increase their renewable energy capacity ensures that the number and size of wind farms will continue to increase.

1.1.1 Wind Energy and the Atmospheric Boundary Layer

The atmospheric boundary layer (ABL) is the portion of the troposphere that is directly influenced by the presence of the earth's surface and responds to surface forcings with a timescale of approximately one hour or less [6]. This lowest level of the atmosphere, with the Earth's surface as a boundary, is a spatially and temporally dynamic region with a variety of scales of motion. Exchanges of sensible heat and humidity between the ground and the overlying layers directly impact near-surface atmospheric conditions, which in turn may affect the conditions in the entire ABL and modify the entrainment from layers above [7]. Observations and numerical simulations have shown that wakes generated within large wind farms can play a major role in these exchanges.

Turbulent wakes are generated as a wind turbine extracts kinetic energy from the wind and converts it into rotational energy. Experimental measurement and numerical simulations have shown that these wakes modify surface temperatures and land-atmosphere exchanges [8], [9]. With the present and planned growth of wind energy, these modifications, and their impact on the lowest layer of the atmosphere that serves as host to almost all human activity, needs to be more thoroughly investigated and understood. Wind turbine wakes have been shown to bring about changes to both the dynamic and thermal properties of the ABL [10], [11], [12], [13]. Evidence of changes to near-surface temperatures, via mesoscale modeling [14], in-situ measurement [15], and remote sensing [16] have also been shown to change the mean wind speed, potential temperature profile, and surface fluxes [17], [18], [19].

1.2 Previous Research

Even with the widespread deployment of wind turbines, their influence on near-surface meteorology has only begun to be investigated. A brief summary of the various approaches found in the literature are detailed in this section.

1.2.1 Numerical Modeling and Simulation

With the present and planned growth of wind energy, and the consequential deployment of a large number of wind turbines, studies have investigated the climatic impact resulting from large-scale wind power development [20], [21], [22], [23]. Each of these studies utilized a global climate model (GCM), with the wind turbines parameterized as either a combined momentum sink and source of turbulent kinetic energy (TKE) or, alternatively, as surface roughness elements. These parameterizations were implemented to analyze the impact of regional to continental scale deployment of high density wind turbine arrays. Climatic changes were minimal for spatial scales exceeding that of the wind turbine array with any appreciable change effectively confined to within the array. Near-surface temperature changes within the wind farm were less than or equal to one degree Kelvin while more pronounced differences, as would be expected, were observed for flow characteristics such as wind speed and turbulence. Results from these models ultimately depend on the fidelity of the model, including the ocean model, and of the simulated wind turbines. Consequently, several of these studies have further work planned to update these results with future model enhancements and more realistic parameterizations.

Mesoscale models, such as the Regional Atmospheric Modeling System (RAMS), have also been used to study the impact of wind farms on local meteorology, specifically near-surface temperature, humidity, and surface fluxes of sensible and latent heat [14], [24]. These regional climate models use a subgrid-scale (SGS) rotor parameterization representing the turbine as either a sink of kinetic energy or momentum and a source of TKE. In Roy et al. [14], the regional model was enhanced by the incorporation of an improved rotor parameterization, based on a modern commercial turbine, and the use of archived atmospheric sounding data for initialization. The simulation approximated a 7 x 3 array in the middle of a domain representative of flat terrain at sea-level. The integration of these real-world elements produced (via spatial and temporal averaging) a slight, but statistically significant, warming of near-surface temperatures for a stable atmosphere (where relatively warm air resides above cooler air adjacent to the ground) and a still smaller, but statistically significant, cooling of near-surface temperatures for an unstable atmosphere (where relatively warm air resides below cooler air aloft). The magnitude of the surface temperature change was correlated to the magnitude of the equivalent potential temperature lapse rate, but all temperature changes were well below one degree Kelvin. Humidity changes were assessed by considering the surface total water mixing ratio, which represents the amount of moisture present in each kilogram of dry air. When the ambient mixing ratio lapse rate was negative, indicating an increase in humidity with height, the wind farm had a net moistening of the near-surface air. As the converse also held true, it can be stated that surface humidity showed a statistically significant inverse correlation with the ambient mixing ratio lapse rate. Hence, it was concluded that enhanced vertical mixing delivers relatively moist air downward and relatively dry air upward, leading to an increase in near-surface humidity in the presence of a negative lapse rate. Analogously, a positive ambient mixing ratio lapse rate led to a decrease in near-surface humidity following vertical mixing. The surface sensible heat flux is dependent upon the temperature gradient between the ground and near-surface air. Similarly, the surface latent heat flux is dependent upon the moisture gradient between the ground and near-surface air. Fluxes of sensible and latent heat are therefore affected by changes to near-surface air temperature and humidity. Consequently, mesoscale models have shown that a wind farm's effect on near-surface temperature also brings about changes to the near-surface sensible heat flux, and a wind farm's effect on near-surface moisture also brings about changes to the near-surface latent heat flux.

Parameterizing the wind turbines within the domain as a kinetic energy sink and TKE source, Baidya Roy et al. [24] first put forth that the aforementioned effects on near-surface temperature and moisture are brought about by the turbulence produced by the parameterization scheme. The turbulent wake of wind turbine rotors, consisting of eddies of several different length scales, enhance vertical mixing. Consequently, in a stable boundary layer (SBL) turbulent eddies serve to mix warm air downward and cooler air upward. This dynamic results in a warming of near-surface temperatures. Analogously, in an unstable atmosphere, enhanced vertical mixing delivers cooler air downward while mixing warmer air upward. While this dynamic will result in cooler near-surface temperatures, the decrease in near-surface temperatures was noted to be more muted, presumably due to the already well-mixed nature of an unstable environment.

A very popular tool, utilized to quantify the changes that occur within the wind turbine array boundary layer (WTABL), is large eddy simulation (LES). In LES, the largest turbulent eddies are resolved (explicitly computed) while smaller scales of motion, not resolved by the grid, are modeled [25]. With a smaller cut-off length scale for modeling, LES provides higher spatial and temporal resolution of the structure and dynamics of the flow within the WTABL compared to global and regional scale models. Therefore, LES, with its increased capability to simulate and highly-resolve the flow through the WTABL, possesses the ability to provide additional insight into the impact of wind farms on local meteorology. Temperature and velocity fields within turbine wakes, in a stably stratified ABL, have been investigated using LES [26]. Results agree with lower-resolution model studies that show how enhanced vertical mixing lowers the temperature above the rotor turbine top tip height and increases the temperature below the rotor turbine bottom tip height. In a LES investigation, neglecting stratification effects and specifically aimed at determining whether surface scalar fluxes change in the presence of wind turbines, results showed an overall increase in scalar fluxes on the order of 10%-15% within a fully developed WTABL [17].

Alternatively, LES has been used extensively to investigate the effect of the environment on the WTABL. Since the extraction of kinetic energy from the upstream flow is used to produce electricity, downstream wake recovery is an important issue in the development of large turbine arrays. LES has shown that higher levels of upstream turbulence intensity aid in the recovery of wakes and moves the location of peak turbulence intensity and turbulent shear stress closer to the turbine [27]. Large wind farms rely on the entrainment of kinetic energy from surrounding higher-velocity flow for faster wake recovery. LES has been used to investigate the influence of atmospheric stability on entrainment and pointed toward stable atmospheric scenarios leading to reduced entrainment [28] and longer downstream velocity deficits [29]. Alternatively, simulations point toward a weaker inversion strength or height [30], or increased positive buoyancy [31], increasing the entrainment rate and shortening the wake recovery. LES numerical experiments have also been utilized to explore the role of large-scale flow structures within the turbulent wake in entrainment [32]. Such numerical experiments have also demonstrated how synthetic downward forcing of high velocity flow at upstream wind turbines can enhance kinetic energy entrainment and power extraction [33].

1.2.2 Measurement

Numerical simulation has been the predominate means for the investigation of wind farm impacts to local meteorology. Observational data sets are therefore needed in order to further inform the impact of wind farms on local meteorology. These data sets, besides being a direct measurement of the environment, serve as a check on model and simulation output and act as a basis to further enhance these models and simulations.

A pioneering field campaign in 1989 collected temperature measurements within a wind farm at San Gorgonio, California [34]. Near-surface temperatures exhibited similar trends to the aforementioned simulations that showed nocturnal and early morning warming and cooler surface temperatures during daytime hours. Vertical temperature profiles that were gathered simultaneously further showed that, similar to numerical simulations, near-surface warming coincided with stable conditions and cooling was associated with an unstable atmosphere. Although these early observations reinforce a consistent trend, it is noted that these observations were gathered from a forty-one row wind farm located in mountainous terrain and composed of 23 meter tall turbines with 8.5 meter rotor blades. These turbines, very small by today's standards, were sited with a relatively close spacing of 120 meters.

In-situ vertical measurements of potential temperature were also undertaken during the spring of 2012 at a Midwest utility-scale wind farm sited on flat, homogeneous terrain covered by soy and corn crops [15]. While no discernible change to the potential temperature gradient was identified over the course of daytime measurements, the vertical gradient decreased at night. In particular, the authors noted that this change was brought about largely by the rise of temperatures at 2 meters while hub height values remained relatively consistent.

During the summers of 2010 and 2011, Crop/Wind-energy Experiment (CWEX) 2010 (CWEX10) and Crop/Wind-energy Experiment 2011 (CWEX11) took place in Iowa at a utility-scale wind farm located within an agricultural context. This Midwest site offered similar cultivar type but variability in soil type and moisture content did exist within the measurement domain. During the CWEX11 field campaign, leaf wetness sensors were utilized to study changes to dew duration in the wakes of wind turbines [35]. Since high humidity and stable conditions are conducive to the formation of dew, the measurement of dew duration provides another means to study how wind farms lead to the alteration of local meteorological conditions. A lack of robust data only led to conditional support that dew duration is shortened in the wake of a wind turbine. This conditional conclusion may lend support to the theory that wind farms decrease near-surface humidity. Temperature measurements mirrored the trend of earlier investigations and showed that wind turbines cause negligible changes to daytime (well-mixed) near-surface values, but cause substantial increases, of the order of 1.0-1.5 Kelvin, to overnight (stratified) readings [36].

In support of atmospheric measurement and observation coursework, researchers undertook a field campaign to measure temperature, atmospheric pressure, wind speed, wind direction, relative humidity and evaporation at five different weather instrument clusters positioned around, and within, an Indiana wind farm [37]. Four instrument clusters were arranged to scribe a square around a large array of wind turbines, with the fifth cluster roughly centered and situated approximately 4,500 meters away from each corner. Instrument biases between the center cluster and the four peripheral instrument stations were acknowledged, but not quantified. However, nocturnal and early morning warming, along with daytime cooling, consistent with other experimental measurement and numerical studies, was suggested. Additionally, evidence that air dried as it transited the wind farm, along with an increase in downstream evaporation rates, was established. Due to the sparseness of relevant instrument clusters for any given wind direction, changes to these meteorological parameters lacked good spatial resolution.

With field campaigns being relatively expensive and often times limited in both duration and breadth of measurement, remote sensing techniques have also been employed to compensate for the dearth of in-situ observations. Satellite data has been analyzed over multiple years and seasons to assess how operational wind farms modify land surface temperatures (LST). With a resolution as fine as 120m, adjacent land pixels, with and without wind turbines, have been compared [38], [39], along with an analysis of LSTs of geography before and after wind turbine deployment [16], [40]. Each method has demonstrated a downwind nocturnal warming trend. This trend was universally found during the warm season, with only one study [16] failing to find evidence of this warming during the December to February time frame. With no evidence of large wind turbine arrays impacting daytime temperatures, remotely sensed nocturnal temperature increases were under one degree Celsius.

1.2.3 The Use of UAS in Boundary Layer and Wind Energy Research

Remote controlled (R/C) aircraft were utilized for atmospheric observations as early as 1970. In a study by Konrad et al. [41], for example, the aircraft was equipped to record airspeed, vertical speed, dry- and wet-bulb temperatures, pressure and relative humidity. The need for continuous piloting, and the accompanying inherent flight path imprecision, along with clunky flight systems and meteorological sensors, stymied the widespread feasibility of remotely piloted aircraft in field campaigns. Subsequent development of the global positioning system (GPS), advancements in integrated circuits and battery technology, and the miniaturization of aircraft systems has now led to the proliferation of small and affordable unmanned aerial systems (UAS). Commonly referred to as a drone, a UAS is a system comprised of a number of sub-systems to include the air vehicle (often called an unmanned aerial vehicle (UAV)), the payload, a control station (CS) (most often a ground control station (GCS)), aircrew, data link, launch and recovery equipment, maintenance and support equipment, and an operational space consisting of rules and regulations [42]. The ready availability of UASs, reductions in the size of environmental sensors, and the creation of a regulatory environment that permits commercial operations (including research), have allowed the potential for using UASs in atmospheric data collection, amongst many other uses [43], [44], [45]. Fixed-wing, versus rotary-wing, UAVs have been the preferred choice to date with early adoption of UASs for ABL and wind energy research taking place abroad [46], [47], [48], [49], [50], [51] and burgeoning use domestically [52] , [53], [54].

A UAS fills an important gap in the suite of instruments available for ABL investigation. Conventional manned aircraft are unable to operate at the lowest levels of the ABL due to a myriad of safety concerns. While meteorological towers can be erected here, and are able to provide high temporal resolution and accuracy, they cannot provide high spatial resolution and have practical height limitations that are well below the height of the ABL. Tethered solutions can only offer skewed single column measurements and similar non-tethered options cannot be precisely controlled. Remote sensing solutions also possess altitude limitations and decreasing resolution with height. As a result of these limitations, none of the aforementioned strategies offer insight into horizontal inhomogeneity or a complete description of the vertical extent of the ABL. Alternatively, a UAS can be precisely controlled to provide horizontally and vertically continuous measurements across vast heights (including the vertical extent of the ABL) and distances conveniently and cost effectively. Infrasonic sensing [55], along with atmospheric sampling of vertical profiles [56], turbulence [51], [57], marine boundary layers [58], [59], sea breezes [60], coastal boundaries [61], and temperature fluctuations, for the assessment of their impact on the propagation of electromagnetic and acoustic waves [54], have all been successfully accomplished with UAS. UAS have also been exploited to evaluate numerical weather prediction (NWP) ABL parameterization schemes [62] and storm forecasting techniques [63], detect underlying surface temperatures [64], investigate the Arctic [65] and Antarctic [66] ABL, and aid in the calculation of sensible and latent heat fluctuations [52].

Multiple studies [67], [68], [69], [70] have demonstrated that in-situ measurements of atmospheric temperature and humidity, via a UAS, are indistinguishable in accuracy relative to ground-based remote sensing techniques and traditional in-situ aerial measurements. Inferred wind velocity, based on GPS ground speed and an assumed constant UAV true airspeed, has been shown to compare favorably to pilot balloon ascents tracked by theodolites. UAS sensed temperature and humidity profiles have been contrasted with radiosonde measurements and have also shown comparable accuracy [67]. Meteorological towers have also been used, along with remote sensing techniques [68], to successfully validate UAS acquired temperature, humidity and wind velocity measurements. D.E. Cook et al. [69] showed that UAS temperature and humidity measurements were equivalent to ground-based weather stations within a 95% confidence level and were statistically indistinguishable from concurrent radiosonde measurements. UAS derived potential virtual temperature data has also been shown to compare well to both tower and radiosonde derived data [70].

The advantages associated with increased spatial coverage and resolution, along with the reduced infrastructure and cost afforded by a UAS when compared to conventional methods, are also beginning to be exploited in wind power meteorology [71], [72]. Exploiting the flexibility and inexpensiveness of a UAS, this platform has been leveraged to explore the upstream flow [73] and detailed near-wake structure [74] of wind turbines. Atmospheric turbulence within a wind turbine array impacts turbine loads and fatigue, downstream flow recovery, and thus, wind farm layout and productivity. As a result, UASs are also being utilized to investigate the structure of downstream turbulence in wind farms [75], [76].

CHAPTER II

OBJECTIVES

2.1 Research Motivation

In numerical investigations using a mesoscale model, Roy et al. [8], [13] found that wind farms alter near-surface air temperature and humidity and, in doing so, also affect surface sensible and latent heat fluxes. Results demonstrate that enhanced vertical mixing of air with different temperatures and moisture content lead to these changes. As an aggregate, model runs initialized with a positive mixing ratio lapse rate exhibit overall downstream near-surface drying, while a negative upstream mixing ratio lapse rate results in general surface moistening.

The spatially and temporally dynamic character of the ABL, and the many scales of motion introduced by the presence of utility-scale wind turbines, ensures that downstream near-surface changes are not spatially uniform. With an absence of higher resolution numerical studies or experimental measurements in the literature, further investigation with increased spatial resolution is required.

2.2 Research Objectives

This research investigates how enhanced vertical mixing, induced by utility-scale wind turbines, alters downstream relative humidity. High resolution in-situ measurements are made with an instrumented small unmanned aerial system (sUAS) within two state-of-the-art wind farms. The experimental set up allows for the changes in relative humidity to be mapped in the near-wake region of a single wind turbine. Vertical, lateral, and downstream flight profiles are executed in the near wake region and compared to upstream values. The suite of absolute temperature and relative humidity profiles is captured in stable, unstable, and neutrally stable atmospheric stability conditions over the course of several days. To complement this mapping, LES is utilized to investigate how compounding wakes, within a 6 x 4 turbine array, contribute to a cumulative change to near-surface values of relative humidity.

> *Motivation and goal of research:* *The primary motivation for this research is to investigate the impact that enhanced mixing, brought about by wind turbines, has on near-surface relative humidity. The principal goal is to map changes in relative humidity with high spatial resolution.*

2.3 Research Execution

2.3.1 Experimental Measurement

In-situ measurements of relative humidity are gathered via an instrumented sUAS in two state-of-the-art Midwest wind farms. Within the experimental campaign:

- Vertical, lateral, and downstream profiles are flown in the near wake region of a utility-scale wind turbine and compared to upstream values.
- The complete suite of profiles are captured in stable, unstable and neutrally stable atmospheric stability conditions over the course of several days.
- Measured values of changes in relative humidity are put forth in the context of an uncertainty analysis.

2.3.2 Numerical Investigation

A large eddy simulation of a single wind turbine and a 6 x 4 wind turbine array is undertaken using fixed inflow profiles for humidity, temperature, and wind speed. Within the numerical simulations:

- The turbine rotor is parameterized using a rotating actuator disk model that is representative of a utility-scale wind turbine.
- Temperature profiles representative of stable, unstable, and neutral stability conditions are used.
- The fixed inflow profile assumes a logarithmic velocity profile and positive specific humidity lapse rate.
- The magnitude of the downstream relative humidity change from a compounding wake is quantitatively analyzed.

2.4 Presentations and Publications

A list of presentations and publications produced by this research is listed below.

2.4.1 Presentations

1. Adkins, K., Sescu, A., and El Fajri, O., “Analysis of near-surface relative humidity in a wind turbine array boundary layer using an instrumented unmanned aerial system and large-eddy simulation,” 69th Annual Meeting of the American Physical Society Division of Fluid Dynamics, Portland, OR, Nov 20-22, 2016.

2. Adkins, K. and Sescu, A., “Observations of near-surface relative humidity in a wind turbine array boundary layer using an instrumented unmanned aerial system,” American Geophysical Union 2016 Fall Meeting, San Francisco, CA, Dec 12-16, 2016.

3. Adkins, K., Olds, J., and Ellis, C., “Development, testing and use of an instrumented unmanned aerial system to investigate changes to the near-surface meteorology within a wind farm,” Association

for Unmanned Vehicle Systems International Xponential 2017, Dallas, TX, May 8-11, 2017. (accepted)

2.4.2 Publications

1. Adkins, K., Sescu, A., "Differential mapping of relative humidity in the near-wake region of a wind turbine using an instrumented unmanned aerial system," Int. J. of Green Energy, under review.

2. Adkins, K., Sescu, A., "Analysis of near-surface relative humidity in a wind turbine array boundary layer using an instrumented unmanned aerial system and large-eddy simulation," Renewable Energy, under review.

3. Adkins, K., Olds, J., and Ellis, C., "Development, testing and use of an instrumented unmanned aerial system to investigate changes to the near-surface meteorology within a wind farm," Proceedings of the Association for Unmanned Vehicle Systems International Xponential 2017, Dallas, TX, May 8-11, 2017. (accepted)

CHAPTER III

METHODOLOGY

3.1 Experimental Campaign

The measurement campaign took place during the period of May 24 – 27, 2016 within two recently developed Midwest wind farms. An instrumented quadcopter style sUAS was utilized for in-situ measurement of both temperature and relative humidity. The UAV flew a prescribed flight plan with the objective of collecting data in a stabilized hover at points both upstream and downstream of designated upstream wind turbines.

3.1.1 Wind Farm Setting

The wind farm in which most of the measurements were made consists of 44 General Electric (GE) 1.7 megawatt (MW) wind turbines. The GE 1.7 MW turbine is a three-blade, horizontal-axis wind turbine with active yaw control to keep the rotor continuously pointed into the wind [77]. The GE 1.7 MW turbine is designed with a 100 meter rotor diameter and hub heights of 80 and 96 meters. While both hub heights are represented within the wind farm, the 80 m hub height is more predominate and was utilized. To investigate the effect that a different hub height has on changes to near-surface relative humidity, limited measurements were also made within an adjacent wind farm. This wind farm was composed of 15 Gamesa G114 wind turbines. The G114 is a 2.0 MW, three-blade, horizontal-axis wind turbine with active yaw control. The turbine tower is 93 meters in height and is fitted with three blades that create a 114 meter rotor diameter [78]. Each wind farm is hosted in a largely agricultural setting with residential homes sparsely distributed throughout. Each turbine around which measurements were made was situated upstream of all other turbines during the time at which measurements were made. The general topography of the region, and specifically the zones in which measurements were taken, is flat, dry land with similar cultivar. During the course of the campaign, the ground adjacent to the GE 1.7 MW wind turbine was uniformly covered by soybeans approximately three inches in height; the G114 wind turbine was surrounded by sugar beets approximately two to three inches in height.

3.1.2 Synoptic and Local Meteorological Conditions

A dome of high pressure had dominated the region during the days leading up to the field campaign. As the campaign commenced, warm and moist air advected into the region on the backside of the departing high. This warm and moist airmass characterized the conditions for the duration of the campaign. As the area of high pressure moved further southeast, a low pressure system tracked north of the region. This brought about a modest increase in south and southwesterly winds during the middle portion of the measurement period. Concurrently, an associated weak cold front approached the region and stalled just north of the measurement zone. This brought about minor low-level instability before retreating as a warm front. The departure of this frontal boundary left warm air and light southerly flow for the remaining portion of the field campaign.

3.1.3 UAS Operations

All experimental measurements were made using an instrumented sUAS. In the absence of state and local legislation, the Federal Aviation Administration (FAA) singularly regulates UAS operations. The research nature of the operation classified it as a commercial operation. Consequently, requisite exemptions, authorization and registration was obtained from the FAA (Appendix A, B, C). Restrictions placed on this authorization curtailed flight greater than 400 feet above ground level (AGL). Consequently, turbines with an 80 meter hub height were intentionally sought out for the majority of the measurements in order for the UAS to sample the largest possible vertical swath of the downstream rotor swept area. GE 1.7 MW wind turbines with an 80 meter hub height have a top turbine tip height of 130 meters, or roughly 427 feet. This left only the top 27 feet of the vertical rotor swept area unavailable for investigation. The larger Gamesa G114 wind turbines have a top turbine tip height of 150 meters; thus, the top 30 meters of the rotor swept area was unsampled for these limited measurements.

Early in the planning phase of the field campaign, permission was secured from all landowners whose property lay underneath the flight path of the UAV or could be observed from the vantage point of the UAV. Prior to the commencement of flight activity, an initial site survey was undertaken to identify potential flight safety hazards. Following the identification of operational risks, a crew briefing took place to coordinate operations and mitigate risk. A ground perimeter was established under the area where take-off and recovery operations were planned in order to maintain positive control and keep nonparticipants safe. Notice to Airmen (NOTAM) were checked for the existence of any Temporary Flight Restrictions (TFRs).

All flight crew members possessed extensive training with respect to UAS operations, including certification from the Unmanned Safety Institute (USI) in UAS Safety, Vehicle Systems and Vehicle Operations.

3.1.4 System Description

A popular quadcopter, the DJI Inspire 1, was instrumented to make all experimental measurements. This platform was readily available off-the-shelf, lent itself well to the requisite instrumentation, offered ease of use, and the ability to hover in a stable manner. The instrumentation suite included a temperature and relative humidity measurement probe, along with an Arduino microcontroller, a GPS receiver, a SD card module, and a 9 VDC power source for data logging and supplying power to the sensor.

3.1.4.1 System Design

3.1.4.1.1 Instrumentation mount

For the purpose of making measurements, the DJI Inspire 1 had to be fitted with an instrumentation mount and sensors. The instrumentation mount, shown in Figure 3.1, was uniquely designed for the field campaign's specific purpose and sensor suite. Prior to fabrication, a series of test flights were undertaken to determine the height, above the UAV fuselage, at which both an onboard temperature and relative humidity sensor would not be influenced by the flow induced by the quadcopter's rotors. When the gear to which the motors and rotors are attached remained unretracted, the sensor values corresponded to that of adjacent ambient air when they were placed greater than four inches above the UAV fuselage. The sensor is vertically oriented with the bottom part of the sensor secured at this level, thus providing additional vertical separation. An analogous test was performed, with rotors turning, following mount fabrication with the aircraft in a representative final flight configuration. Each of these trials showed that the onboard instrumentation produced values equivalent to the ambient environment at the same altitude. The mount platform was specifically designed to host the temperature and relative humidity probe on the top shelf and the data logging components and power source on a lower shelf. The mount was designed to maintain the payload's mass over the vehicle's center of gravity. Consideration was also given to ensuring adequate airflow around the Arduino microcontroller and the sensor while maintaining a sufficient distance between them so as to not contaminate the sensors' reading. The mount was designed to attach to the vehicle at existing structural junctions and, once finalized, was 3-D printed out of a translucent thermoplastic. The instrumentation mount and UAV are shown in Figures 3.1 and 3.2 respectively.

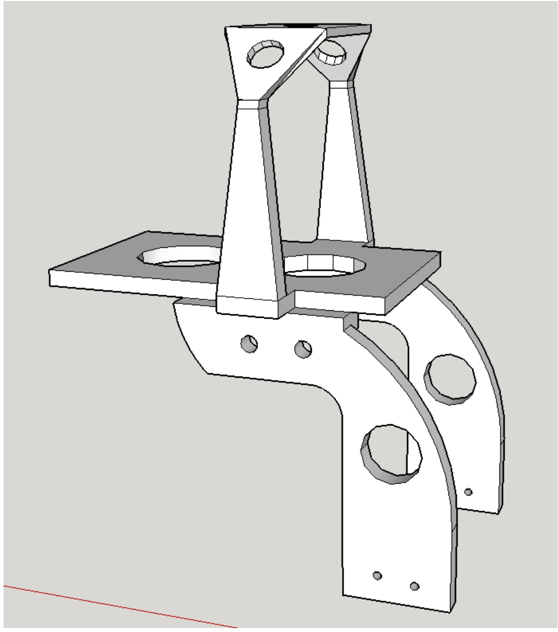

Figure 3.1 Instrumentation mount design.

Figure 3.2 Instrumentation mount attached to the UAV.

3.1.4.1.2 Sensors

Temperature and relative humidity measurements were obtained with a high accuracy meteorological probe containing a resistor temperature detector (RTD) and a capacitive humidity sensor respectively. The temperature and relative humidity sensor weighs 10 grams and is enclosed in a white polycarbonate housing with a 40 μm dust filter. An RTD measures temperature by correlating temperature to the temperature dependent resistance characteristics of a live metal conducting element. A platinum RTD is used for all temperature measurements. A capacitive humidity sensor consists of a hygroscopic dielectric material placed between a pair of electrodes. A polymer serves as the dielectric material in the chosen humidity sensor. As relative humidity changes, the amount of water molecules absorbed by the polymer changes the dielectric constant and thus the capacitance. Resistance and capacitance change in a near linear fashion with temperature and relative humidity respectively [79]. A capacitive sensor is a good choice for an unsterile environment or when condensation is possible but was specifically chosen for its strong performance with respect to accuracy, repeatability, stability and fast response.

The probe is factory calibrated and delivered with a factory calibration certificate. The sensors' uncertainty is based on a standard uncertainty multiplied by a coverage factor of $k = 2$, providing a level of confidence of approximately 95%. Temperature measurements enabled the calculation of a temperature lapse rate for the assessment of atmospheric stability. For the range of temperatures experienced during flight operations, temperature measurements have an uncertainty of ±0.1 K. Relative humidity measurements have a varying uncertainty that is a function of both temperature and humidity. For the range of conditions experienced during flight operations, uncertainty values varied from 0.39% - 0.5% RH.

The probe is factory calibrated with a supply voltage of 3.3 VDC and the aforementioned accuracy for the probe is only achieved when the probe is supplied by a voltage within the range of 3.3 - 5 VDC. To maintain this level of sensor performance, the voltage regulator on the Arduino microcontroller, used to process the sensor output, for data logging and to power the meteorological probe, was set-up to provide 3.3 VDC.

A sensor’s output does not reflect its input immediately. The time it takes for a sensor to approach its input is quantified by its response time. The humidity sensor has a longer response time than the temperature sensor, quoted by the manufacturer to be 15 seconds. A capacitive humidity sensor, such as the one used, generally has a much longer response time for decreasing humidity levels compared to environments where humidity increases. Thus, the response time is determined through consideration of this worst case, decreasing humidity level, scenario. Consequently, 16 second data records were taken, once a stabilized hover was realized, with only the last measurement utilized.

3.1.4.1.3 Data logging

An Arduino Uno Rev 3 microcontroller is utilized for onboard data logging. The Arduino microcontroller board is housed in a plastic protective case that also accommodates the 9 VDC power source and hosts a microSD card breakout board for data storage. On top of the plastic housing a 3DR uBlox GPS module is mounted to allow for time stamping of temperature and humidity data. Because the UAV carries its own data logger, along with the ability to time stamp the data, telemetry or remote collection schemes were unnecessary.

Interfacing the temperature and humidity sensor with the Arduino microcontroller required the use of a bulkhead adapter. This adapter, in conjunction with the manufacturer's wiring diagram, allowed for a proper hardware interface. Since less than 7 VDC may not provide the Arduino's 5 V pin with adequate voltage and greater than 12 VDC may result in the voltage regulator overheating, a 9 V battery is used to supply external power to the microcontroller. This concurrently allows the Arduino to supply 3.3 VDC to the sensor, ensuring the manufacturer's quoted accuracy. In turn, the meteorological probe provides a 0-1 V analog output. With a sensor operating range of -40 – 60 °C for temperature and 0-100% for humidity, a 0.6 V output was equated to 20 °C and 60% relative humidity. The Arduino processes data based on 5 V and 1024 bits of information. Consequently, this allows 1024 discrete analog levels to be detected. A data logging code was written and uploaded to the Arduino that converted the analog voltage to digital temperature and humidity values (the code is available in Appendix D).

The interfacing of a SD card and GPS module with the Arduino provided a way to capture and store data on board the aircraft. Using an existing Arduino SD card library, a SD card model was interfaced with the Arduino, thus allowing data to be written to and saved in a .csv file. The cycling of power creates a break in the log file that can be used to distinguish separate sorties. Interfacing a GPS module with the Arduino allowed for all data to be time stamped. The use of GPS time negated the need to initiate a system clock and provided an easy strategy for ground crew to note seminal events. In addition, besides time stamping data, the GPS receiver specifies, per the National Marine Electronics Association (NMEA) format, the following information:

- Latitude
- N/S hemisphere
- Longitude
- E/W hemisphere
- Fix quality
    - 0 = invalid
    - 1 = GPS fix
    - 2 = Digital GPS (DGPS) fix
- Number of satellites
- Horizontal dilution of precision (HDOP)
- Mean sea-level (MSL) altitude in meters
- Height above the WGS84 datum in meters
- Time since last DGPS update
- DGPS reference station ID

- Checksum

From the NMEA sentence, time, latitude, longitude, hemisphere, fix quality, along with MSL and WGS84 altitudes were extracted and written. This allows another way, principally through a latitude and longitudinal coordinate, to associate the data during post-processing.

3.1.4.2 System Validation

Prior to the field campaign, the UAV was flight tested, per the requirement of the Section 333 exemption, and the UAS operationally checked. The fully instrumented UAV underwent increasingly sophisticated maneuvering, commencing from a simple hover and proceeding to maneuvers that reflect those anticipated during execution of the flight plan. This was accomplished in a slow, progressive manner to ensure that the vehicle retained its stability. Once confidence was gained in the platform, the data acquisition system was operationally checked during flight. The fully configured platform is shown in Figure 3.3.

Figure 3.3 Fully instrumented UAV in flight configuration.

3.1.5 Flight Plan

Constrained by the FAA's altitude restriction and with the motivation to sample as much of the downstream rotor swept area as possible, wind turbines with an 80 meter hub height were intentionally sought out for the majority of testing. With the objective of calculating differences in upstream and downstream relative humidity, an easily accessible area with uniform topography and surface moisture characteristics, along with the absence of other natural or man-made flow disturbances at the ground, was identified. Due to the concurrent ability to easily access a 93 meter hub height turbine within close proximity, limited measurements were also taken around this taller turbine. Due to the higher top tip height, and the FAA regulations in place at the time of the field campaign, a smaller percentage of the rotor-swept area of the 93 meter hub height wind turbine was sampled. Schematics of the foundational profiles flown around the wind turbines are shown in Figures 3.4 and 3.5 with measurement points represented by white dots.

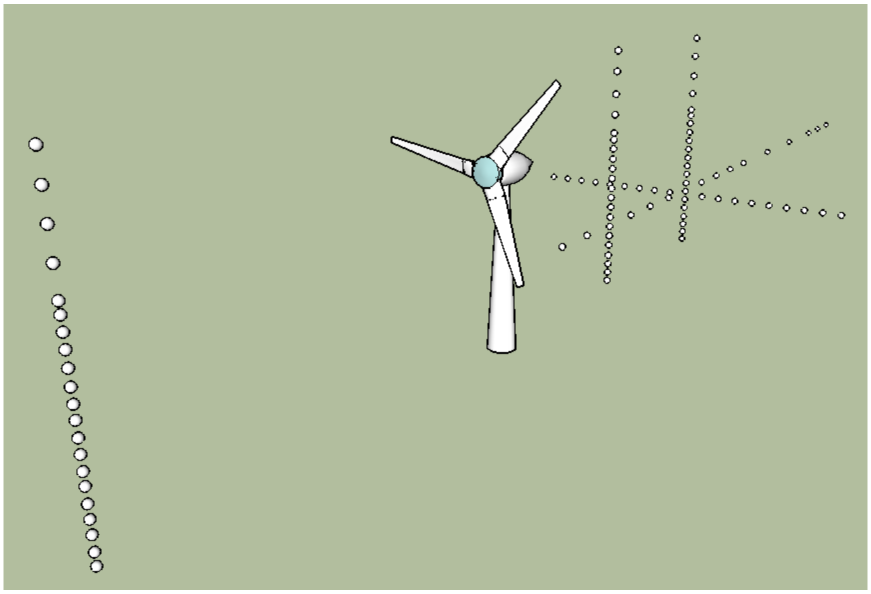

Figure 3.4 Front-angled view showing basic flight profiles, and measurement points, flown around wind turbines.

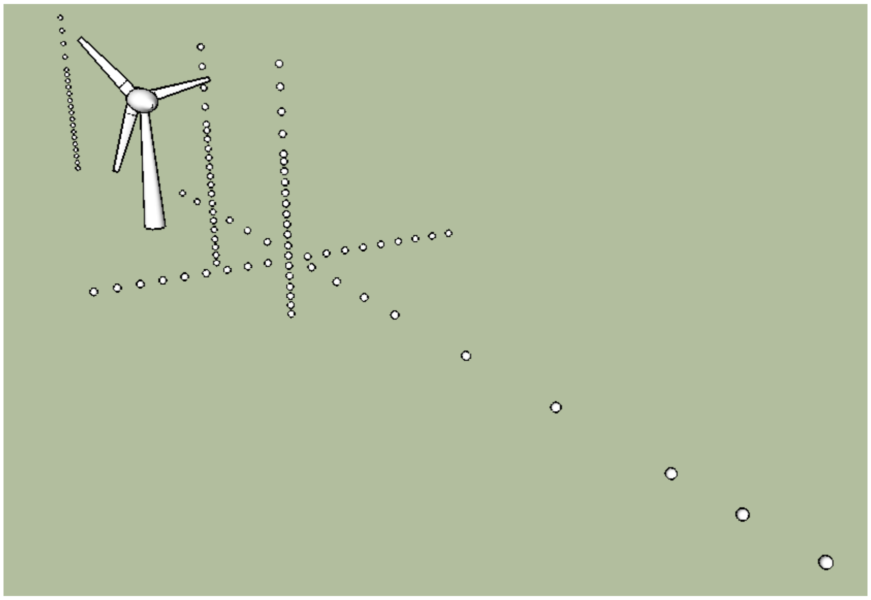

Figure 3.5 Rear-angled view showing basic flight profiles, and measurement points, flown around wind turbines.

Basic flight profiles consist of sweeps made in the vertical, downstream and spanwise directions. Vertical measurements, spanning from 2 to 120m in altitude, are made at 2 rotor diameters up and downstream of the turbine. Measurement points are spaced 5m apart up to the lower rotor hub height of 80m and then spaced at 10m intervals up to 120m. Downstream points, beginning 50m aft of the rotor plane, are made at an altitude equal to the bottom turbine tip height. Measurements are made every 25m downstream through 300m. Beyond 300m, measurements are made every 50m through 500m. This distance still ensures that visual line of sight (VLOS) is maintained with the UAV. Lateral measurements are also made at the bottom turbine tip height, at a downstream position of 2 rotor diameters, and are spaced 10m apart out to 90m on either side of the turbine hub. This brings lateral measurements out 40m on either side of the rotor shadow.

A launch and recovery zone was established per the best practice recommendations of the Unmanned Safety Institute (USI), a professional training organization for UAS operators [80]. The launch and recovery zones were composed of two distinct areas, referred to as Zones A and B. Zone A is an area for crewmembers to remain clear of when the system is on the ground with rotors turning. The perimeter put forth for this area is 10 times the UAV diameter. Only crewmembers associated with the starting and launching of the system are allowed inside this area. Zone B consists of a larger outer perimeter that is clear of both spectators and hazardous terrain. The dimension put forth for Zone B is the greater of 150 feet on the upwind side of the launch and recovery point or 100 times the UAV diameter. For this purpose, the greatest dimension of the Inspire UAV was taken to be 3 feet. Therefore, Zone A was established with a 30 foot radius and Zone B with a 300 foot radius.

3.2 Simulation and Modeling

In the absence of an analytical theory, numerical simulation can be used to provide qualitative and quantitative insights into complex unsteady flows, including turbulent flows through wind farms. Numerical simulation of turbulent flows, such as the flow within a WTABL, sets out to solve the time dependent Navier-Stokes equations using one of three computational strategies. At the top level, direct numerical simulation (DNS) involves no approximation or averaging, and is aimed at predicting all turbulent length and time scales in the flow through high-order spatial and temporal discretization schemes. While DNS produces one manifestation of the turbulent flow accurately, the very high computational expense makes it presently impractical for realistic applications, such as the WTABL, because the number of grid points scales with Reynolds number to the power of 9/4 [81]. At the lower level, the Reynolds-averaged Navier Stokes (RANS) strategy models the flow by decomposing the dependent variables into mean and fluctuating parts [81]. The mean portion of the flow is predicted by solving the time-averaged Navier-Stokes equations while the contribution of the fluctuating, or unsteady, part to the flow is introduced through turbulence modeling. RANS solvers are very efficient in terms of the required computational resources, but turbulence models introduce a high level of approximation. Finally, the third strategy, large-eddy simulation (LES) provides an intermediate level of approximation of the turbulent flow. The numerical experiments conducted for this work are accomplished using LES.

3.2.1 Large Eddy Simulation

LES resolves the large turbulent eddies under the assumption that the large scales are dependent on the aggregate flow and models the smaller scales of motion based on

Kolmogorov’s assumption that they are isotropic and more common in their character [82]. These tenets are the result of a unidirectional energy cascade that transports turbulent energy from the largest, anisotropic, energy containing eddies to smaller, isotropic eddies affected by viscosity. LES partitions the resolved and residual velocity and scalar fields, such as temperature and humidity, by filtering. The filtered turbulent flow field consists of a wide range of turbulent scales greater than a scale found within the inertial subrange, where energy travels from larger to smaller eddies. The scales lost by the filtering process are statistically invariant, with a few exceptions (such as the flow in the vicinity of a solid boundary), and consequently lend themselves more readily to modeling [25]. Hence, LES simulates large eddies and their interaction with the parameterized smaller scale eddies.

3.2.1.1 Governing Equations

LES produces time dependent, three-dimensional solutions to the filtered Navier-Stokes equations representing the transport of mass, momentum, and energy. The filtered LES version of the Navier-Stokes equations for incompressible, high Reynolds number (Re) ABL flow in this investigation are:

$$\frac{\partial \tilde{u}_i}{\partial x_i} = 0 \tag{3.1}$$

$$\frac{\partial \tilde{u}_i}{\partial t} + \tilde{u}_j \frac{\partial \tilde{u}_i}{\partial x_j} = -\frac{1}{\rho}\frac{\partial \tilde{p}}{\partial x_i} - \frac{\partial \tilde{\tau}_{ij}}{\partial x_j} + \delta_{i3} g \frac{\tilde{\theta} - \langle \theta \rangle}{\theta_0} + f_c \varepsilon_{ij3}\left(\tilde{u}_j - u_{gj}\right) + f_T \delta_{i1} \tag{3.2}$$

$$\frac{\partial \tilde{\phi}}{\partial t} + \tilde{u}_j \frac{\partial \tilde{\phi}}{\partial x_j} = -\frac{\partial \pi_j}{\partial x_i} \tag{3.3}$$

where the coordinate system is defined as $x_i(i = 1,2,3) = (x, y, z)$ with *x* and *y* representing horizontal coordinates (*x* being oriented in the streamwise direction) and *z* denoting the vertical coordinate, and the tilde and the angle brackets represent spatial filtering and horizontal averaging, respectively, $\tilde{u}_i (i = 1,2,3)$ is the velocity vector field with components in the streamwise, lateral, and vertical direction, $\tilde{\theta}$ and θ_0 are the resolved potential temperature and the reference temperature, respectively, f_c is the Coriolis parameter, g is the gravitational acceleration, δ_{ij} is the Kronecker delta, ε_{ijk} is the alternating unit tensor, and f_T is a forcing term modeling the effect of the wind turbines. In this study, the assignment of $z = 0$ is associated with the ground surface. Equation 3.1 is the filtered conservation of mass equation, Equation 3.2 is the filtered momentum equation, with the Boussinesq approximation and Coriolis terms included, and Equation 3.3 is the transport equation for a scalar, ϕ, which in this study can represent either potential temperature, θ, or specific humidity, q. In the aforementioned equations, $\tau_{ij} = \widetilde{u_i u_j} - \tilde{u}_i \tilde{u}_j$ is the SGS Reynolds stress resulting from the filtering of the nonlinear terms in the original Navier-Stokes equations, and $\pi = \widetilde{u_j \theta} - \tilde{u}_j \tilde{\theta}$ is the SGS flux of heat or humidity resulting from the filtering of the convection terms in the scalar transport equation (both SGS quantities need to be modeled to close the set of equations).

3.2.1.2 Subgrid-scale Modeling

Unresolved scales are more isotropic in nature, and are, therefore, more amenable to parameterization. Smagorinsky's eddy viscosity model [81] is one of the most popular models, based on the assumption of the instantaneous and complete dissipation of all energy that cascades downward from the larger to the smaller scales until it reaches the viscous dissipation scale. The SGS Reynolds stress, τ_{ij}, representing the residual stress left over following filtering of the momentum equations, is parameterized in order to bring about closure of the governing equations. Within the Smagorinsky eddy viscosity model, the SGS Reynolds stress, τ_{ij}, is expressed as:

$$\tau_{ij} = -2\nu_T \bar{S}_{ij} \tag{3.4}$$

while the SGS flux of heat or humidity is represented via the SGS eddy-diffusivity model as

$$\pi_j = -\frac{\nu_T}{Pr_T}\frac{\partial \tilde{\theta}}{\partial x_j} \tag{3.5}$$

where $\bar{S}_{ij}$ is the mean strain-rate tensor, Pr_T is the SGS Prandtl number, and the eddy, or turbulent, dissipative viscosity, ν_T, is represented by:

$$\nu_T = (C_s \mathrm{l})^2 \sqrt{2\bar{S}_{ij}\bar{S}_{ij}} \tag{3.6}$$

In Equation 3.6, C_s is the Smagorinsky coefficient, and l is a length scale at which energy is passed from the resolved to the subgrid field (hence making it a function of the filter width, Δ) [83]. The specification of the Smagorinsky coefficient is one of the main challenges of the models that use the eddy-viscosity/diffusivity hypothesis, only having a well-defined value for isotropic turbulence [84]. In this study, the magnitude of the Smagorinsky coefficient is determined dynamically using a Lagrangian scale-dependent model as developed by Porte-Agel et al. [85] and extended to scalar transport equations by Bou-Zeid et al. [86].

3.2.1.3 Boundary Conditions

The system of equations of motion and scalar transport require both boundary and initial conditions. Output from a concurrent precursor simulation with periodic boundary conditions in both horizontal directions is used to provide realistic inflow conditions to the main simulation that include wind turbines [87]. Velocity and scalar fields from the end of the precursor simulation's turbulent ABL domain, absent of wind turbines, are written to the end of the main domain, containing wind turbines, and are blended with the WTABL flow. This subsequently creates a turbulent inflow, through a periodic boundary condition, for the first row of wind turbines. LES results utilizing this precursor strategy have been shown to be in good agreement with field data [87].

Due to the Coriolis effect, the direction of the wind changes with height in the ABL, subscribing to an Ekman spiral. This presents a challenge in trying to align the geostrophic velocity components to achieve the desired flow direction at hub height. For the simulations, an adjustment to the geostrophic wind direction is accomplished through manipulation of a Coriolis force source term in the momentum equations in order to achieve the desired hub height flow direction [88]. Once the simulation reaches a fully-developed state, this term is deactivated in order to avoid unrealistic dynamics.

In addition to the stream-wise periodicity previously described, a periodic boundary condition also wraps the domain boundary from one lateral boundary to the other. A top boundary is established well above the top of the simulated ABL, with the condition that no flow passes through the boundary and that all vertical gradients vanish. An effective top of the ABL, isolating it from the top boundary of the domain, is specified via a capping inversion created by a temperature gradient. A source or sink of heat is introduced above the top of the ABL within the precursor simulation to enable the desired atmospheric stability [88]. The lower boundary condition is defined by the standard logarithmic Monin-Obukhov similarity theory [89], [90], [91], [92], [93] (see equations 3.7-3.9). A constant potential temperature and specific humidity flux are assigned to the surface. Figure 3.6 illustrates the boundary conditions associated with the precursor and main simulation.

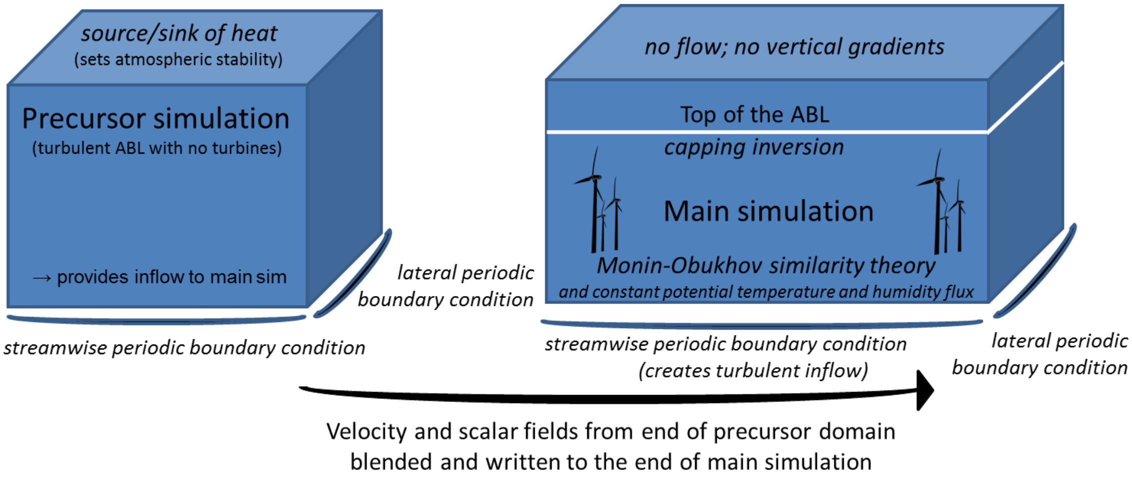

Figure 3.6 Boundary conditions for the precursor and main simulation.

3.2.1.4 Numerical Method

The LES code used in this research features a Fourier-based pseudo-spectral method in the horizontal directions, where operations are exchanged, based on ease, between physical and spectral spaces [94]. A second-order accurate, centered difference scheme is used in the vertical direction. This centered difference scheme requires the use of a staggered grid in the vertical direction. Here, the vertical component of velocity is located on a cell face with all other variables located at cell centers, with the exception of the surface values of temperature and moisture that are referenced to the physical surface at z=0.

With the high Reynolds number flow associated with the ABL, flow within close proximity to the ground cannot be resolved. Assuming a homogeneous surface and using a uniform vertical grid, wall modeling from Monin-Obukhov similarity theory [89], [90], [91], [92], [93] is used. Monin-Obukhov similarity theory relates the instantaneous surface stresses, $\tau_{13}|_{z=0}, \tau_{23}|_{z=0}$, to the instantaneous velocity components, u_i, at the first vertical grid point by:

$$\tau_{i3}|_{z=0} = -u_*^2 \frac{\widetilde{u_i}}{V_f} = -\left[\frac{\kappa V_f}{ln\left(\frac{z}{z_0}\right)-\Psi_M}\right]^2 \frac{\widetilde{u_i}}{V_f} \tag{3.7}$$

where u_* is the friction velocity, κ is the von Karman constant, taken to be 0.4, Ψ_M is the momentum stability correction function, z_0 is the effective roughness length, and V_f is the locally filtered horizontal velocity at the first vertical grid point defined as:

$$V_f = \left[\tilde{u}_1 \left(\frac{\Delta z}{2}\right)^2 + \tilde{u}_2 \left(\frac{\Delta z}{2}\right)^2\right]^{\frac{1}{2}} \tag{3.8}$$

Differences in the properties of the underlying surface and overlying atmosphere determine the direction and magnitude of surface fluxes. The LES code sets up a constant flux layer using Monin-Obukhov similarity theory where the surface heat flux is computed as:

$$\langle w'\theta' \rangle_{z=0} = \frac{u_* \kappa(\theta_s - \tilde{\theta})}{ln\left(\frac{z}{z_{0s}}\right)-\Psi_H} \tag{3.9}$$

Here, θ_s is the imposed surface potential temperature, $\tilde{\theta}$ represents the resolved potential temperature at the first vertical grid point, z_{0s} is the scalar roughness length equal to $0.1 z_0$, and Ψ_H is heat flux stability correction function [17], [13]. A similar approach is applied to the specific humidity at the surface.

Velocity and scalar fields are integrated in time using a second-order accurate Adams–Bashforth scheme. The second-order Adams method approximates the integrand with a first-order polynomial, or linear interpolant. The Adams-Bashforth method is fully explicit [95].

To more efficiently handle the large number of grid points, and associated calculations, the LES code has been parallelized to take advantage of the power of parallel computing. The domain is decomposed by taking a specified number of two-dimensional horizontal slices through the entire domain. Distributed machines are linked by the message-passing interface (MPI) standard. The LES code is based on a previous algorithm that was also utilized by Calaf et al. [11], [17], with various augmentations implemented in the code to facilitate its use on more complex applications.

3.2.1.5 Wind Turbine Parameterization

The accuracy of LES of a WTABL depends on both the modeling of the SGS and wind turbine induced forces. A wind turbine extracts kinetic energy from the wind and converts it into mechanical energy. The LES code parameterizes this energy extraction process in the absence of turbine design specifics and models the wind turbines by the Actuator (drag) Disc Method (ADM). The ADM is a common, straightforward and proven approach in numerical modeling [96], [97].

An ADM with rotation (ADM-R) similar to that found in [96], [98], [99] is implemented in these numerical studies. According to this parameterization, the rotor disk is divided into a number of annulus segments, of spanwise length $\mathrm{D}r$, within which lift and drag forces are individually evaluated. The resultant lift and drag forces per rotor annulus segment of spanwise length $\mathrm{D}r$ can be determined from

$$F_L = \frac{1}{2}\rho_0 V_{rel}^2 c_L \frac{Bc}{2\pi r} \tag{3.10}$$

and

$$F_D = \frac{1}{2}\rho_0 V_{rel}^2 c_D \frac{Bc}{2\pi r} \tag{3.11}$$

respectively, where ρ_0 is the density of the air, V_{rel} the relative velocity of the blade segment, c_L and c_D are the lift and drag coefficients, respectively, of the blade element, B specifies the number of blades, c represents the chord length, and r is the radial coordinates with respect to the location of the blade element. These forces are projected onto the axial and tangential directions in order to represent the effect on the flow,

$$F_A = F_L \cos(\phi) + F_D \sin(\phi) \tag{3.12}$$

$$F_T = F_L \sin(\phi) - F_D \cos(\phi) \tag{3.13}$$

where $\emptyset$ is the angle between the rotor plane and the flow velocity relative to the rotor blade, estimated as

$$\phi = \tan^{-1}\left(\frac{V_N}{\Omega r - V_t}\right) \tag{3.14}$$

with V_t being the tangential component of the induced velocity. In Meyers and Meneveau, 2010, 2013 [98], [99] the axial (or thrust) and tangential forces were expressed as

$$F_A = \frac{1}{2}\rho_0 C'_T \langle \bar{u} \rangle_d^2 A_{rotor} \tag{3.15}$$

$$F_T = \frac{1}{2}\rho_0 C'_P \langle \bar{u} \rangle_d^2 \frac{\langle \bar{u} \rangle_d}{\Omega r} A_{rotor} \tag{3.16}$$

where averaging both in time (represented by bar) and over the disk area (angle brackets and subscript ‘d’) are applied to the velocity normal to the rotor disk. C'_T and C'_P are modified thrust and power coefficients (linked to the lift and drag coefficients and the geometry of the blade), respectively. Each of these are evaluated based on the velocity at the disk, as opposed to using the undisturbed upstream velocity at the hub height, which is associated with the usual thrust and power coefficients C_T and C_P. The relationship between the two sets of thrust and power coefficients is given as

$$C_T = (1-a)^2 C_T' \tag{3.17}$$

$$C_P = (1-a)^3 C_P' \tag{3.18}$$

Given C_T, C_P and a from experimental measurements, the thrust and power coefficients C_T' and C_P' can be determined, and the forces acting on the flow can be updated. To avoid Gibbs oscillations on the LES grid, the forces are filtered via a Gaussian convolution filter [100].

3.2.1.6 Simulation Cases

Simulations are performed for both a single wind turbine and a wind turbine array in stable, unstable and neutrally stable atmospheric regimes. An unstable simulation was created with a negative temperature lapse rate of 2 °C in the first 300 m. This temperature gradient is representative of the various stable lapse rates observed during the field campaign. Presuming that the greatest effect on relative humidity will be observed during stable atmospheric conditions, due to stratified nature of the ABL, LES of the turbine array was executed with a negative lapse rate of both 1 and 2 °C in the first 300 m. Unstable and neutral ABL scenarios were created with a positive temperature lapse rate of 1.13 °C in the first 100 m and equal to the dry adiabatic lapse rate (DALR) respectively.

Replicating the turbine around which most measurements were made, all simulations were implemented with 80 m hub height, 100 m rotor diameter wind turbines having a thrust coefficient of 0.81. A positive lapse rate of .5 g/kg in the first 400 m was instituted for specific humidity. A logarithmic inflow wind profile was imposed that resulted in a 6 m/s wind speed at hub height. A constant potential temperature of 300 K and a constant specific humidity flux of 0.01 g/kg•m/s were imposed at the ground level. The thrust coefficient was obtained from GE as a function of hub height wind speed. With a logarithmic inflow profile for wind that results in a 6 m/s hub height value, a thrust coefficient of 0.81 was used.

Simulations for a single wind turbine were executed within a domain having downstream, lateral and vertical dimensions of 1500 m x 400 m x 400 m respectively. Single wind turbine simulations were constructed on a grid of 128 x 64 x 96 equally spaced points. As a result, the grid structure on which all single wind turbine simulations were executed had a resolution of 11.7 m x 6.3 m x 4.2 m. The domain size for the simulation of WTABLs depended on the type of thermal stratification, with an increased vertical dimension used for neutral and unstable stratifications allowing for the increased depth of the ABL to be adequately captured. 7 x 4 wind turbine arrays in a stably stratified environment were constructed within a domain of 3600 m x 1600 m x 400 m and built on a grid consisting of 192 x 128 x 96 points. This provided a resolution of 18.8 m x 12.5 m x 4.2 m. Neutral and unstable WTABLs were built within a domain of 3600 m x 1600 m x 1200 m. Therefore, 6 x 4 wind turbine arrays in a neutral or unstable ABL, had a resolution of 18.8 m x 12.5 m x 12.5 m. For all thermal stratifications and array configurations, wind turbines were spaced 650 m apart in the downstream, and 400 m in the lateral, direction.

CHAPTER IV

RESULTS AND DISCUSSION

4.1 Experimental Measurement

During the time period of May 24 – 27, 2016, between morning and evening civil twilight, multiple flights were carried out around wind turbines at two different wind farms. Concurrent temperature measurements that were taken during each flight were used to characterize the atmosphere's static stability. All points flown within a paired upstream and downstream profile were flown within a 10 – 15 minute timeframe. Select data points, that were captured early-on in each flight, were re-flown at the conclusion of the flight to ensure a quasi-static atmosphere during any given flight. Over the course of a given flight, freestream atmospheric conditions showed very little variation.

4.1.1 Test for Statistical Significance

Statistical significance quantifies how likely a result is not associated with random chance. Conversely, the p-value represents the probability that random chance explains the result. A paired t-test was used to test for the statistical significance of the change in observed upstream and downstream relative humidity values. In general, a paired t-test is used to compare the means of two related data sets composed of the same number of points and organized in pairs [101]. Generally, the two sets of data are separated by time and are created before and after an 'event'. A statistical analysis of all experimental measurements was conducted by pairing corresponding points on either side of the wind turbine. The statistical significance of the change brought about by the presence of the wind turbine is expressed by a p-value and accompanying level of confidence.

An example calculation of the p-value for a suite of upstream and downstream vertical profiles is shown below. The dependent variable is the measured relative humidity.

Table 4.1 Upstream and downstream vertical profiles of relative humidity.

Height [m]	Upstream Relative Humidity [%]	Downstream Relative Humidity [%]
2	79.18	78.65
7	78.69	77.1
12	77.22	74.78
17	74.78	71.85
22	71.85	69.4
27	70.37	67.47

Table 4.1 (Continued)

32	67.93	65.03
37	65.48	63.41
42	64.5	63.11
47	63.53	62.63
52	62.05	61.16
57	61.95	60.18
62	60.56	58.72
67	60.05	58.73
72	58.77	58.27
77	58.26	57.8
80	56.82	57.82

Table 4.1 (Continued)

90	55.98	56.84
100	54.63	55.38
110	52.94	54.39
120	52.7	53.91

Upstream and downstream measurements observed at the same height are paired. For the vertical profiles above, this provides 21 matched observation pairs. To test the null hypothesis that the mean difference is zero, the following steps are executed:

1) The difference between each pair of observations is calculated.
2) The mean difference, $\bar{d}$, representing the average change between upstream and downstream relative humidity, is calculated. For this suite of profiles, the mean difference is 1.02905.
3) The standard deviation, s_d, of the differences is calculated. For this suite of profiles, the standard deviation of the differences is 1.42026.
4) The standard error of the mean difference is calculated according to,

$$SE(\bar{d}) = \frac{s_d}{\sqrt{n}} \tag{4.1}$$

where n represents the number of paired observations. For these paired observations, the standard error of the mean difference is 0.30993.

5) The t-statistic, for use in subsequent testing of the null hypothesis, is calculated according to,

$$T = \frac{\bar{d}}{SE(\bar{d})} \tag{4.2}$$

For these observed vertical flight profiles, the t-statistic is 3.32027.

6) Under the null hypothesis, this statistic follows a t-distribution with n-1, or 20, degrees of freedom.

7) Using a standard t-distribution table, and considering 20 degrees of freedom and T equal to 3.32027, yields a p-value of 0.003.

Hence, since 0.003 is less than 0.05, it is concluded that the average change in relative humidity of 1.02905% is not due to random chance but can be attributed to the presence of the wind turbine.

Confidence level ranges from 0 – 100% and is calculated according to,

$$100 \bullet (1 - \text{p-value}) \tag{4.3}$$

Table 4.2 provides selected confidence levels and the associated p-value. Per convention, characterization of a statistically significant change is reserved for confidence levels greater than 90%.

Table 4.2 Confidence levels and associated p-values.

Confidence Level	p-value
99%	0.01
95%	0.05
90%	0.1
80%	0.2
50%	0.5

4.1.2 Experimental Measurements around a Single Wind Turbine

4.1.2.1 Stable Atmospheric Boundary Layer

During the overnight hours, the ground cools as it emits more radiation than it absorbs. Consequently, the air immediately overlying the ground cools by conduction as heat energy is transferred downward toward the ground. In the absence of winds, which mix the air, or clouds, which reradiate previously absorbed infrared radiation, the cooling of air not adjacent to the ground is slower. These dynamics create a nocturnal inversion where environmental temperature increases with height.

Measurements of temperature and relative humidity during stable atmospheric conditions were accomplished just after morning civil twilight, in keeping with the restrictions levied by the FAA, and before the morning inversion was broken by convection. A positive lapse rate for relative humidity existed during each of these flights as surface moisture evaporated into the bottom of the air column and air temperature increased with height.

Measurements of upstream and downstream relative humidity within vertical profiles, observed during stable atmospheric conditions, are shown in Figures 4.1 – 4.4. Figures 4.1 – 4.3 provide measurements taken around the GE 1.7 MW wind turbine and Figure 4.4 gives measurements around the Gamesa G114 turbine. All measurements were captured during temperature inversions characterized by a negative lapse rate in the first 100 m ranging from a modest 0.5 °C to a robust 4 °C. Hub height wind speeds ranged from 4 – 7 m/s.

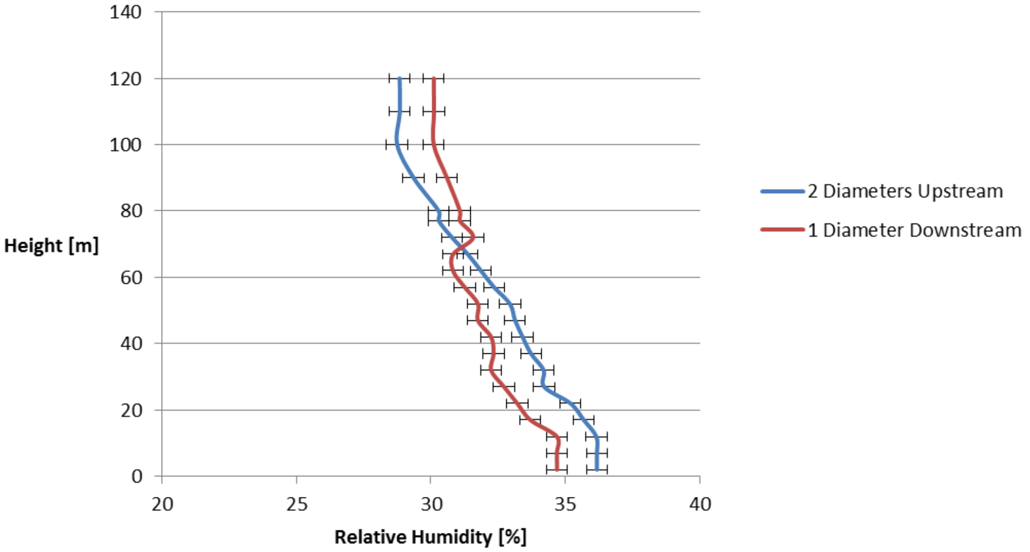

Figure 4.1 Measured upstream and downstream vertical relative humidity profiles around a GE 1.7 MW wind turbine with an 80 m hub height and 100 m rotor diameter.

Observed 0.5 °C/100 m temperature lapse rate with an upstream hub height wind speed of 7 m/s.

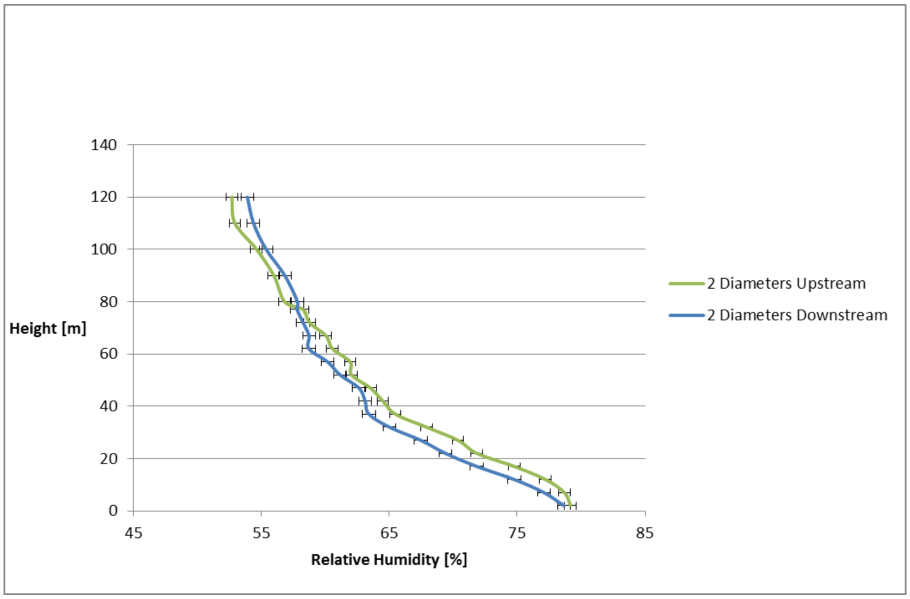

Figure 4.2 Measured upstream and downstream vertical relative humidity profiles around a GE 1.7 MW wind turbine with an 80 m hub height and 100 m rotor diameter.

Observed 4.4 °C/100 m temperature lapse rate with an upstream hub height wind speed of 4 m/s.

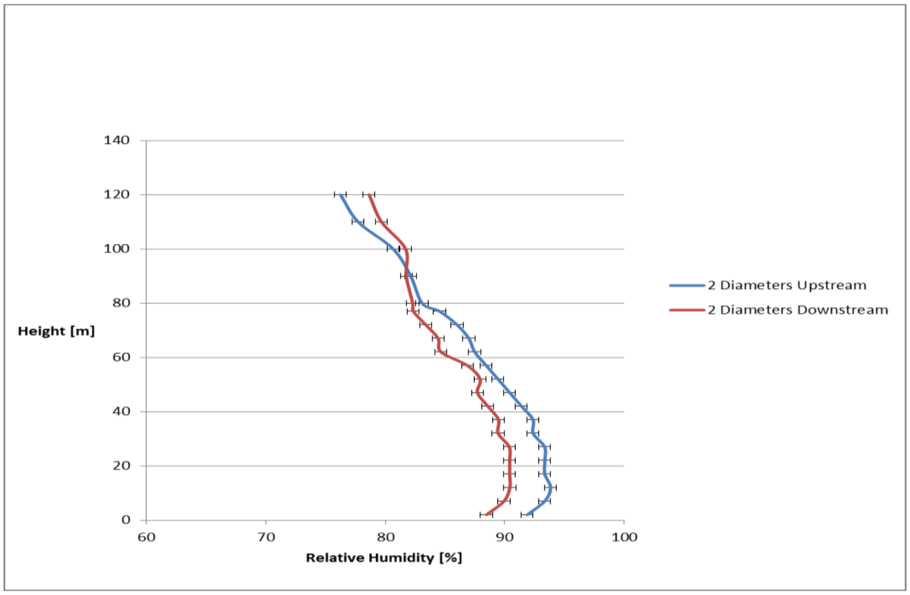

Figure 4.3 Measured upstream and downstream vertical relative humidity profiles around a GE 1.7 MW wind turbine with an 80 m hub height and 100 m rotor diameter.

Observed 4 °C/100 m temperature lapse rate with an upstream hub height wind speed of 5 m/s.

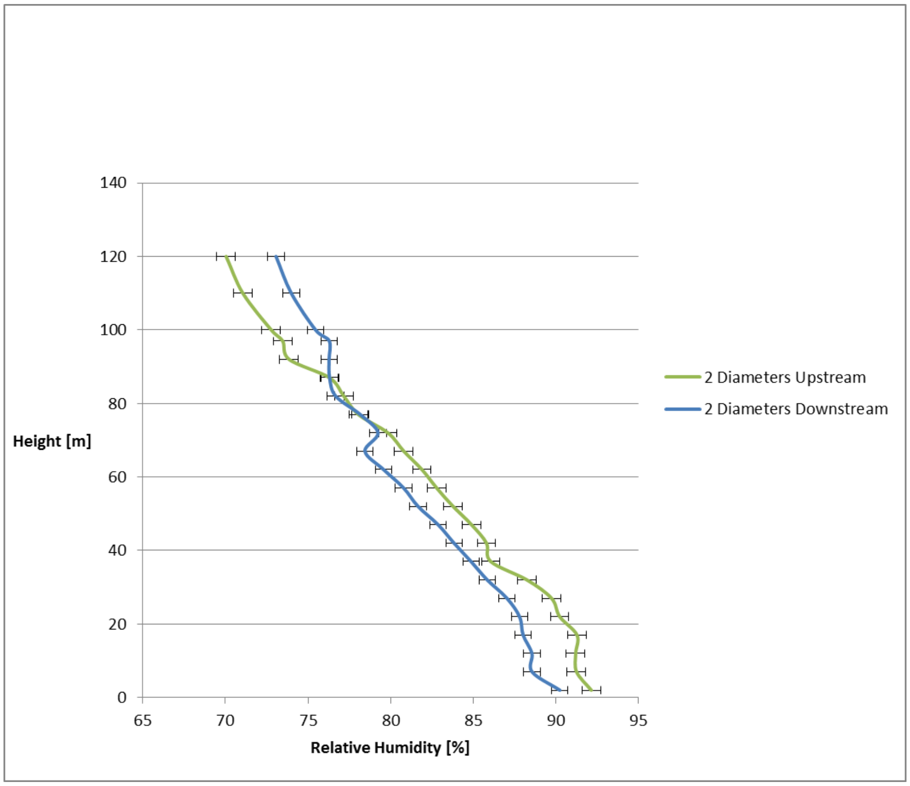

Figure 4.4 Measured upstream and downstream vertical relative humidity profiles around a Gamesa G114 wind turbine with a 93 m hub height and 114 m rotor diameter.

Observed 1.8 °C/100 m temperature lapse rate with an upstream hub height wind speed of 6 m/s.

Each of the observed scenarios displays a general decrease in humidity closer to the ground and an increase aloft. The inflection point for these regions of change generally occurs slightly below the turbine hub height, with the exception of the final vertical profile flown around the GE 1.7 MW turbine. This general trend of the inflection point located slightly below the turbine hub height is presumably the result of a sinking wake and the exception is attributed to the irregular nature of the turbulent wake structure. The indistinct nature of this inflection is also captured in the downstream profile around the Gamesa G114 turbine as the two profiles cross over each other several times. In each scenario, the demarcation between the region of relative humidity change is brought about by a change in the general slope of the downstream profile, opposed to an observed change in the general trend of the upstream profile. This suggests that the change in relative humidity is indeed the result of the presence of the wind turbine. The maximum decrease in relative humidity is consistently observed slightly below the lower turbine tip height. Figures 4.5 – 4.8 show the difference between upstream and downstream measurements of relative humidity for the four aforementioned stable scenarios. The previous observations regarding the location of the inflection point and the region of maximum reduction are easily seen in these figures. The decrease below the hub is not necessarily constant in the vertical direction. Due to the short time-span over which each measurement was made over, absent of any sort of time-averaging, some fluctuations in the vertical direction can be observed in these profiles. Further, the magnitude of change between the area of maximum humidity decrease just below the lower turbine tip height and the decrease in proximity to the ground can be markedly greater. However, as the descending blades of the turbine deliver drier air aloft to the lower turbine tip height, this region of decreased relative humidity might move downward with downstream distance.

Figures 4.5 – 4.8 show that the region of increase in relative humidity just above the hub is also significant. As previously noted, FAA restrictions in place at the time of the investigation thwarted measurements above 400 feet AGL. However, it is noted that the magnitude of change of the upper-most observation is on par with the magnitude of change at the corresponding distance below the turbine hub height. Collectively, these observations suggest that the descending blades are delivering drier air downward while the ascending blades are displacing moister air upward.

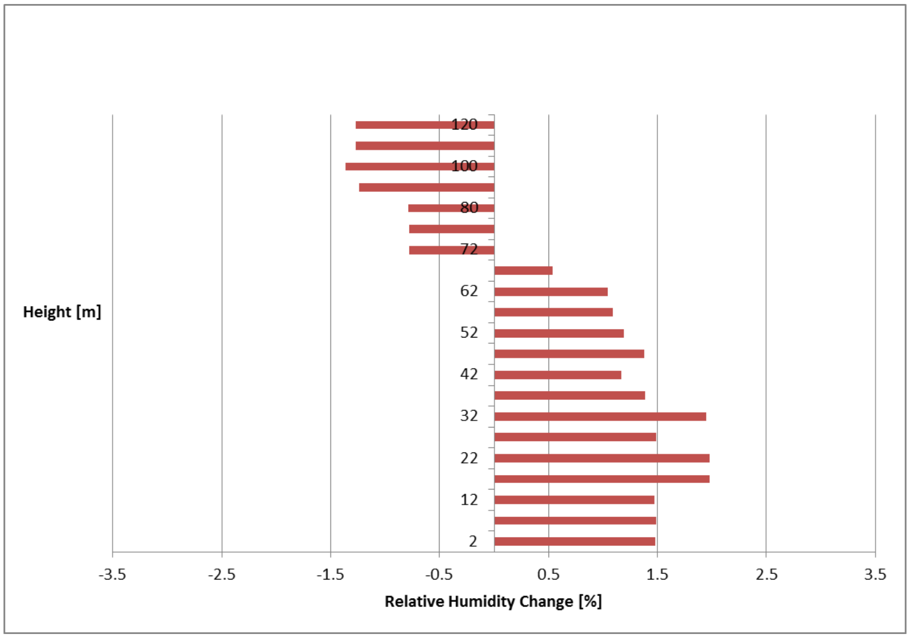

Figure 4.5 Change in measured relative humidity (upstream minus downstream) as a function of height around a GE 1.7 MW wind turbine with an 80 m hub height and 100 m rotor diameter.

Observed 0.5 °C/100 m temperature lapse rate with an upstream hub height wind speed of 7 m/s.

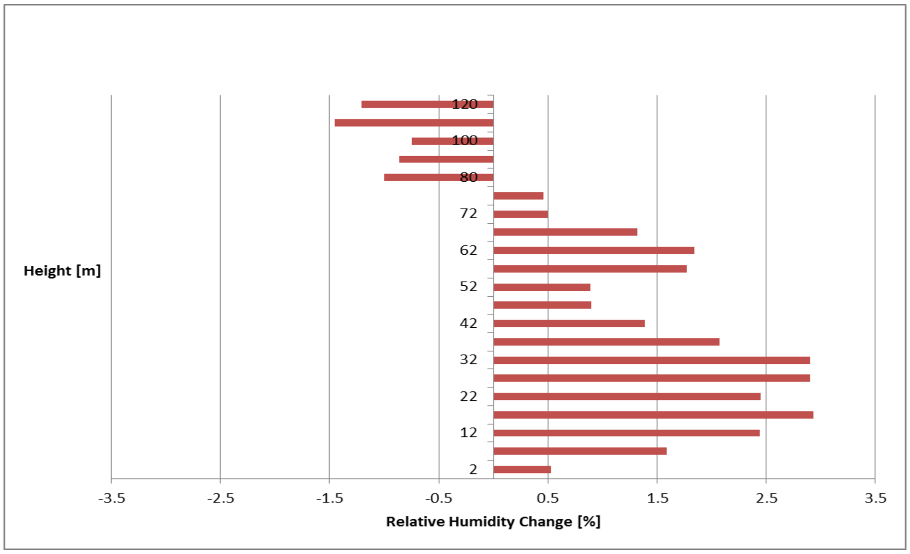

Figure 4.6 Change in measured relative humidity (upstream minus downstream) as a function of height around a GE 1.7 MW wind turbine with an 80 m hub height and 100 m rotor diameter.

Observed 4.4 °C/100 m temperature lapse rate with an upstream hub height wind speed of 4 m/s.

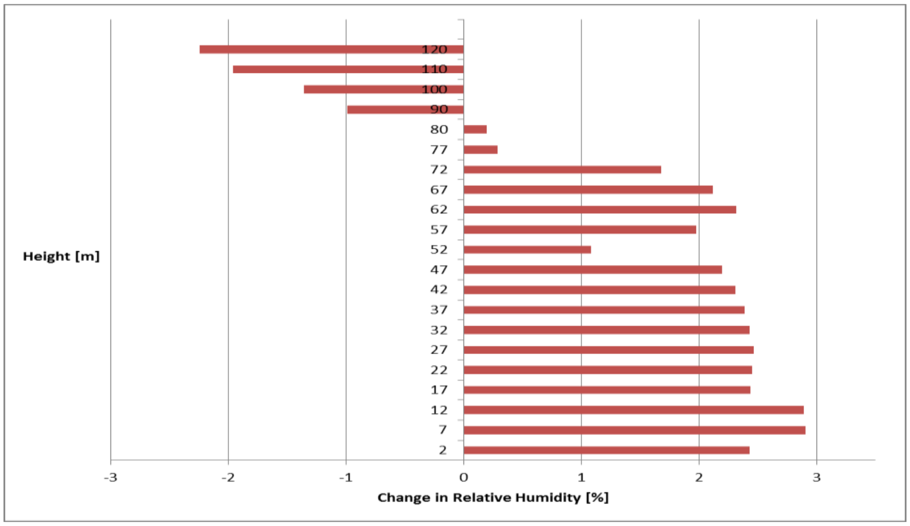

Figure 4.7 Change in measured relative humidity (upstream minus downstream) as a function of height around a GE 1.7 MW wind turbine with an 80 m hub height and 100 m rotor diameter.

Observed 4 °C/100 m temperature lapse rate with an upstream hub height wind speed of 5 m/s.

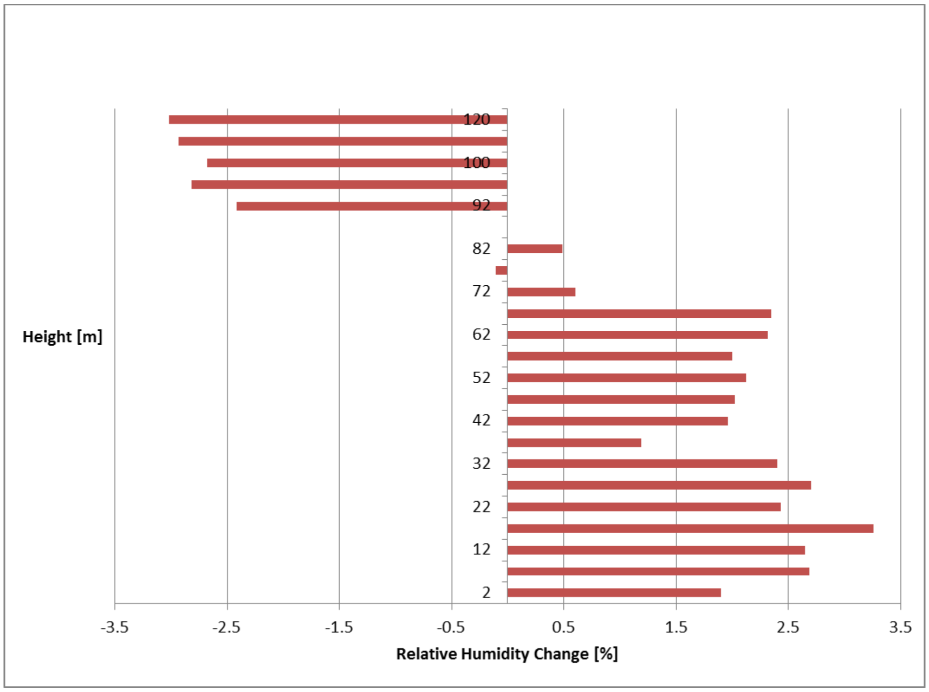

Figure 4.8 Change in measured relative humidity (upstream minus downstream) as a function of height around a Gamesa G114 wind turbine with a 93 m hub height and 114 m rotor diameter.

Observed 1.8 °C/100 m temperature lapse rate with an upstream hub height wind speed of 6 m/s.

As detailed in Table 4.3, all measured changes in relative humidity around the GE 1.7 MW turbine, captured during stable regimes, are found to be statistically significant at the 95% level (threshold p-value of 0.05) or higher with p-values ranging from < .001 to .044. The single profile flown around the Gamesa G114 is found to be statistically significant at the 90% level (threshold p-value of 0.1) with a p-value of .075.

Table 4.3 Statistical significance, from paired samples t-test, of relative humidity change between measured upstream and downstream vertical profiles in a stably stratified condition.

Lapse Rate in first 100m	Measurement location	Wind Turbine	Hub height wind speed	Maximum RH change below turbine tip height	Statistical Significance [%]	p-value
4°/100 m	2Ø upstream 2Ø downstream	GE 1.7 MW	5 m/s	-2.9%	99%	<.001
4.4°/100 m	2Ø upstream 2Ø downstream	GE 1.7 MW	4 m/s	-2.9%	99%	.003
0.5°/100 m	2Ø upstream 1Ø downstream	GE 1.7 MW	7 m/s	-2%	95%	.044
1.8°/100 m	2Ø upstream 2Ø downstream	Gamesa G114	6 m/s	-3.3%	90%	.075

Lateral measurements around each turbine type are shown in Figures 4.9 and 4.10. Measurements are made at 2 rotor diameters downstream and at the lower turbine tip height. Similar trends are observed for both of the flights accomplished. At two diameters downstream, due to the clockwise rotation of the rotor blades, an asymmetry in the lateral change to relative humidity exists between the right and left side of the wake.

Both profiles show the greatest decrease in relative humidity to be offset slightly to the right of the centerline with generally lower values, and less of a recovery, found all along the right-hand side of the wake. For a clockwise rotating turbine, the right-hand side of the turbine disk is associated with descending blades and the transport of less humid air aloft downward. Observed decreases in relative humidity along the centerline of the lateral profile are similar in magnitude to those observed during the vertical profile flown during the same timeframe. Pairing upstream and downstream observations and using a paired t-test for statistical analysis, all changes to lateral relative humidity were found to be statistically significant at the 99% level (using a threshold p-value of .01) with p-values < .001. Figures 4.11 and 4.12 display the difference between upstream and downstream measurements of relative humidity corresponding to the lateral profiles of Figures 4.9 and 4.10.

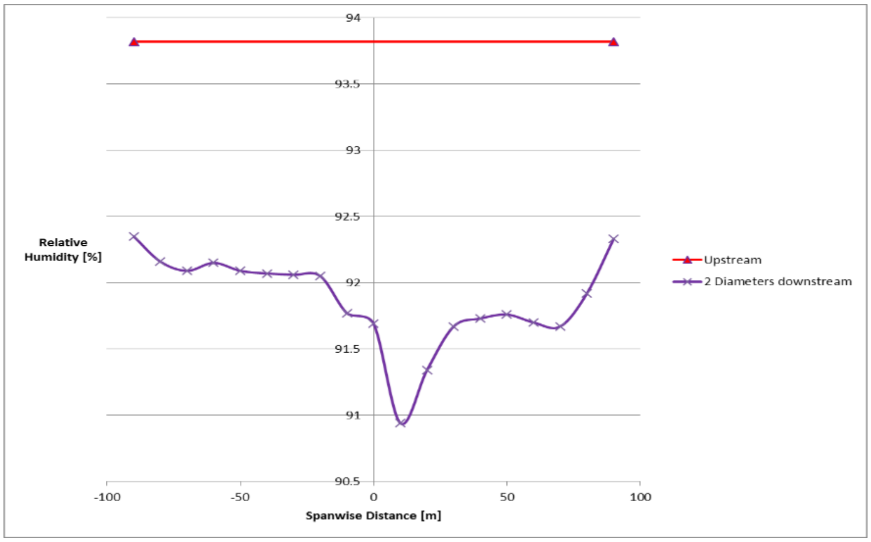

Figure 4.9 Upstream and downstream lateral relative humidity measurements, at the lower turbine tip height, around a GE 1.7 MW wind turbine with an 80 m hub height and 100 m rotor diameter.

Observed 4 °C/100 m temperature lapse rate with an upstream hub height wind speed of 5 m/s.

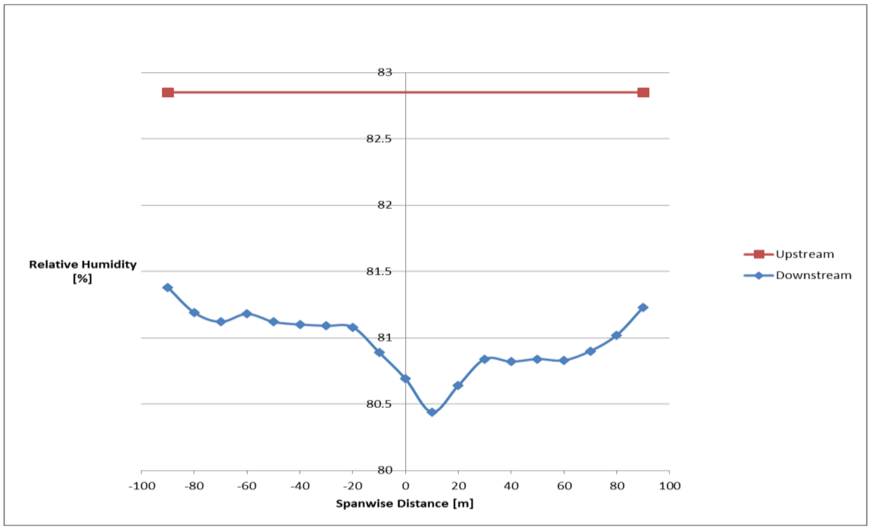

Figure 4.10 Upstream and downstream lateral relative humidity measurements, at the lower turbine tip height, around a Gamesa G114 wind turbine with a 93 m hub height and 114 m rotor diameter.

Observed 1.8 °C/100 m temperature lapse rate with an upstream hub height wind speed of 6 m/s.

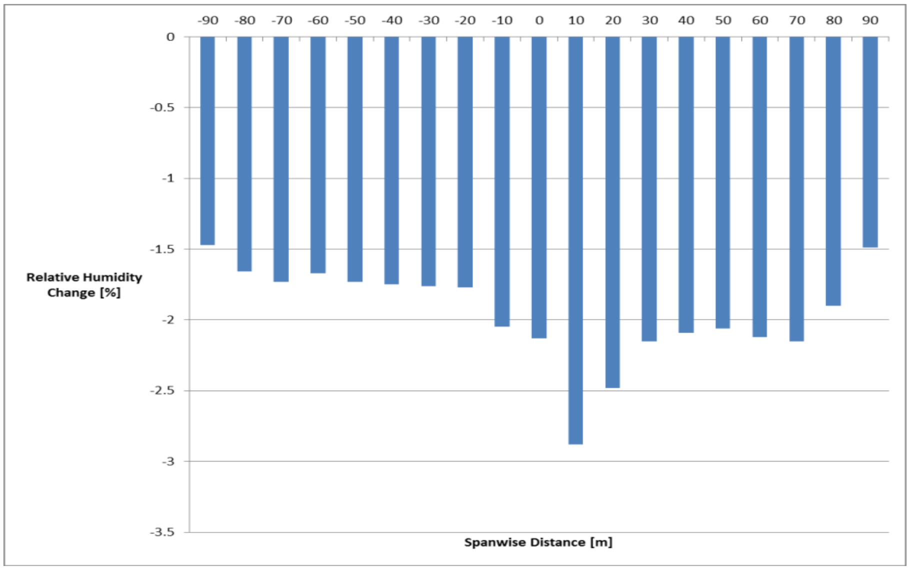

Figure 4.11 Change in measured relative humidity (upstream minus downstream), at the lower turbine tip height, as a function of lateral position around a GE 1.7 MW wind turbine with an 80 m hub height and 100 m rotor diameter.

Observed 4 °C/100 m temperature lapse rate with an upstream hub height wind speed of 5 m/s.

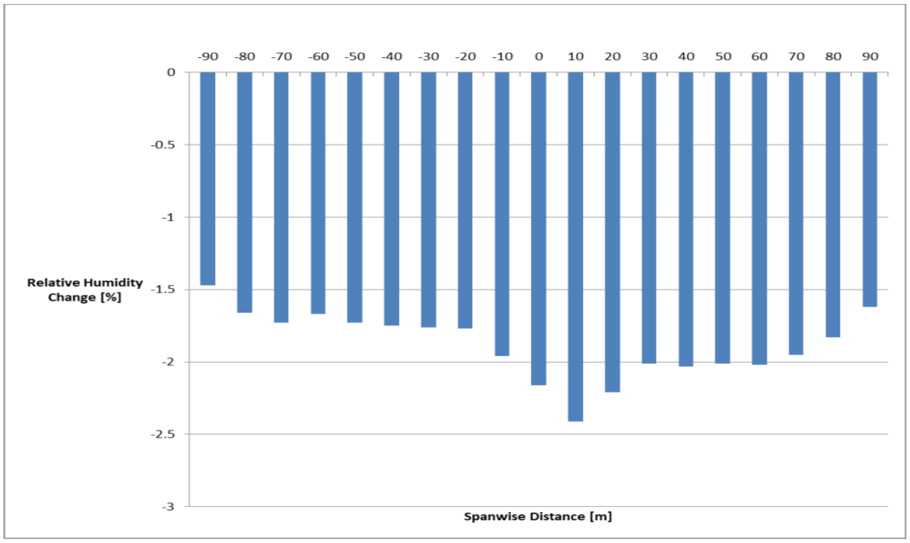

Figure 4.12 Change in measured relative humidity (upstream minus downstream), at the lower turbine tip height, as a function of lateral position around a Gamesa G114 wind turbine with a 93 m hub height and 114 m rotor diameter.

Observed 1.8 °C/100 m temperature lapse rate with an upstream hub height wind speed of 6 m/s.

In order to analyze the changes to, and recovery of, relative humidity as a function of downstream distance, flight profiles were flown downstream of the turbine tower at the lower turbine tip height. Flights were constrained to 500 m downstream in order to maintain VLOS with the UAV. Figures 4.13 – 4.14 give the measured relative humidity values around each turbine model while Figures 4.15 – 4.16 provide the difference between measured upstream and downstream values. Pairing upstream and downstream observations and using a paired t-test for statistical analysis, all changes to downstream relative humidity were found to be statistically significant at the 99% level (using a threshold p-value of .01) with p-values < .001.

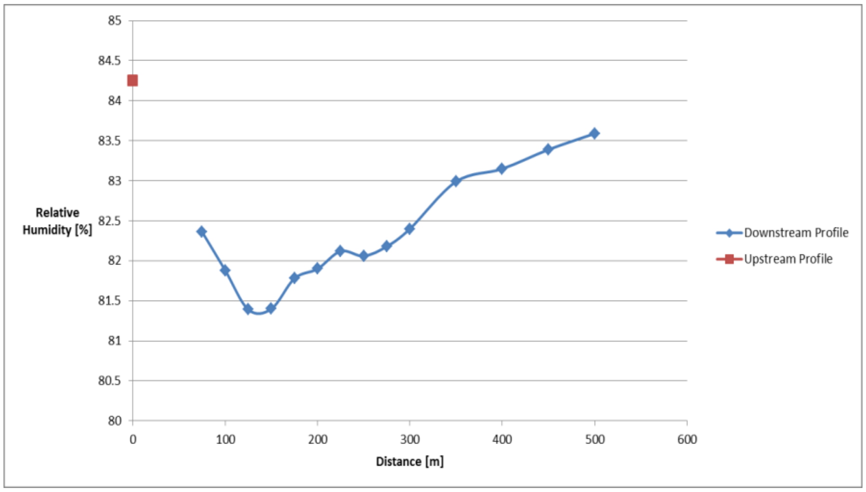

Figure 4.13 Downstream relative humidity measurements, at the lower turbine tip height, around a GE 1.7 MW wind turbine with an 80 m hub height and 100 m rotor diameter.

Observed 4 °C/100 m temperature lapse rate with an upstream hub height wind speed of 5 m/s.

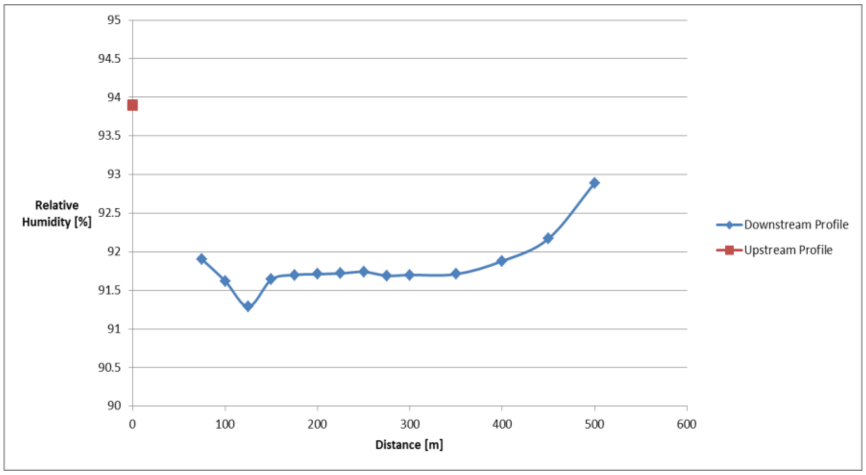

Figure 4.14 Downstream relative humidity measurements, at the lower turbine tip height, around a Gamesa G114 wind turbine with a 93 m hub height and 114 m rotor diameter.

Observed 1.8 °C/100 m temperature lapse rate with an upstream hub height wind speed of 6 m/s.

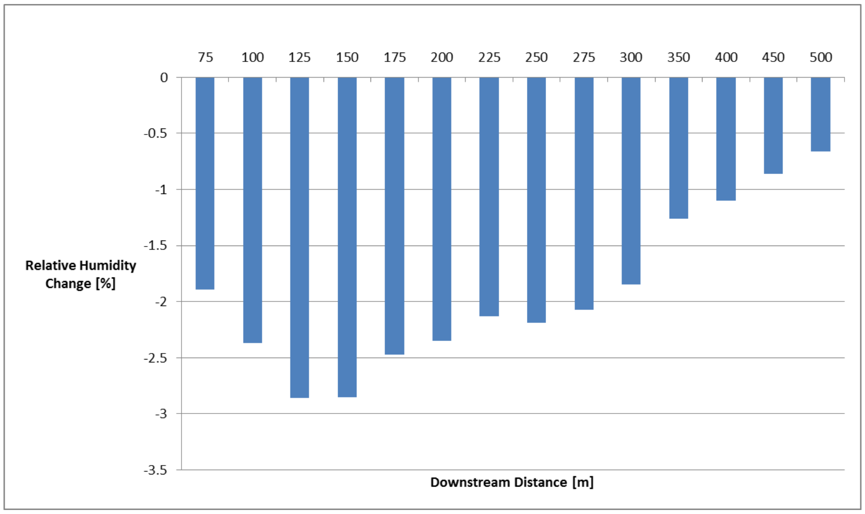

Figure 4.15 Change in measured relative humidity (upstream minus downstream), at the lower turbine tip height, as a function of downstream position around a GE 1.7 MW wind turbine with an 80 m hub height and 100 m rotor diameter.

Observed 4 °C/100 m temperature lapse rate with an upstream hub height wind speed of 5 m/s.

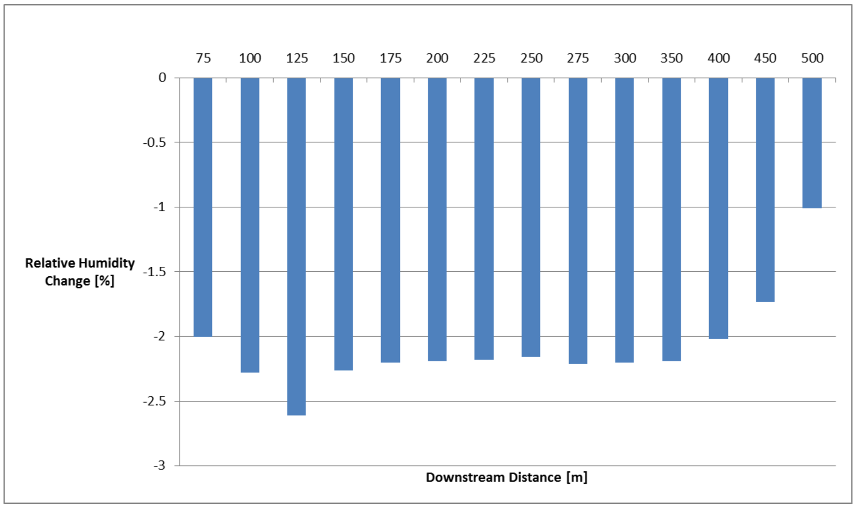

Figure 4.16 Change in measured relative humidity (upstream minus downstream), at the lower turbine tip height, as a function of downstream position around a Gamesa G114 wind turbine with a 93 m hub height and 114 m rotor diameter.

Observed 1.8 °C/100 m temperature lapse rate with an upstream hub height wind speed of 6 m/s.

Both flights around each turbine model indicate a steep gradient in relative humidity immediately aft of the wind turbine disk, show the greatest reduction in relative humidity to occur at approximately 1.25 rotor diameters, and reveal a shallower recovery. The relatively larger Gamesa G114 turbine suggests a recovery displaced further downstream. However, each turbine's wake has recovered nearly 60-80% of the maximum relative humidity deficit by 500 meters downstream.

4.1.2.2 Unstable and Neutral Boundary Layer

An unstable, or convective, boundary layer occurs whenever the underlying surface is warmer than the overlying air. A cloud-free day with light winds, the occurrence of a warmer body of water beneath cooler air, or the advection of cold air aloft, are each possible circumstances that create this dynamic. Turbulence in this unstable boundary layer is more vigorous, especially turbulent energy in the vertical direction, and consequently mixes the atmosphere well.

Flight times during the heat of the day, on a cloud free afternoon, were selected in order to capture unstable scenarios. During this time, the sun is intensely heating the ground, and in turn the adjacent air, at a rate greater than turbulent eddies can transport this air upward. Hence, temperatures markedly decreased with height, especially in the lowest 100m.

A neutral atmosphere is often found during the transition between an unstable and stable environment. Therefore, evening flights were planned that would allow for all data to be gathered just prior to evening civil twilight, in order to comply with FAA regulations. When the intense heating of adjacent air by the ground has subsided but air parcels are still well mixed, a temperature lapse rate near that of the dry adiabatic lapse rate (DALR) can manifest and yield a neutrally stable scenario. This occurs as cooler parcels aloft are mixed down by turbulent eddies and warm at the DALR, and warmer parcels are mixed similarly upward while cooling adiabatically at the DALR.

The aforementioned stable and neutral stability characterizations of the atmosphere assess only the static stability of the atmosphere. Static stability only takes into account buoyancy forces, ignoring shear associated with the mean flow [102]. Hence, the enhanced vertical mixing brought about by the wind turbine does not change the character of the downstream flow in unstable and neutral atmospheric regimes as significantly as in a stably stratified environment.

The vertical profile shown in Figure 4.17 is representative of the profiles measured in unstable and neutral atmospheric regimes where the measured upstream and downstream values of relative humidity are found to be only slightly discrepant. The change in relative humidity, shown in Figure 4.18, continues to be indicative of the mixing of drier air downward and moister air upward in the presence of a positive relative humidity lapse rate. However, error bars associated with sensor uncertainty are observed to overlap. Therefore, while the upstream and downstream profiles are slightly discrepant, the presence of overlapping error bars result in the profiles to be taken as equivalent.

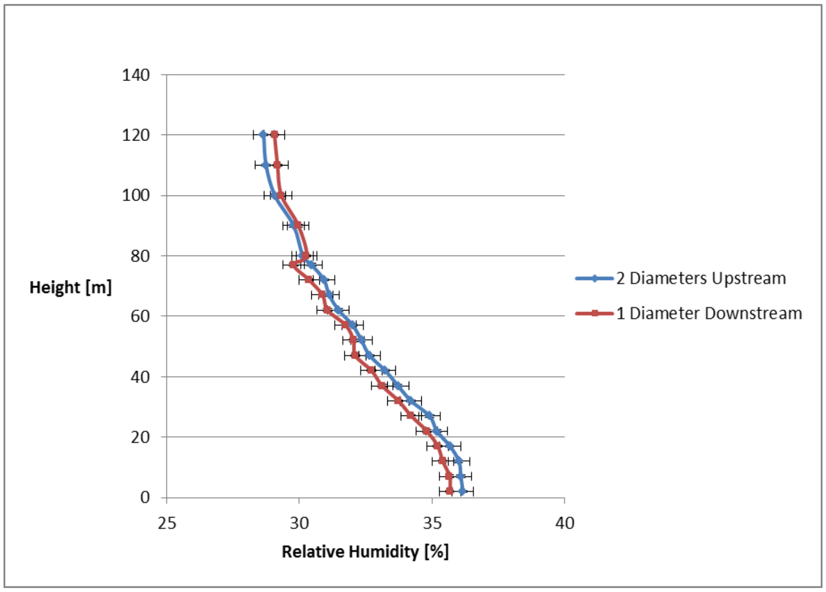

Figure 4.17 Measured upstream and downstream vertical relative humidity profiles around a GE 1.7 MW wind turbine with an 80 m hub height and 100 m rotor diameter.

Observed 0.97 °C/100 m temperature lapse rate with an upstream hub height wind speed of 7 m/s.

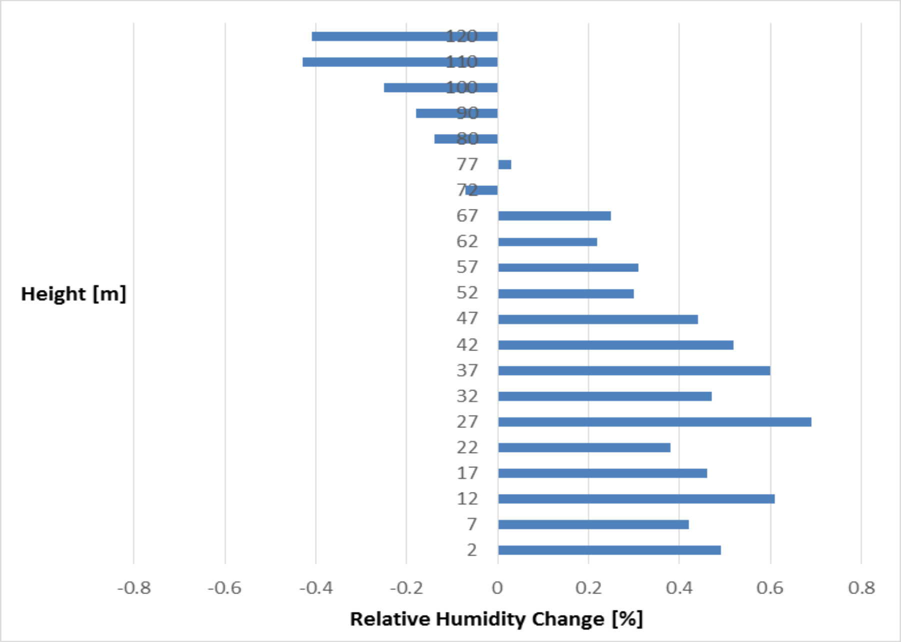

Figure 4.18 Change in measured relative humidity (upstream minus downstream) as a function of height around a GE 1.7 MW wind turbine with an 80 m hub height and 100 m rotor diameter.

Observed 0.97 °C/100 m temperature lapse rate with an upstream hub height wind speed of 7 m/s.

4.2 Comparison between Numerical and Experimental Results around a Single Wind Turbine

With the largest changes to relative humidity observed in the relatively unmixed atmosphere characterized by stable stratification, and upstream and downstream profiles measured in unstable and neutrally stable regimes taken to be consistent, LES is contrasted with experimental measurements obtained over multiple flights in stable atmospheric conditions. The previously described LES configuration is executed for a single wind turbine for qualitative comparison since surface fluxes were not measured during the field campaign and the turbine power coefficient was unavailable from the manufacturer. Contour plots of instantaneous streamwise velocity in Figure 4.19 highlight flow features downstream of the turbine. These plots are taken on a horizontal plane at hub height elevation, along with two vertical planes at the boundaries of the domain. The effect of the turbine's clockwise rotation is noticeable in the skewness of the wake, characterized by the upwelling of low momentum from below the rotor on the left side and the downwelling of high momentum from above the rotor on the right side.

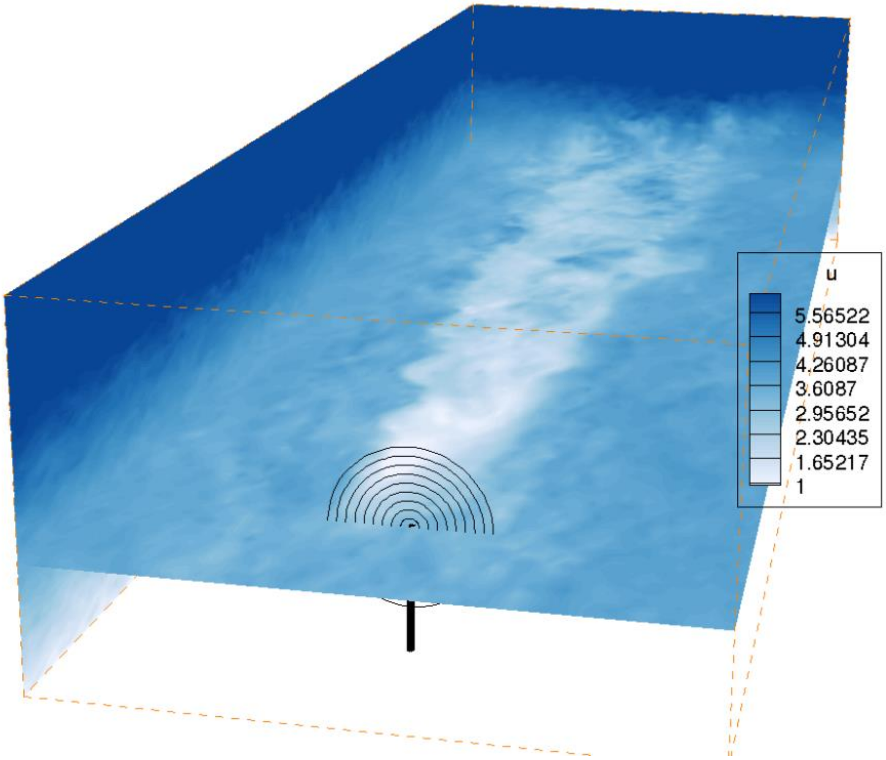

Figure 4.19 Contour plots of the instantaneous velocity magnitude in a horizontal plane section passing through the hub (two other vertical plane sections at the lateral boundaries are also shown).

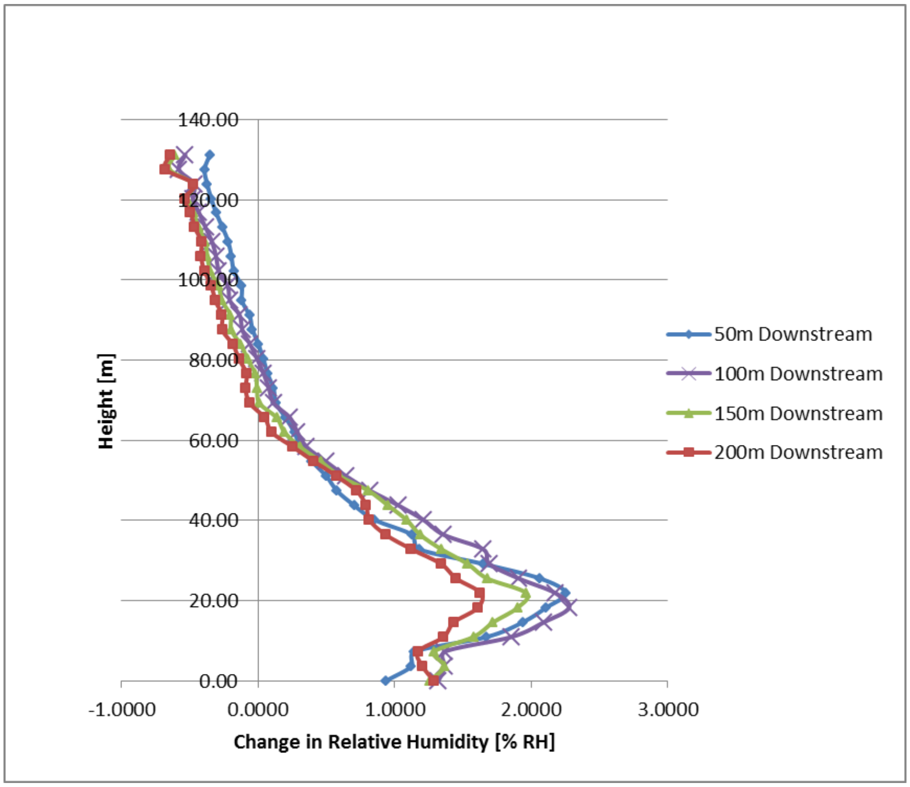

Figure 4.20 Change in LES time-averaged relative humidity (upstream minus downstream) as a function of height. Simulation output shows a general decrease in relative humidity below the turbine hub height and a maximum decrease just below the lower turbine tip height.

Figure 4.20 shows the difference between upstream and downstream values of time-averaged relative humidity at 50 m increments from 50 m to 200 m downstream. With the imposition of a positive humidity lapse rate, LES output shows a general decrease in relative humidity below the turbine hub height and an increase above it as the rotor mixes moist air upward and delivers drier air downward. The inflection point between these two regions occurs at the turbine hub height at 50 m downstream. As surmised from the field observations, the height of the inflection point decreases with downstream distance as the wake sinks. At all downstream distances, the maximum decrease in relative humidity occurs in the form of a ‘nose’ just below the lower turbine tip height with a maximum decrease of 2.3% relative humidity occurring at 1 rotor diameter downstream. The magnitude of humidity change decreases with downstream distance from this point. Interestingly, the height of the 'nose' does not decrease with downstream distance. This behavior, in contrast to the height of the inflection point, along with the sharper gradient present below the turbine hub height is attributed to the presence of the underlying surface. This lower boundary provides a constraint that supports the build-up of air with decreased humidity. The magnitude of change (increase) at the upper tip height is more modest and is less than, or equal to, one-half of the magnitude of the change (decrease) at the lower tip height. This dichotomy is most likely associated with the absence of a constraining physical boundary.

Figure 4.21 provides a contour plot showing the averaged relative humidity change in a vertical plane passing through the turbine's hub and parallel to the streamwise direction. Readily evident is the area of maximum decrease in relative humidity at, and slightly below, the lower turbine tip height. An increase in relative humidity is observed at the level of the upper turbine tip height. Well away from the surface, the more vertically diffuse nature of this region is apparent. Figure 4.22 shows a continuous horizontal slice through the lower turbine tip height. A split in the humidity deficit is observed to originate approximately 1 rotor diameter downstream. This split in the humidity 'wake' is responsible for the perceived shorter streamwise humidity deficit along the centerline seen in Figure 4.21. Figure 4.22 shows how the region of humidity decrease actually extends much farther downstream. While a very sharp gradient borders the region of maximum deficit in the lateral direction, the presence of an expanding wake is apparent as the broader deficit in humidity extends laterally well beyond the shadow of the rotor swept area.

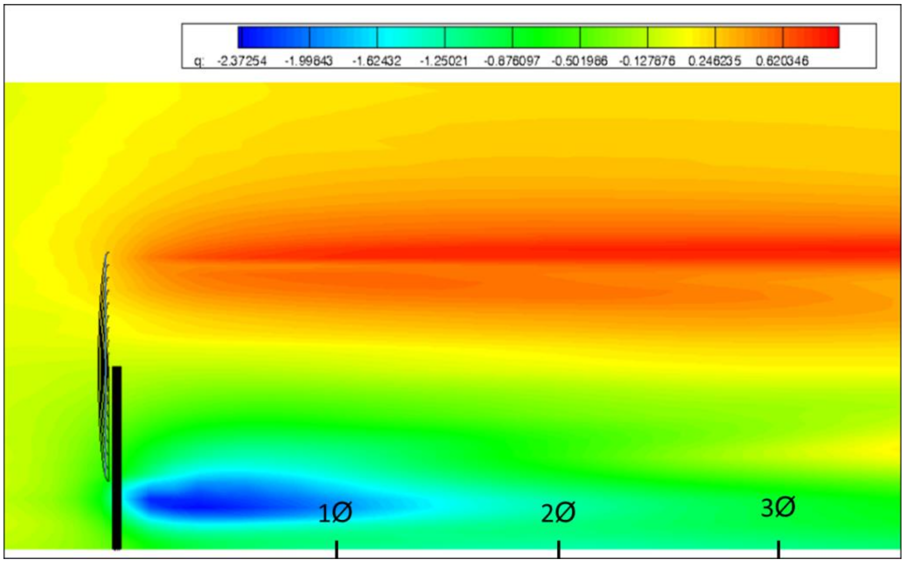

Figure 4.21 Contour plots of time-averaged relative humidity change in a vertical plane section passing through the hub and parallel to the streamwise direction (the legend shows changes in relative humidity compared to the upstream level).

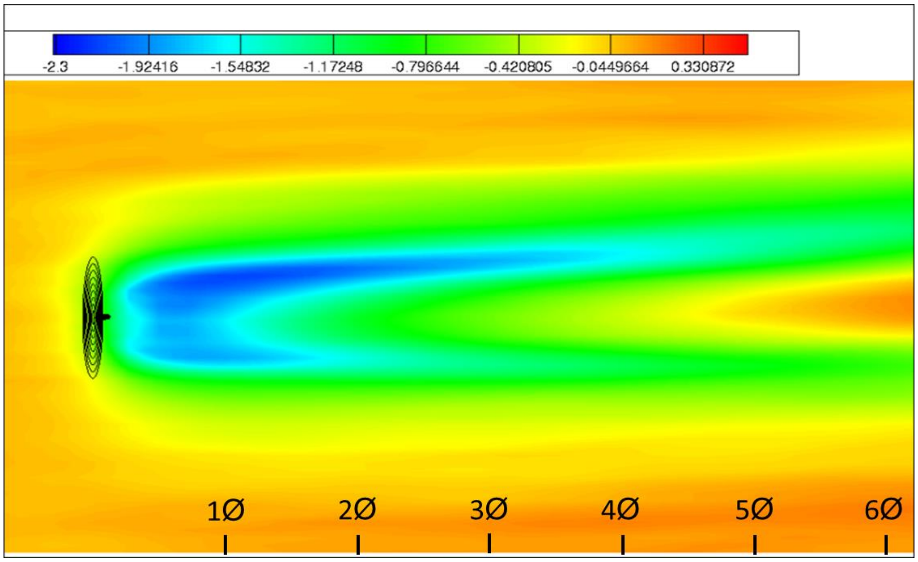

Figure 4.22 Contour plots of time-averaged relative humidity difference in a horizontal plane section passing through the lower turbine tip height and parallel to the streamwise direction (the legend shows changes in the relative humidity from the upstream level).

Figure 4.23 juxtaposes the measured difference between upstream and downstream vertical profiles of relative humidity and LES output at 100 m downstream. Figure 4.24 shows numerous measured vertical profiles and LES output at 200 m downstream. All observed hub height wind speeds were in the 4 – 7 m/s range and observed temperature inversions in the first 100 m ranged from a modest 0.5 °C to a robust 4 °C. This range in the level of thermal stratification, along with the instantaneous nature of the observations and time-averaging of the LES output, is what differences between observed and numerical results are primarily attributed to. In support of this, it is seen that LES output and observations align much closer in Figure 4.23. Additionally, Figure 4.24 shows a tighter grouping of the more robust levels of thermal stratification and a displaced LES profile with weaker thermal stratification. This speaks to the increased/decreased role that enhanced vertical mixing by the wind turbine plays when the atmosphere is less/more well-mixed. However, despite greatly varying inversion strengths, albeit similar hub height wind speeds, the disparate LES and observed conditions all show very good qualitative agreement. Of particular note is the similar 'nose' like feature, representing the region of largest humidity decrease, in all observed data and LES outputs. Its location, slightly below the lower turbine tip height, along with the location of the inflection between regions of decreased and increased relative humidity near the hub height, are consistent across all results.

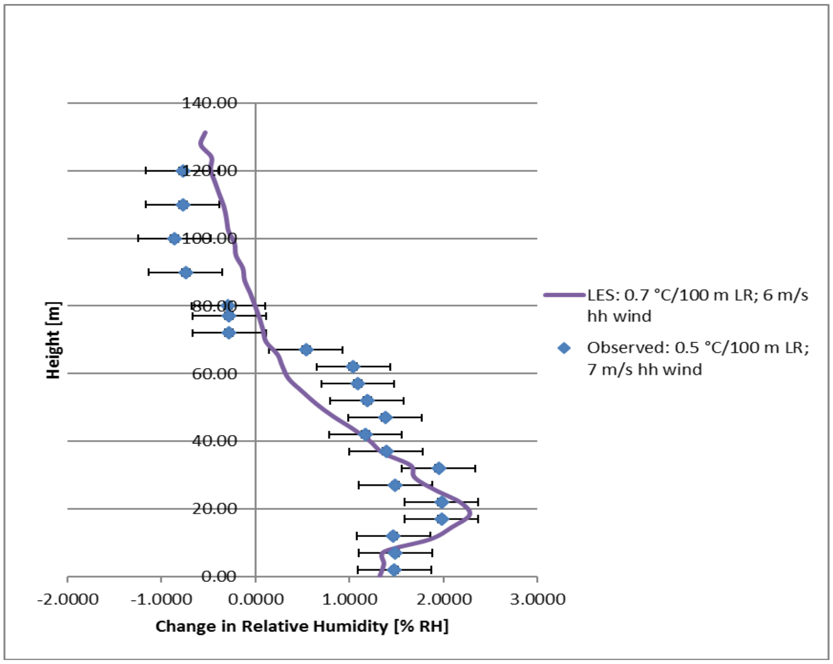

Figure 4.23 LES time-averaged output and observed changes in relative humidity (upstream minus downstream), as a function of height, at 100 m downstream.

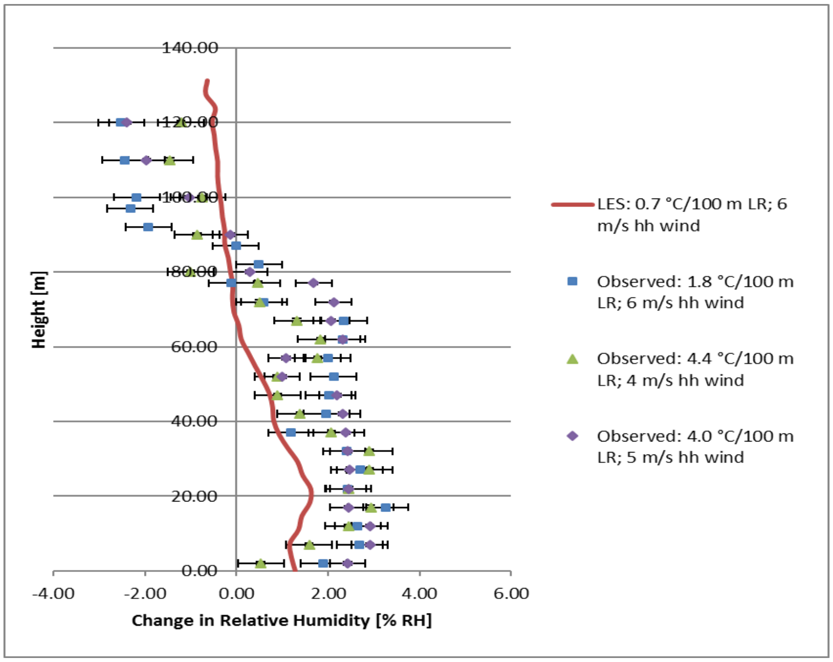

Figure 4.24 LES time-averaged output and observed changes in relative humidity (upstream minus downstream), as a function of height, at 200 m downstream.

Comparisons between time-averaged LES output and downstream measurements, at the lower turbine tip height, to 500 m are shown in Figure 4.25. Again, flights were limited to 500 m downstream in order to comply with FAA regulations mandating that VLOS be maintained with the UAV. Both LES output and calculation of measured differences suggest a steep gradient immediately aft of the turbine that is followed by a more gradual downstream recovery. All scenarios ultimately show a similar magnitude of recovery with 2/3 or greater, of the maximum deficit being recovered by 500 meters. Again, the numerical data suggests a maximum decrease in relative humidity around 1 rotor diameter downstream while all measurement scenarios indicate a maximum decrease just downstream of 1 rotor diameter.

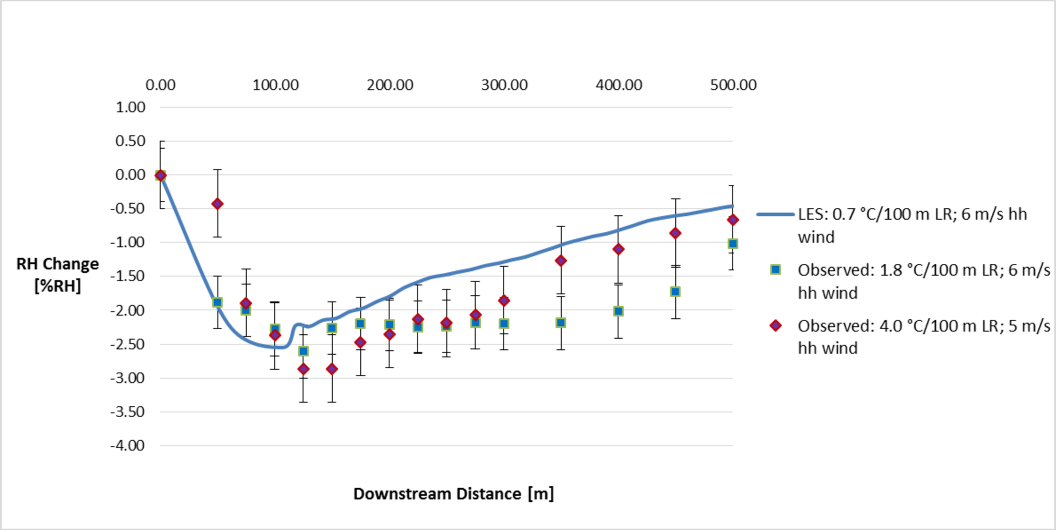

Figure 4.25 LES time-averaged output and observed changes in relative humidity (upstream minus downstream) as a function of downstream distance at the lower turbine tip height.

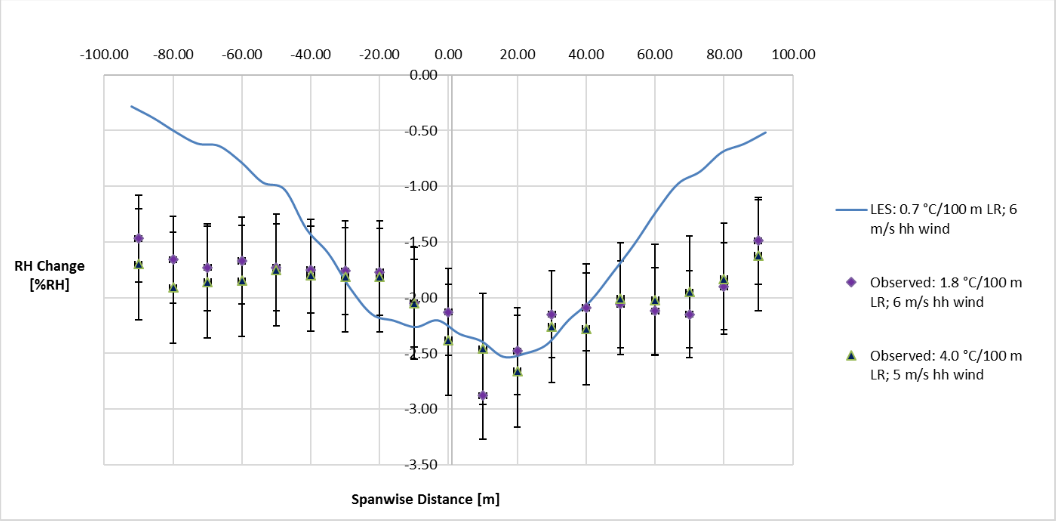

Figure 4.26 LES time-averaged output and observed changes in relative humidity (upstream minus downstream) as a function of lateral distance at the lower turbine tip height.

Lateral measurements, displayed in Figure 4.26 with analogous LES time-averaged output, are for points at the lower turbine tip height and 2 rotor diameters downstream. Of particular interest is the similar asymmetry present in both the LES results and experimental measurements. This asymmetry is the fingerprint of the split humidity ‘wake’ evident in the contour plot of Figure 4.22. Each investigation shows the maximum decrease in relative humidity is located just to the right side of the wake’s centerline. Both the LES and measurement suggest that this deficit remains greater across all of the right-hand side. This asymmetry, with greater deficits on the right-hand side, is presumed to be the result of the turbine blades’ descent, and its delivery of drier air from aloft, on the right-hand side of its clockwise rotation along with the wake’s interaction with the ground. It is noted that numerical and observed data agree best behind the rotor swept area. Therefore, an explanation for the discrepancy between numerical and observed results outside of this region may be tied to the simulated wake expansion.

While good qualitative agreement exists between the numerical and observed data, the small quantitative differences can be attributed to a number of factors. Predominately, differences are attributed to discrepant levels of thermal stratification. The more the atmosphere is already mixed, the smaller the role that wind turbines play in enhanced mixing. However, secondarily, differences can also be explained by specific modeling assumptions. Numerical simulations were constructed with parameterized wind turbines that use a representative power coefficient from the literature. With an exact value, or turbine blade specifics, unavailable from the turbine manufacturers, the only turbine characteristics directly matched were rotor diameter, hub height and the thrust coefficient. Additionally, simulated inflow lapse rate profiles for both temperature and humidity were smoothed and made to be only representative of snapshot measurements taken during a given suite of flight profiles. Finally, while field measurements were made at a locale selected for having similar cultivar type, surface moisture characteristics and topography, surface-level flux measurements were not made and were assumed to be uniform within the simulation. However, even with these assumptions, all distinctive characteristics, related to changes in humidity, observed in field measurements are also displayed by the LES.

A wind turbine's power coefficient represents the ratio of the electrical power produced by the wind turbine to the total energy available at a given wind speed [103]. This parameter is widely used by the wind energy industry to measure wind turbine efficiency. With only the thrust coefficient available from the turbine manufacturer, a representative value for the power coefficient was obtained from the literature for the numerical investigation. For all baseline simulations, a power coefficient of 0.5 was used. To analyze the impact that the power coefficient has on changes to downstream relative humidity, an analogous simulation around a single wind turbine was executed with a substituted power coefficient value of 0.65. The change in humidity, as a function of height, for each power coefficient is shown in Figure 4.27. Adjacent to the surface, the increase in the power coefficient results in a very small decrease in the magnitude of change of near-surface humidity. Where the greatest magnitude of humidity change was previously noted for both measurement and numerical output, slightly below the lower turbine tip height, this difference disappears. The impact of a varying power coefficient seems to have no change on the trend of humidity change throughout the vertical profile and no impact within the region of increased humidity in the vicinity of the upper turbine tip height.

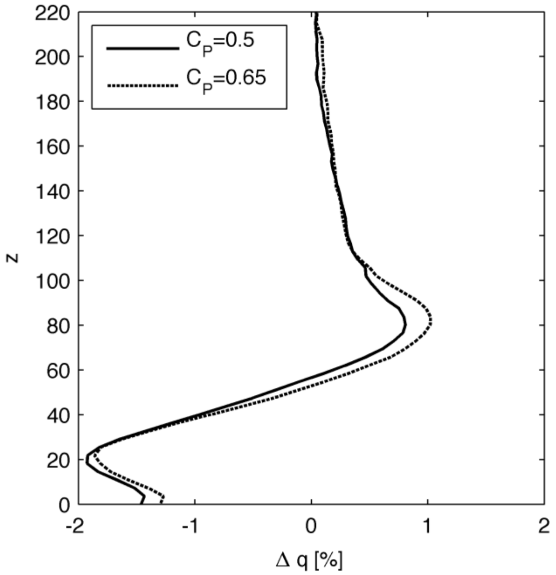

Figure 4.27 Plot of time-averaged LES output of humidity change at 100 m downstream as a function of height for a power coefficient of 0.5 and 0.65.

While field measurements were made at a locale selected for having similar cultivar type, surface moisture characteristics and topography, surface-level flux measurements were not made and assumed to be uniform within the simulation. A constant specific humidity flux of 0.01 g/kg•m/s was imposed at the ground level for all baseline simulations. In order to obtain insight into how a varying value of humidity flux impacts changes to relative humidity, an analogous simulation was run with a different surface moisture flux value. The baseline value of 0.01 g/kg•m/s is contrasted with a doubling of this value, 0.02 g/kg•m/s, in Figure 4.28. While the region of increased relative humidity in the vicinity of the top turbine tip height is observed to not be impacted by a varying surface moisture flux value, the region of maximum relative humidity decrease, slightly below the lower turbine tip height, is significantly impacted.

This contrast, albeit smaller, is present all the way down to the surface. Notably, while the magnitude of humidity change is impacted by the differing flux value the humidity change trend, including the previously noted ‘nose’ shaped region below the lower turbine tip height, is unaffected. These observations indicate that an increase of surface moisture flux can increase the magnitude of humidity change but that the location where these changes occurs remains generally unchanged. Further, while all distinctive characteristics related to humidity change remain consistent, it is noted that the value chosen for the broader numerical investigations in this work produces the most conservative magnitude of change.

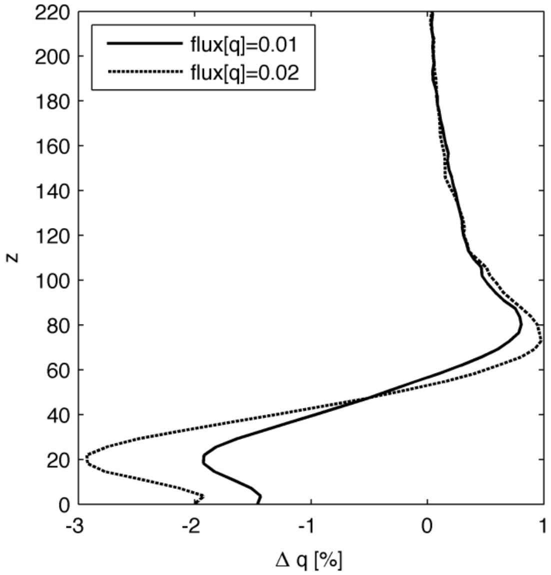

Figure 4.28 A plot of time-averaged LES output humidity change at 100 m downstream as a function of height for a varying surface moisture flux of 0.01 g/kg•m/s and 0.02 g/kg•m/s.

4.3 Numerical Results within a Wind Turbine Array

4.3.1 Stable Atmospheric Boundary Layer

Results from simulations of a stable WTABL, consisting of a 6 x 4 turbine array in aligned and staggered configurations, are considered next. The main objective is to determine the effect of compounding wakes on near-surface relative humidity within the wind farm for two different thermal stratifications ($\Delta\theta=1$ K and $\Delta\theta=2$ K) and two configurations (aligned and staggered turbines). The two different thermal stratifications represent an increase of potential temperature of 1° and 2° per 800 meters. The staggered array displaces every other row of wind turbines. The rotors are laterally displaced so that a distance equal to 45% of the rotor diameter separates the lateral extent of the rotor swept areas. Because a periodic boundary condition is imposed in the lateral direction, the WTABL is taken to be infinitely wide. In Figure 4.29, contour plots of the instantaneous streamwise velocity in a horizontal plane sectioning the flow domain through the hubs are shown corresponding to both aligned (part a) and staggered (part b) configurations. Both configurations seem to suggest that the compounding wakes introduce mixing in the downstream, which is expected to impact the variation of scalar quantities such as relative humidity and potential temperature.

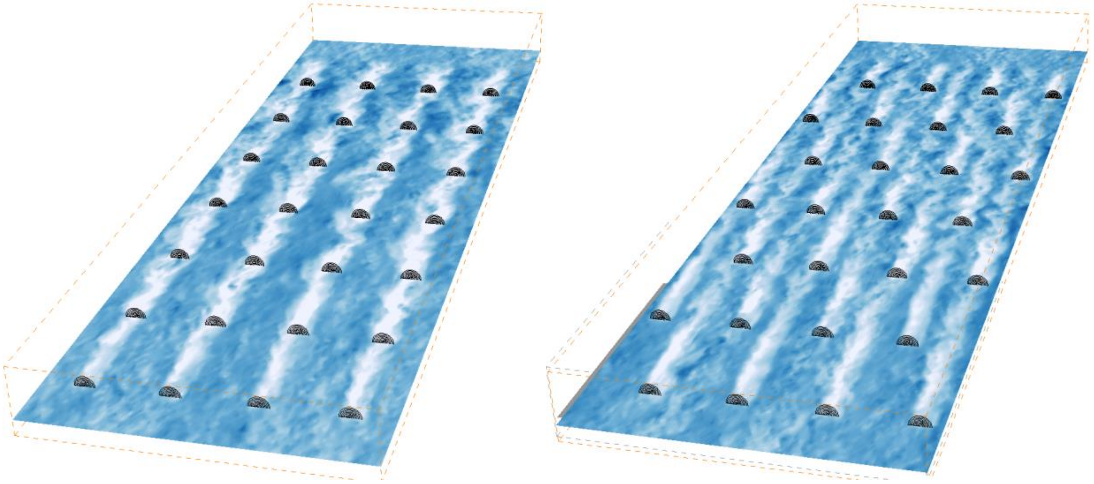

Figure 4.29 Contour plots of instantaneous streamwise velocity in a horizontal plane passing through the hubs: a) aligned configuration; b) staggered configuration.

Since scalars quantities, such as humidity, satisfy transport equations, it is expected that the main contributor to the variation of relative humidity or potential temperature within the wind farm is the momentum flux, which is affected considerably by the rotating rotors. These modifications bring about nuanced changes to relative humidity in all three spatial directions, throughout the WTABL. In Figures 4.30 and 4.31, contour plots in vertical slices taken across the flow domain at fixed downstream distances and isosurfaces of decreased relative humidity provide insight into these changes.

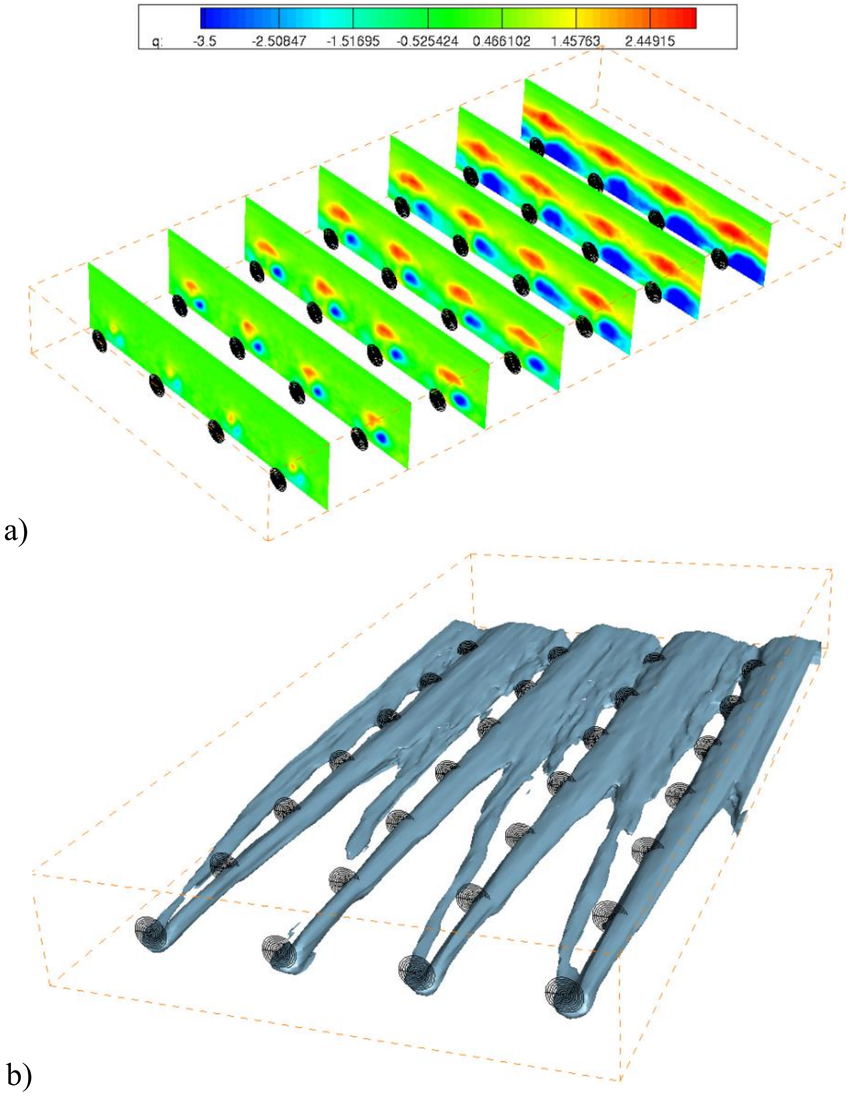

Figure 4.30 a) Contour plots of time-averaged relative humidity difference in vertical plane slices at fixed downstream distances within an aligned turbine array (the legend shows changes in the relative humidity with respect to the upstream level); b) Isosurface of decreased relative humidity for the aligned configuration.

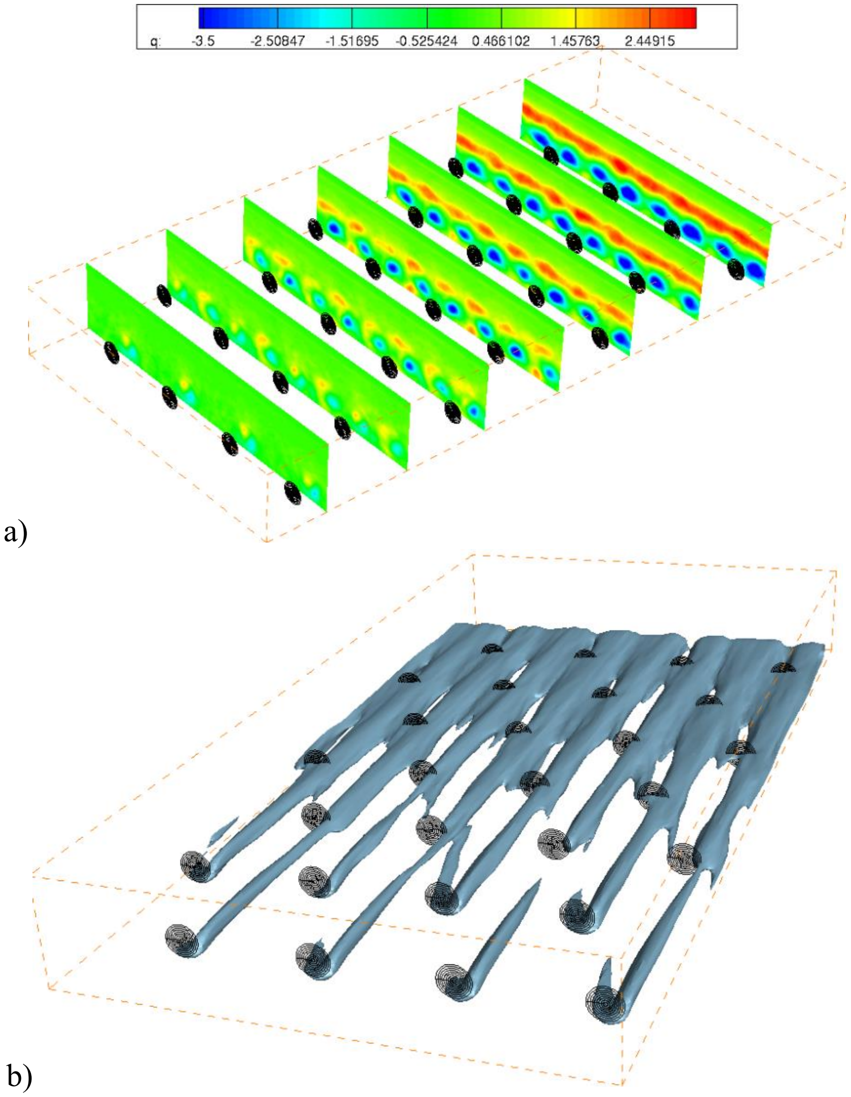

Figure 4.31 a) Contour plots of time-averaged relative humidity difference in vertical plane slices at fixed downstream distances within a staggered array (the legend shows changes in the relative humidity with respect to the upstream level); b) Isosurface of decreased relative humidity for the staggered configuration.

As observed and simulated results around a single wind turbine previously indicated, enhanced vertical mixing, in the presence of a positive humidity lapse rate, delivers moist surface air upward and transports drier air found aloft downward. Upstream vertical cross sections in the domain show how drier air aloft is first brought downward by the descending blades on the right-hand side, and moist air is delivered upward on the left-hand side, of the clockwise rotating turbine. Subsequent streamwise slices through the domain illustrate how these areas of humidity change grow in magnitude and, most predominately, in a lateral manner in the direction of turbine rotation. The region of increased relative humidity grows unencumbered from left to right at, and above, the upper turbine tip height. The region of decreased relative humidity near the lower turbine tip height develops with interference from the underlying surface. As the area of decreased relative humidity grows in the direction of rotation, the region is broken by the vortices' interaction with the ground. Here the surface physically obstructs and slows the flow, hence changing the flow dynamics. Figure 4.31 shows how these breaks, within a staggered configuration, initially host an area of entrainment of moist near-surface air up into the vortex before being cutoff further downstream by the growth of the deficit area.

Experimental measurements and LES results for both one turbine and the 6 x 4 array show that there is a tendency for the humidity "wake" to split in the downstream, as the bottom of the vortex interacts with the ground. Greater humidity deficits occur within two "arms" that grow in all directions (this can be also seen in Figure 4.30b for the aligned WTABL). This suggests, from a humidity perspective, that a staggered wind turbine array may provide different downstream humidity changes. Figures 4.30 and 4.31 show the difference between the two configuration layouts. While inspection of each figure shows similarities in flow dynamics and changes to relative humidity, and an expansion and accumulation of wakes with downstream distance, a reduction in the volume of air with modified relative humidity is realized in both the lateral and vertical directions for the staggered configuration. Figures 4.30 and 4.31 also reveal how wake expansion supports the growth of regions of change in directions counter to the turbine's rotation, along with growth in the vertical direction. When the array is fully transited, a broad and continuous volume of drier air exists below a similar mass of moister air.

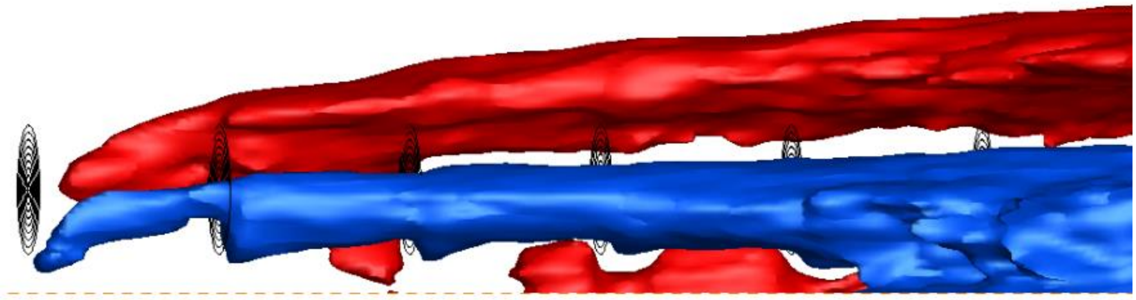

Figure 4.32 Isosurfaces of decreased (blue) and increased (red) relative humidity for an aligned single column of turbines (streamwise length scaled by 1/5).

A side view of isosurfaces of decreased (0.8%) and increased (0.3%) relative humidity is given in Figure 4.32 and illustrates how each of these regions of change also experience continuous uplift. The region of increased relative humidity rises well above the upper edge of the turbine disk by the fourth row, while the region of decreased humidity slightly exceeds the hub height by the third row. Also evident are the areas of entrainment of moist near-surface air into the wake immediately upstream of the third, fourth and fifth row of turbines. The entrainment of moist surface air is eventually cutoff as the region of decreased humidity grows in size. While the uplifting associated with the region of decreased humidity nearer to the ground is modest, the uplift associated with the region of increase higher up is much more significant. This is most likely attributed to the uninhibited upward mixing by the largest turbulent eddies that are more restricted closer to the ground.

In the context of the aforementioned qualitative assessment, a quantitative comparison is made between different atmospheric stratifications in terms of the streamwise, lateral and vertical distributions of averaged relative humidity. Because it appears that the cumulative increase or decrease of humidity in the downstream does not occur at a constant elevation, Figures 4.33 - 4.35 plot distributions of laterally averaged minimum and maximum humidity (taken in the vertical direction) given as:

$$\Delta q_{min}(\mathrm{x})=\frac{1}{(y_2-y_1)}\int_{y_1}^{y_2}\min_{0<z<z_h}[q_{up}(x,y,z)-q(x,y,z)]dy \tag{4.4}$$

$$\Delta q_{max}(\mathrm{x})=\frac{1}{(y_2-y_1)}\int_{y_1}^{y_2}\max_{0<z<z_h}[q_{up}(x,y,z)-q(x,y,z)]dy \tag{4.5}$$

where $y_1$and y_2 are the coordinates of lateral boundaries, z_h is the height of the domain, and q_{up} is the humidity two diameters upstream of the first row of turbines. In Figure 4.33, comparisons between the aligned and staggered configurations are plotted for a thermal stratification of Δθ=2 K. It is evident from this figure that the aligned configuration is more effective in altering the decrease of relative humidity below the hub height, and less effective above. Apparently, the decrease and increase in relative humidity does not seem to attain a fully developed state, which is an investigation that would require the extension of the domain in the downstream direction and an increase in the number of rows and grid points.

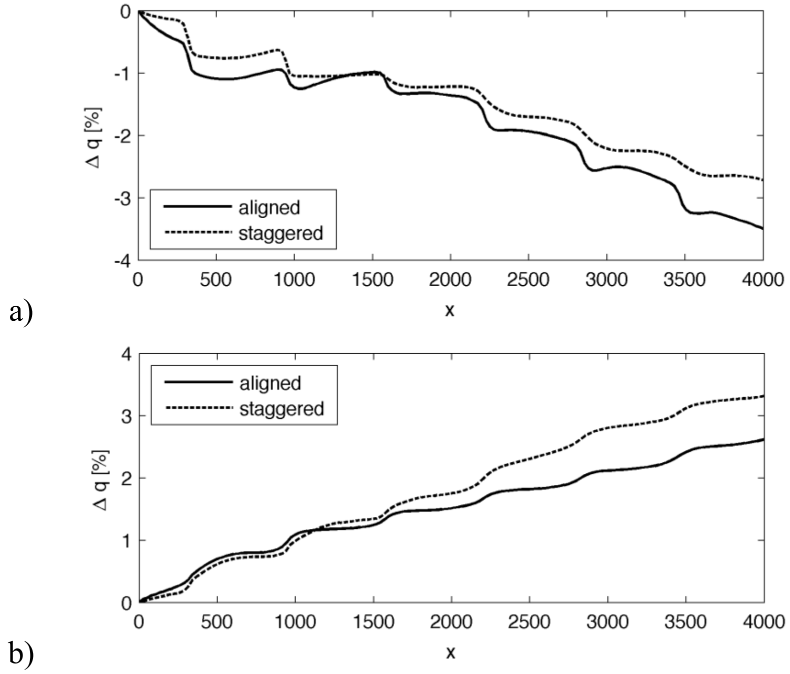

Figure 4.33 Variation of the relative humidity in the streamwise direction for a thermal stratification Δθ=2 K: a) decrease (below the hub); b) increase (above the hub).

In Figures 4.34 and 4.35, distributions of the integrated maximum and minimum humidity are plotted and compared in terms of thermal stratification variation, for both aligned and staggered configurations respectively. Thermal stratification does seem to have a non-negligible impact on the humidity development in the downstream; by increasing the thermal stratification, the region of both decrease and increase in humidity becomes greater in magnitude. This suggests that the wind turbines' enhancement of vertical mixing plays a larger role when the ABL is more strongly thermally stratified and consequently less well mixed.

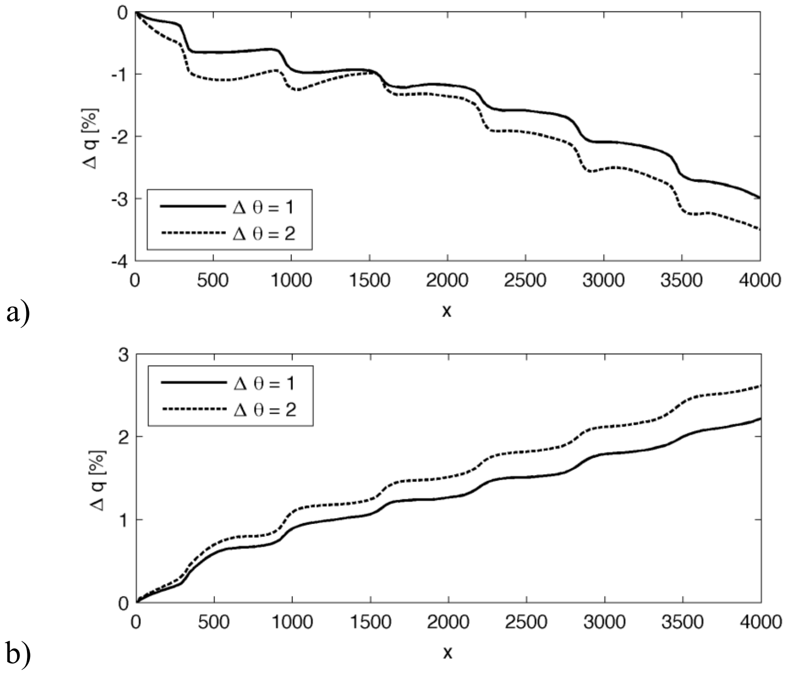

Figure 4.34 Variation of the relative humidity with streamwise direction for the aligned configuration: a) decrease (below the hub); b) increase (above the hub).

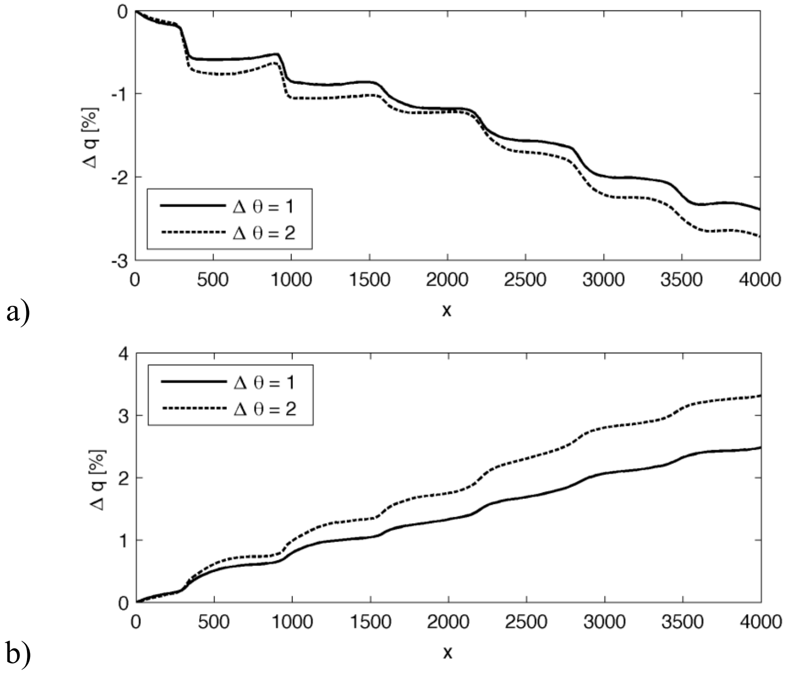

Figure 4.35 Variation of the relative humidity with streamwise direction for the staggered configuration: a) decrease (below the hub); b) increase (above the hub).

In Figures 4.36 through 4.39, distributions of the maximum and minimum humidity are plotted as a function of lateral direction for both wind farm configurations and thermal stratifications. The continual lateral expansion of the accumulated wake with downstream distance, as the magnitude of change concurrently increases, is readily apparent for both array configurations and stratifications. However, as might be anticipated, the accumulated wake from the staggered configuration does not grow as fast and is more constrained in its lateral dimension. Wake expansion is much more readily apparent for the aligned configuration. This ultimately results, for the aligned array, in a broader and more continuous area of decreased relative humidity near the ground downstream of the array. Unencumbered by the surface, the rate of lateral growth for the area of increased relative humidity aloft is faster for all stratifications with the staggered array and a more continuous area of increased relative humidity is created. Analyzing near surface areas of change against areas of change aloft for all stratifications and array configurations, the ground's interaction with the large-scale vortex structures clearly stymies the growth and continuity of the near-surface area of change compared to its counterpart aloft.

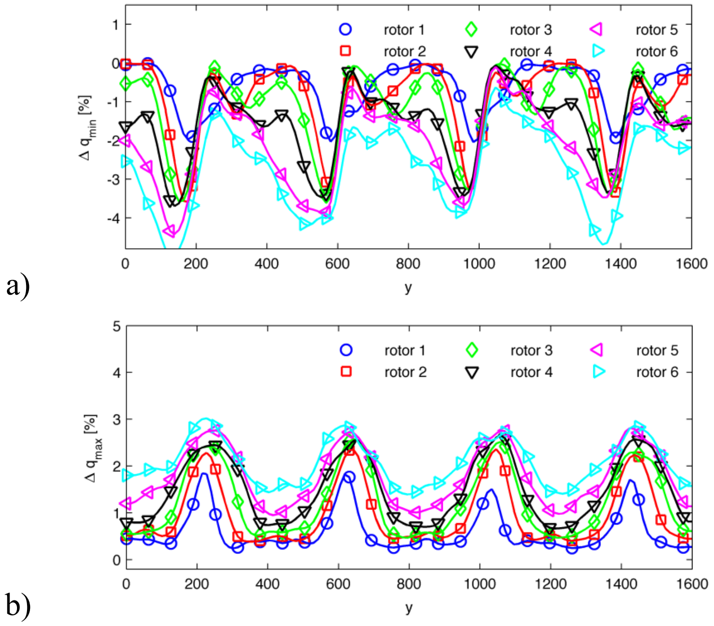

Figure 4.36 Variation of relative humidity with lateral direction for the aligned configuration, Δθ=1 K (profile extracted 2 rotor diameters downstream of the noted rotor): a) decrease (below the hub); b) increase (above the hub).

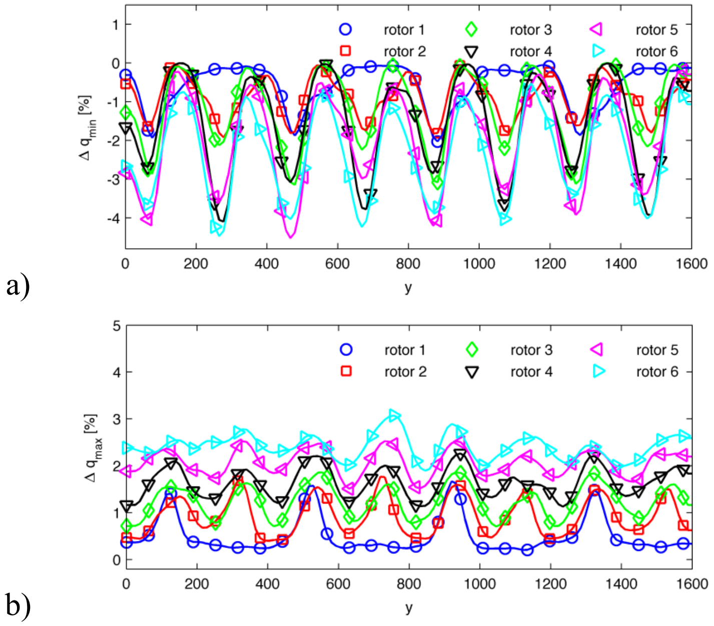

Figure 4.37 Variation of relative humidity with lateral direction for the staggered configuration, Δθ=1 K (profile extracted 2 rotor diameters downstream of the noted rotor): a) decrease (below the hub); b) increase (above the hub).

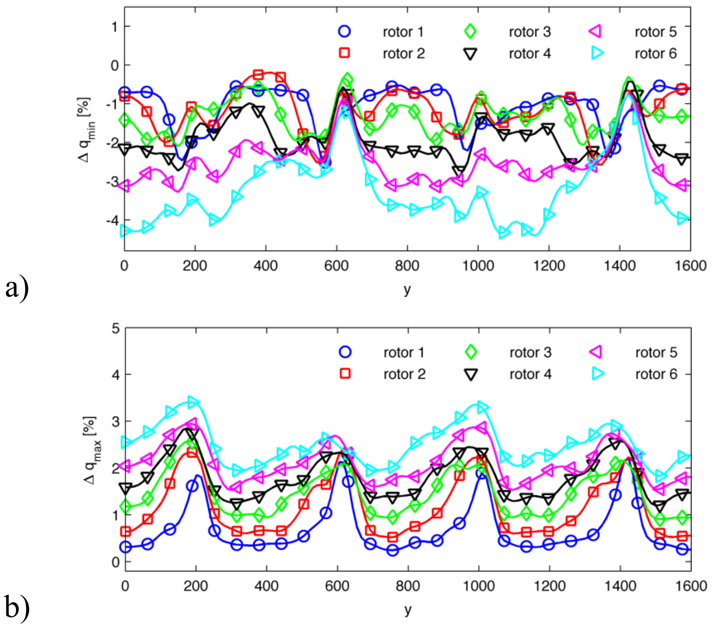

Figure 4.38 Variation of relative humidity with lateral direction for the aligned configuration, $\Delta\theta=2$ K (profile extracted 2 rotor diameters downstream of the noted rotor): a) decrease (below the hub); b) increase (above the hub).

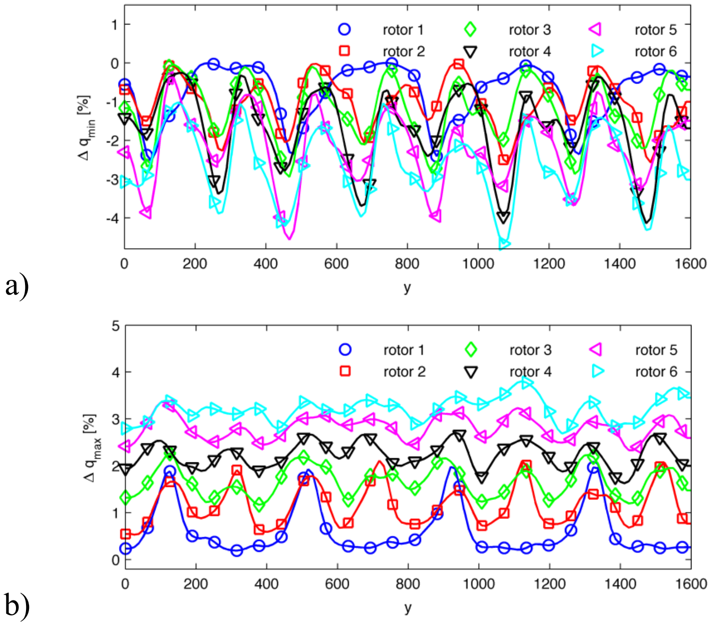

Figure 4.39 Variation of relative humidity with lateral direction for the staggered configuration, $\Delta\theta=2$ K (profile extracted 2 rotor diameters downstream of the noted rotor): a) decrease (below the hub); b) increase (above the hub).

The uplifting of the regions of humidity increase or decrease is also revealed through profiles of averaged relative humidity in the vertical direction for different downstream locations within the wake. This is accomplished in Figures 4.40 – 4.43, where these vertical profiles are plotted not in the center of the wake but in two lateral locations to the left and right sides of the rotor. All vertical profiles are extracted at 2 diameters downstream from the noted rotor. These figures also show that the amount of relative humidity increase above the rotors is approximately the same between the left and right sides of the wake; however, there is considerable disparity between the amounts of decrease below the hub. The elevation associated with the minimum decrease is also significantly lower on the left side of the wake. Inspection also indicates that the change in relative humidity in proximity to the ground, on the left side of the wake for both thermal stratifications, is negative for the first 1-2 rows of turbines, positive for the next few rows, and reverts back to being negative for the last rows of turbines. On the right side of the wake, the switch between signs occurs only for the greater thermal stratification. The smaller thermal stratification yields predominately a relative humidity decrease. Figures 4.40 – 4.43 also suggest that the right-side inflection point, characterizing the switch between the areas of decreased and increased relative humidity, is slightly above the hub height (between z=90 m and z=110 m) while the location of the inflection point on the left side of the wake is not as clear.

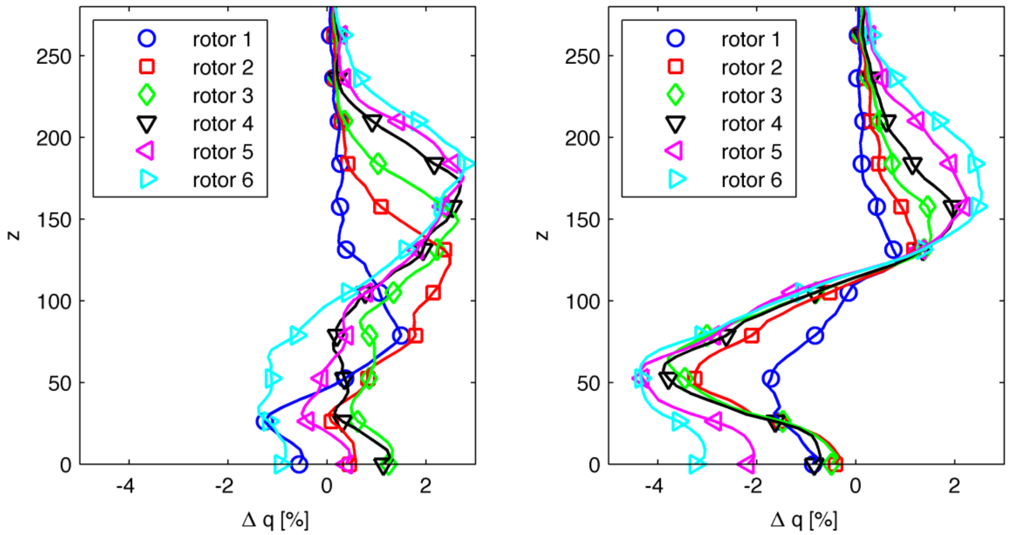

a) b)

Figure 4.40 Variation of the relative humidity with vertical direction for the aligned configuration, Δθ=1 K: a) left side of the wake; b) right side of the wake.

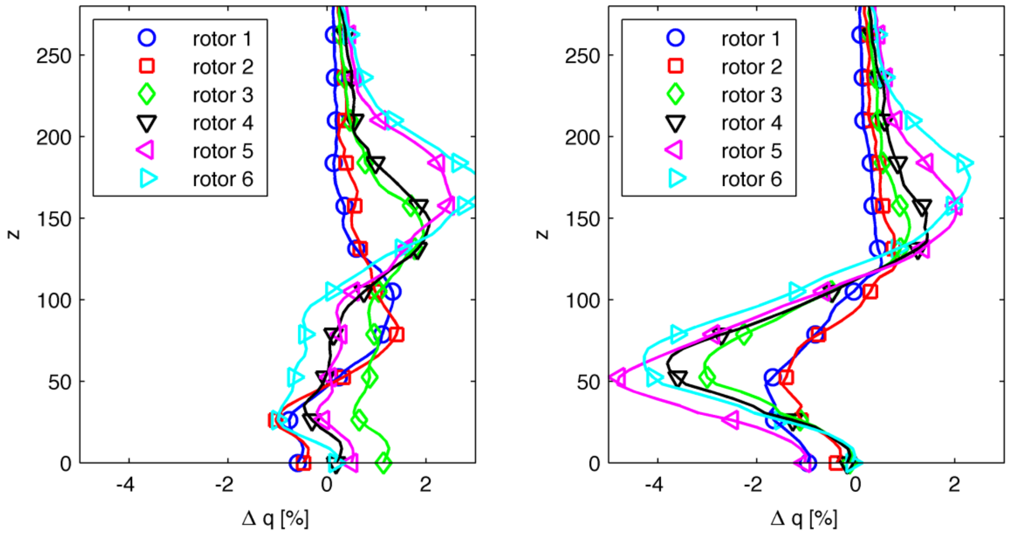

a) b)

Figure 4.41 Variation of the relative humidity with vertical direction for the staggered configuration, Δθ=1 K: a) left side of the wake; b) right side of the wake.

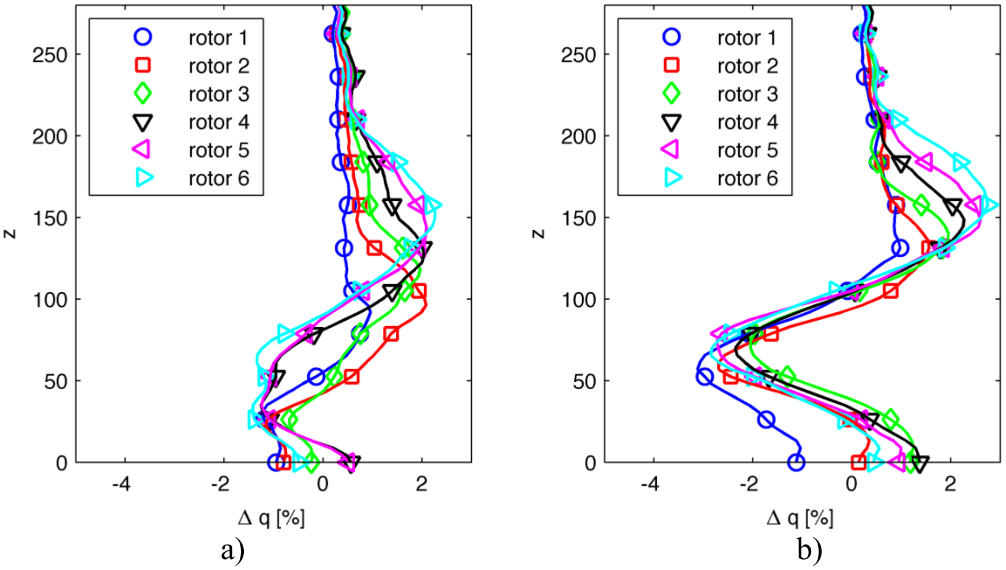

a) b)

Figure 4.42 Variation of the relative humidity with vertical direction for the aligned configuration, Δθ=2 K: a) left side of the wake; b) right side of the wake.

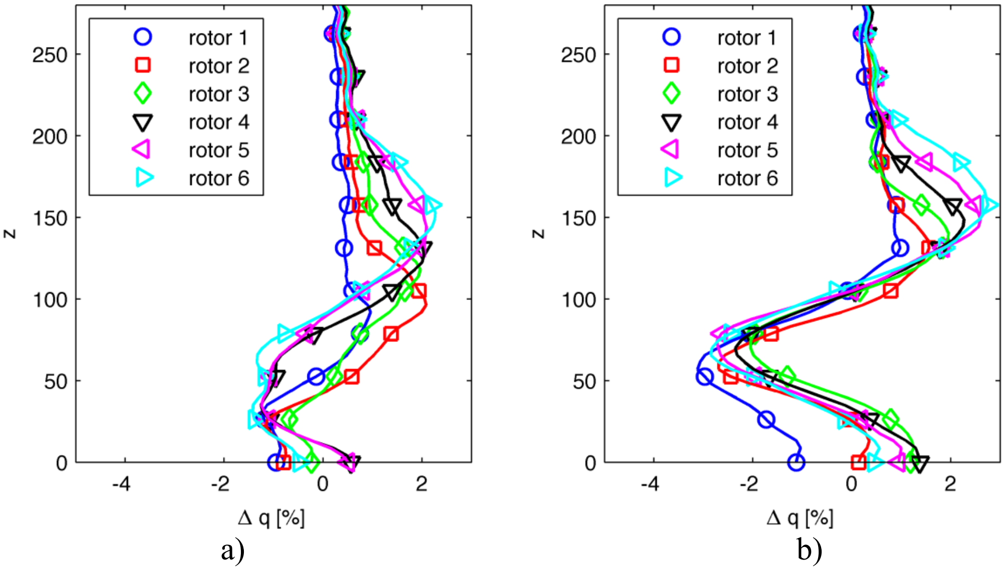

a) b)

Figure 4.43 Variation of the relative humidity with vertical direction for the staggered configuration, Δθ=2 K: a) left side of the wake; b) right side of the wake.

4.3.2 Unstable Atmospheric Boundary Layer

A single unstable scenario is analyzed with both an aligned and staggered 6 x 4 WTABL configuration in order to look at, and compare, the effect of a compounding wake on relative humidity. The unstable atmospheric scenario is created with a potential temperature lapse rate of 1 °K per 800 m. The contour plots of Figure 4.44 display the instantaneous streamwise velocity in a horizontal plane sectioning the flow domain at the turbine hub height. Figure 4.44a shows the flow through an aligned array and Figure 4.44b illustrates the flow through the staggered configuration. Each figure displays how the enhanced mixing associated with the unstable environment brings about faster wake recovery. Of particular interest are the effects of large thermals and plumes, whose size can reach the height of ABL, that develop in unstable conditions and propagate with the mean flow. When present, these structures can locally distort the direction of the mean flow. This distortion is observed in the white patch on the left side of the domain for the aligned case and on the right side for the staggered case. The orientation of the wakes can fluctuate, both left and right, as these structures move through the wind farm. Careful inspection of both figures show that unaligned wakes point toward regions previously influenced by passage of these structures.

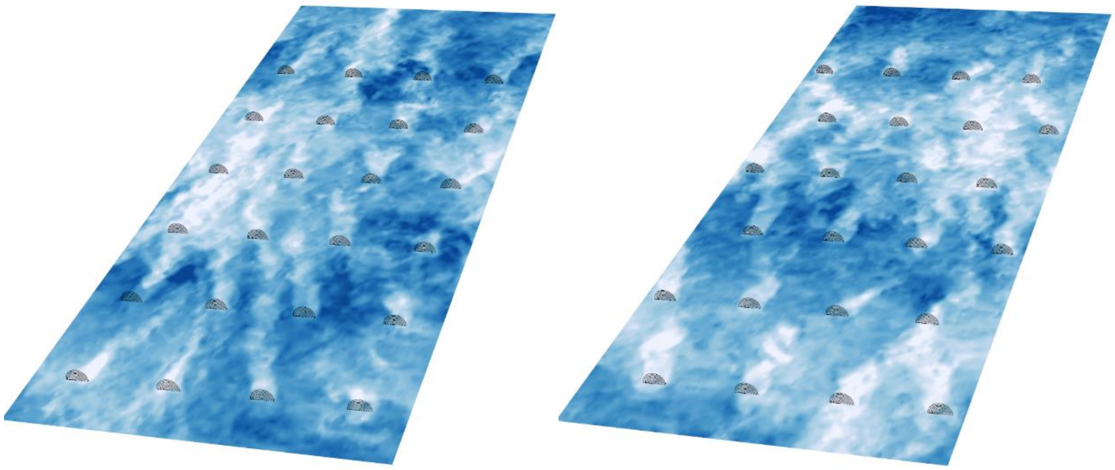

Figure 4.44 Contour plots of instantaneous streamwise velocity in a horizontal plane passing through the hubs of an unstable WTABL: a) aligned configuration; b) staggered configuration.

Turbulence found within an unstable ABL is the result of both wind shear and buoyancy but is predominately driven by thermal buoyancy. This thermal buoyancy gives rise to the aforementioned vertical structures. The support for this vertical enhancement can be observed in the contour plots that lie within vertical slices taken at regular downstream intervals in Figures 4.45 and 4.46.

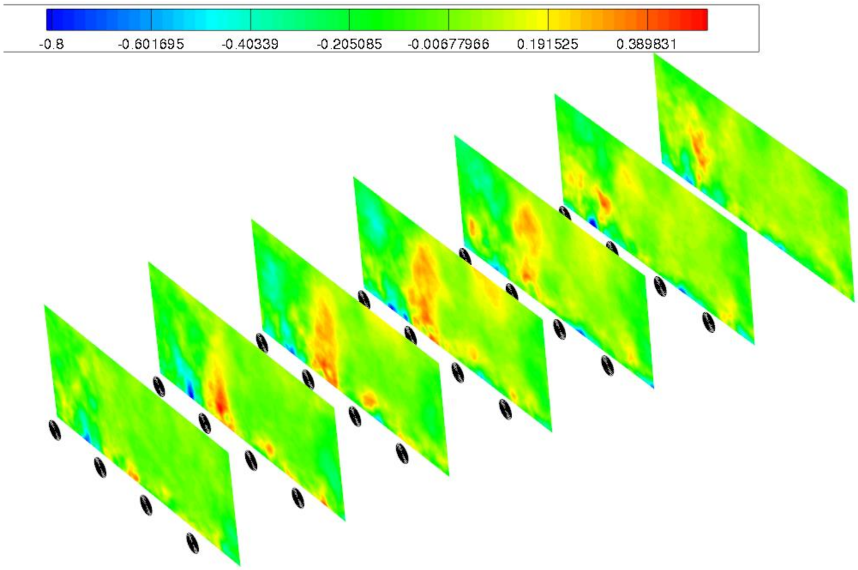

Figure 4.45 Contour plots of time-averaged relative humidity difference in vertical plane slices at fixed downstream distances within an aligned turbine array and unstable environment (the legend shows changes in the relative humidity with respect to the upstream level)

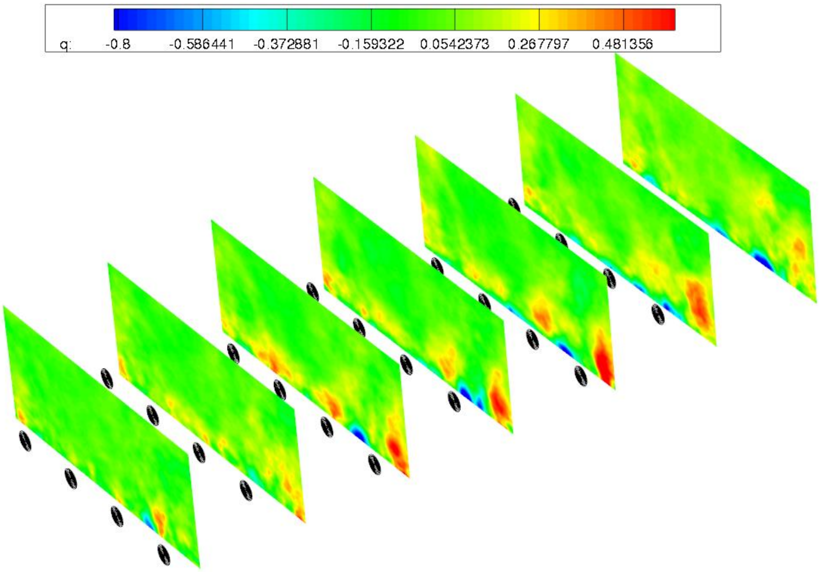

Figure 4.46 Contour plots of time-averaged relative humidity difference in vertical plane slices at fixed downstream distances within a staggered array and unstable environment (the legend shows changes in the relative humidity with respect to the upstream level)

Contrasting Figures 4.45 (aligned) and 4.46 (staggered) with the corresponding stable plots, Figures 4.30a (aligned) and 4.31a (staggered), it is apparent that vertical mixing is enhanced in the presence of atmospheric instability. The greater boundary layer depth associated with the unstable ABL, well above the upper turbine tip height, is also evident as regions of humidity increase extend well above the areas of increase observed with the stable stratification. However, inspection of the magnitude of humidity increase and decrease show the reduced effect that the wind turbines have on the already well-mixed ABL. With changes well below 0.5%, the magnitude of change is much smaller than the changes observed for either of the stable scenarios. While the previously discussed impetus for the development of regions of change, descending blades mixing down drier air and ascending blades mixing up moister air, is the same, the more robust background turbulence within the unstable WTABL more quickly erodes the areas of change. This dynamic results in the absence of large, well-defined regions of downstream change. This is especially true for the staggered configuration where “channels” of humidity change are not reinforced by the next row of turbines and have ample streamwise distance for dilution by atmospheric mixing.

With the enhanced mixing associated with an unstable atmosphere, a more muted downstream change in relative humidity is expected relative to the change realized in a stable environment. Figure 4.47 shows the streamwise distribution of averaged relative humidity change (calculated as in the stable regime by means of Equations 4.4 and 4.5) for both an aligned and staggered configuration, and thus allows for a quantitative comparison to the analogous stably stratified distributions shown in Figure 4.33. The magnitude of the decrease in relative humidity in the unstable scenario appears to be independent of the array configuration but is a full order of magnitude smaller than the change observed in the stable environment. Similar to the stable results, the staggered configuration is more effective at altering the increase in relative humidity above the turbine hub height; however, again, the humidity change observed is over an order of magnitude less than the change brought about in the stably stratified regime. In contrast to either of the stable scenarios, the complementary enhanced mixing brought about by the atmosphere and the WTABL results in a quasi-stationary-state value of humidity change that is realized fairly early on within the array (e.g., after the third row in Figure 4.47b).

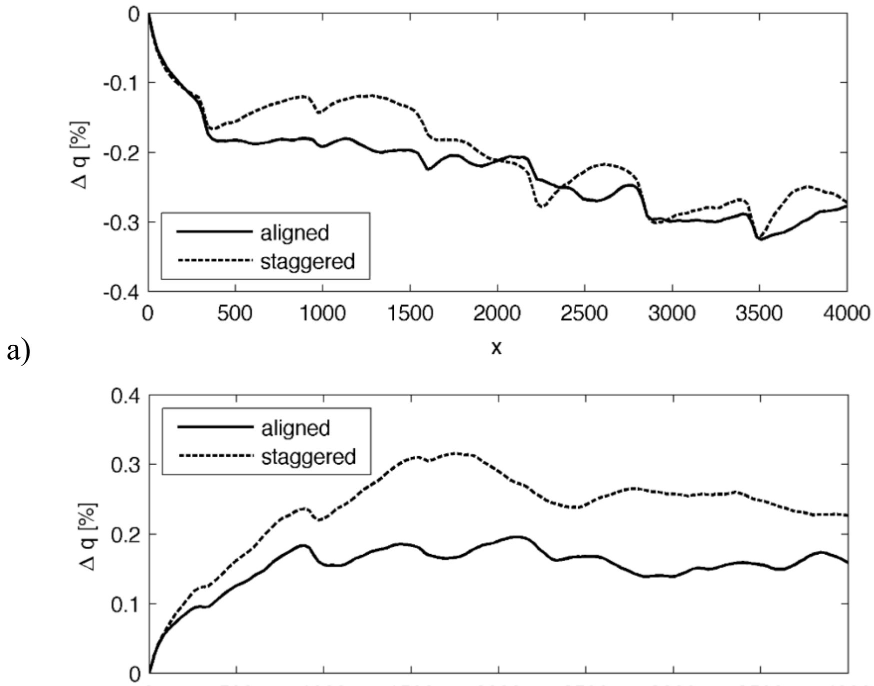

Figure 4.47 Variation of the relative humidity in the streamwise direction for an unstable stratification a) decrease (below the hub); b) increase (above the hub).

Figures 4.48 and 4.49 provide the distributions of the maximum and minimum humidity change as a function of lateral distance for both wind farm configurations in the unstable environment.

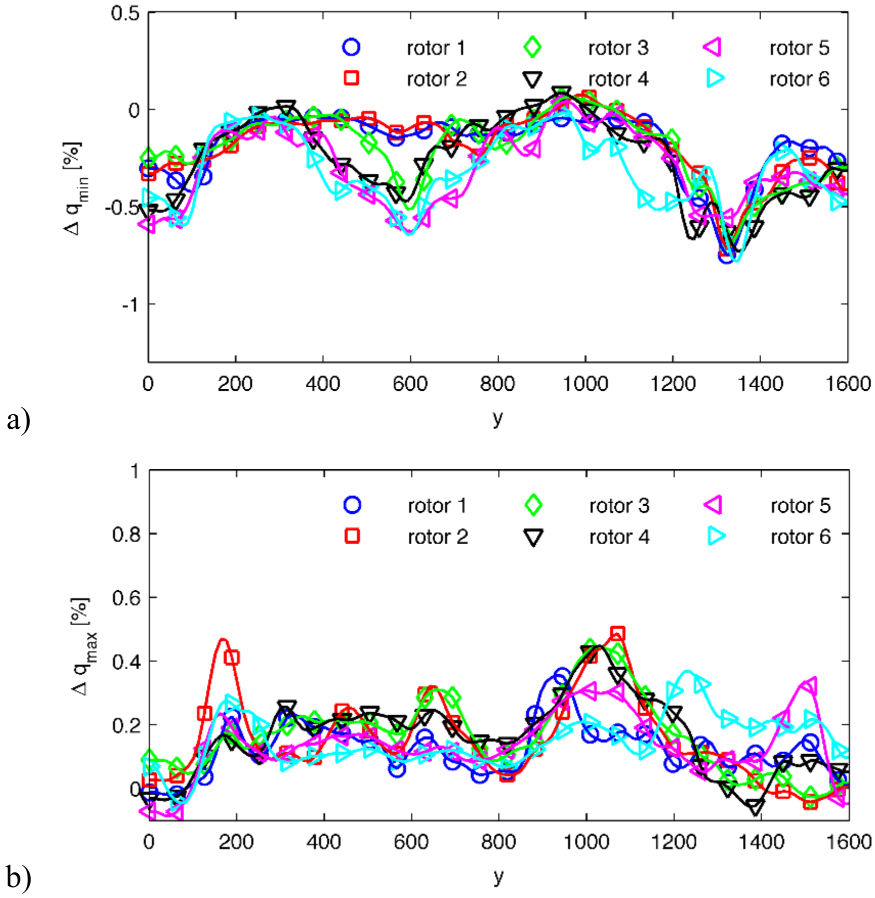

Figure 4.48 Variation of relative humidity with lateral direction for the aligned configuration (profile extracted 2 rotor diameters downstream of the noted rotor): a) decrease (below the hub); b) increase (above the hub).

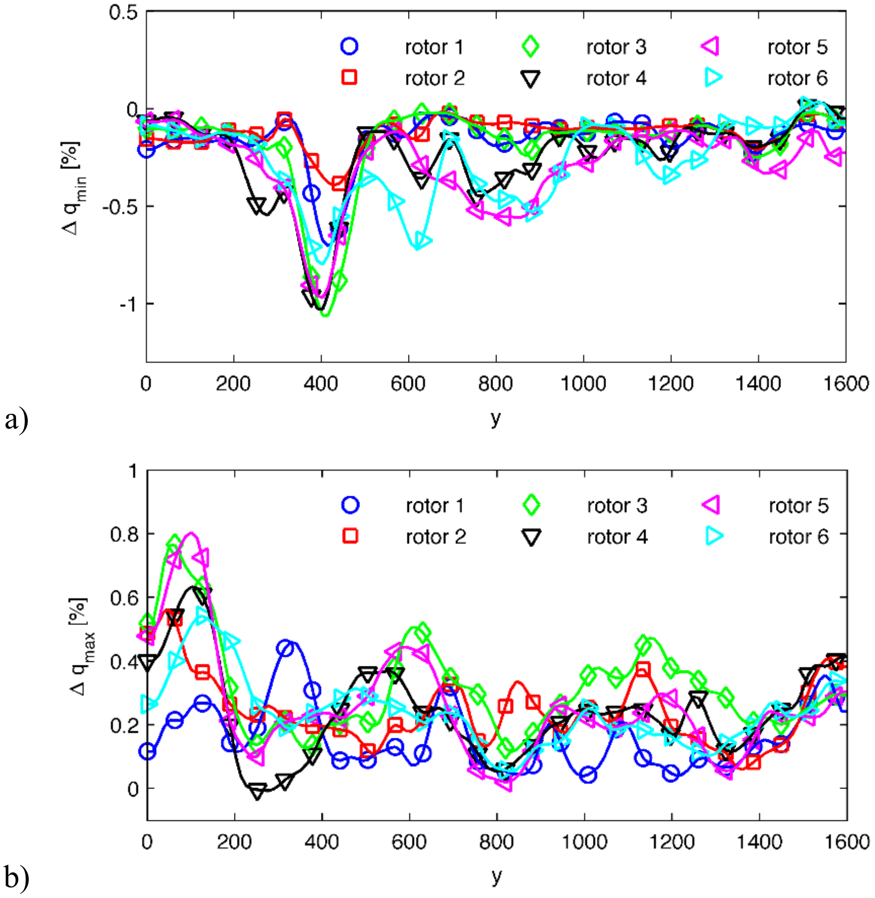

Figure 4.49 Variation of relative humidity with lateral direction for the staggered configuration (profile extracted 2 rotor diameters downstream of the noted rotor): a) decrease (below the hub); b) increase (above the hub).

The lateral distributions for the aligned configuration reinforce the previous observations made for the unstable WTABL. The enhanced background mixing that brings about faster wake recovery manifests in these plots as less wake expansion when compared to the corresponding stable plots of Figure 4.36 through 4.39, which show clear wake expansion. Additionally, the more subdued change in relative humidity associated with the unstable atmospheric regime is apparent in the greater lateral uniformity of the unstable plots compared to the distributions shown for both levels of stable stratification.

Vertical profiles of averaged relative humidity change within the downstream wake are given in Figures 4.50 and 4.51 for the aligned and staggered configuration respectively. All distributions present similarly with a modest humidity gradient below the wind turbine hub height and uniformity both above the hub and, in general, with downstream distance. This is in keeping with the well-mixed nature of the unstable WTABL.

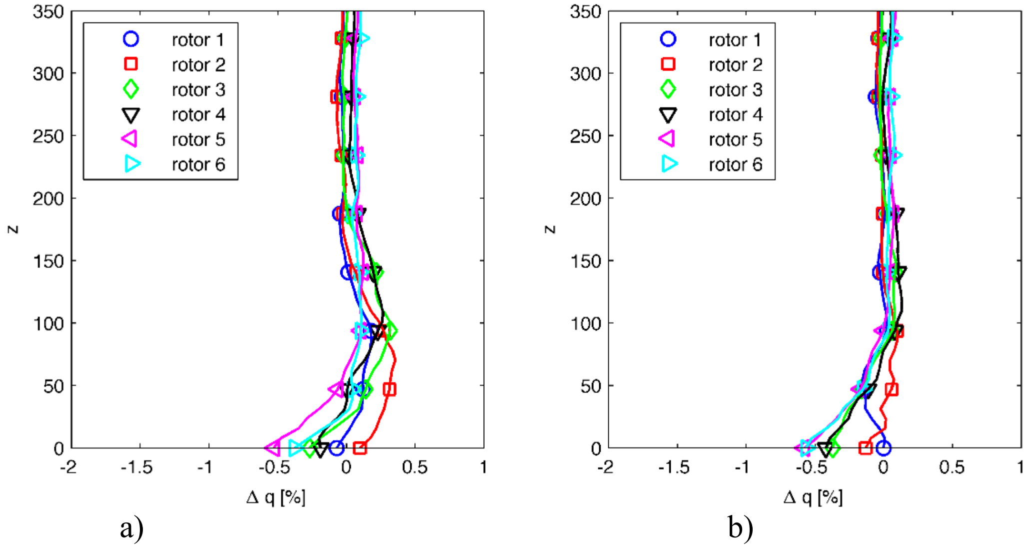

Figure 4.50 Variation of relative humidity with vertical displacement for the aligned array configuration a) left side of the wake; b) right side of the wake.

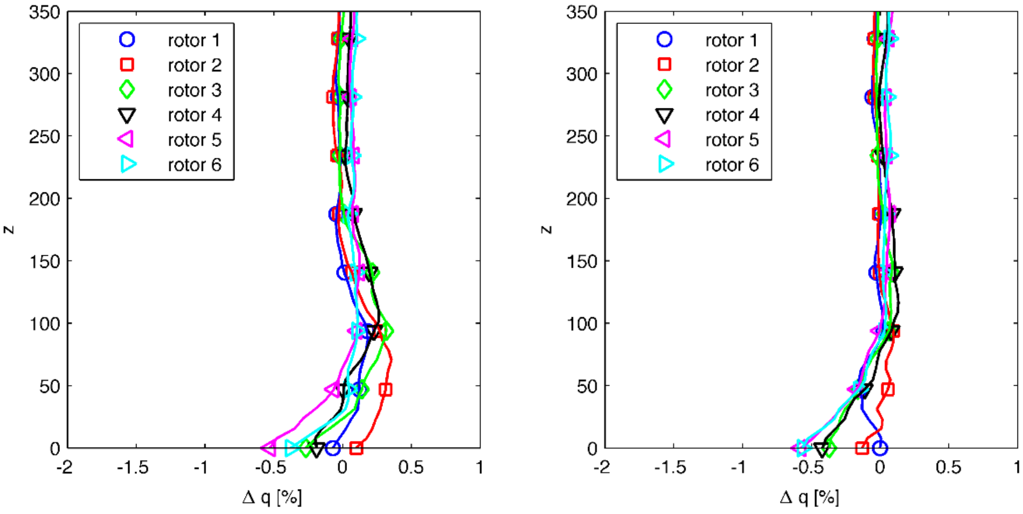

a) b)

Figure 4.51 Variation of relative humidity with vertical displacement for the staggered array configuration: a) left side of the wake; b) right side of the wake.

4.3.2 Neutral Atmospheric Boundary Layer

The effect of compounding wakes in an aligned and staggered 6 x 4 WTABL configuration is also analyzed for a neutral atmospheric stratification. The neutral stability regime is defined by a constant potential temperature lapse rate. In this neutral condition, buoyancy effects are negligible. The instantaneous streamwise velocity, in a horizontal plane at the hub height level, is shown in the contour plots of Figure 4.52. The orientations of the wakes in the neutral regime seem to follow the same trend when compared to the unstable regime, but they feature a certain level of ‘randomness’ versus the orientation of the wakes under stable thermal stratification.

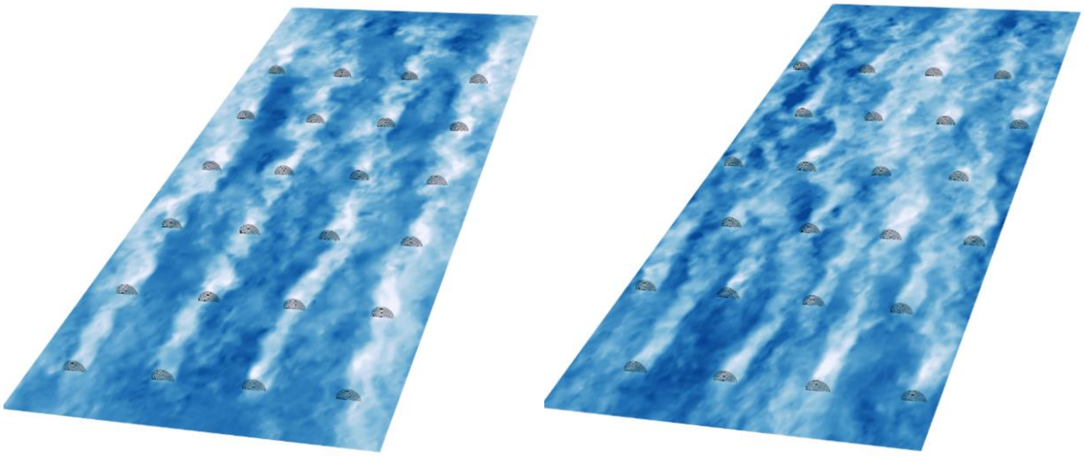

Figure 4.52 Contour plots of instantaneous streamwise velocity in a horizontal plane passing through the hubs of a neutrally stratified WTABL: a) aligned configuration; b) staggered configuration.

Inspection of Figures 4.53 (aligned) and 4.54 (staggered), showing vertically sliced contour plots of humidity change at fixed downstream distances, illustrate how vertically displaced air parcels of a given humidity tend to remain at their newly displaced location. Consequently, the parcels tend to form more diffuse areas of change relative to regions of change in the stable conditions reflected in Figures 4.30a (aligned) and 4.31a (staggered). Therefore, while areas of humidity increase aloft are allowed to maintain their integrity in the absence of strong background mixing, the more diffuse nature of the region of change results in a magnitude of change in-between that found in stable and unstable regimes. Unlike the moister air mixed upward, the drier air mixed downward is constrained by the ground. Consequently, the same level of diffuseness is stymied and the magnitude of humidity decrease is much greater and in line with what might be anticipated during stable conditions, especially for the aligned array. This phenomenon is also captured, and quantified, in Figure 4.55 that provides averaged relative humidity (calculated using Equations 4.4 and 4.5) as a function of downstream position for both array configurations. As mentioned above, the development of the region of decreased relative humidity is constrained by the ground and, although less than, is on par with the magnitude of humidity decrease observed in stable conditions. This is in stark contrast with the unconstrained and, consequently, more diffuse region of humidity increase aloft. This more subdued change is shown in Figure 4.55b and is closer to the magnitude of change associated with an unstable environment.

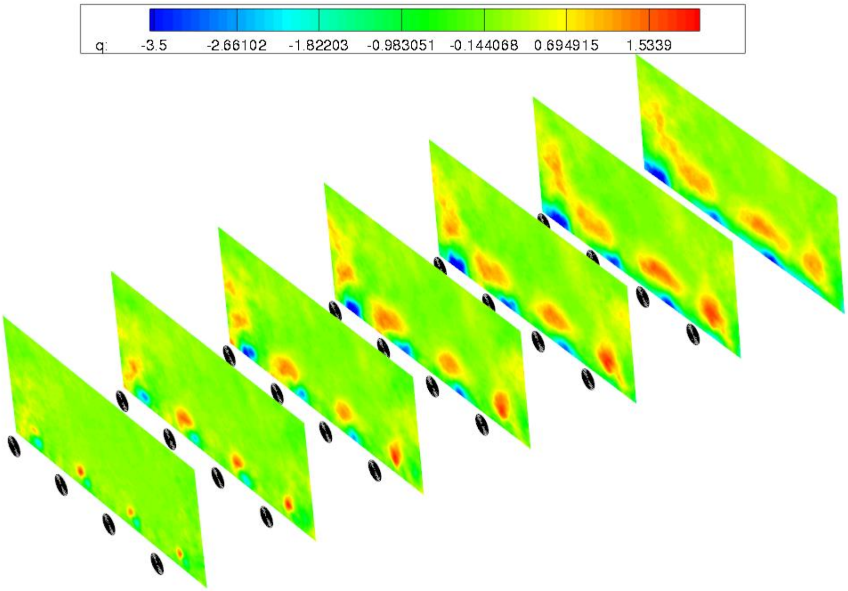

Figure 4.53 Contour plots of time-averaged relative humidity difference in vertical plane slices at fixed downstream distances within an aligned turbine array and neutral environment (the legend shows changes in the relative humidity with respect to the upstream level)

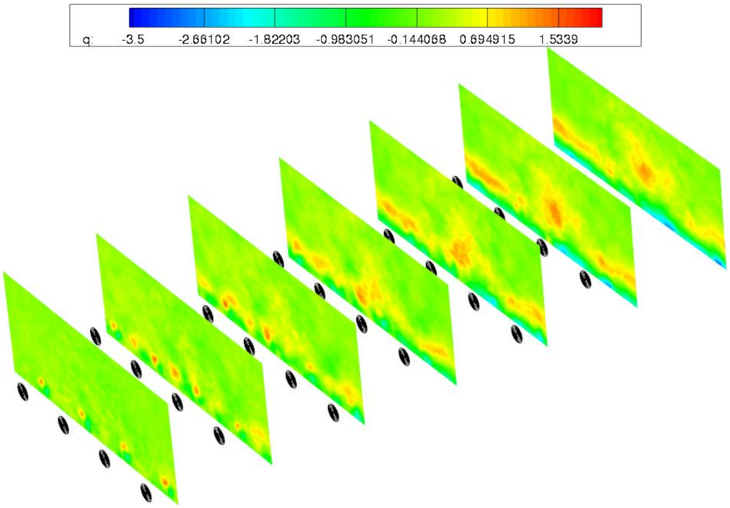

Figure 4.54 Contour plots of time-averaged relative humidity difference in vertical plane slices at fixed downstream distances within a staggered turbine array and neutral environment (the legend shows changes in the relative humidity with respect to the upstream level)

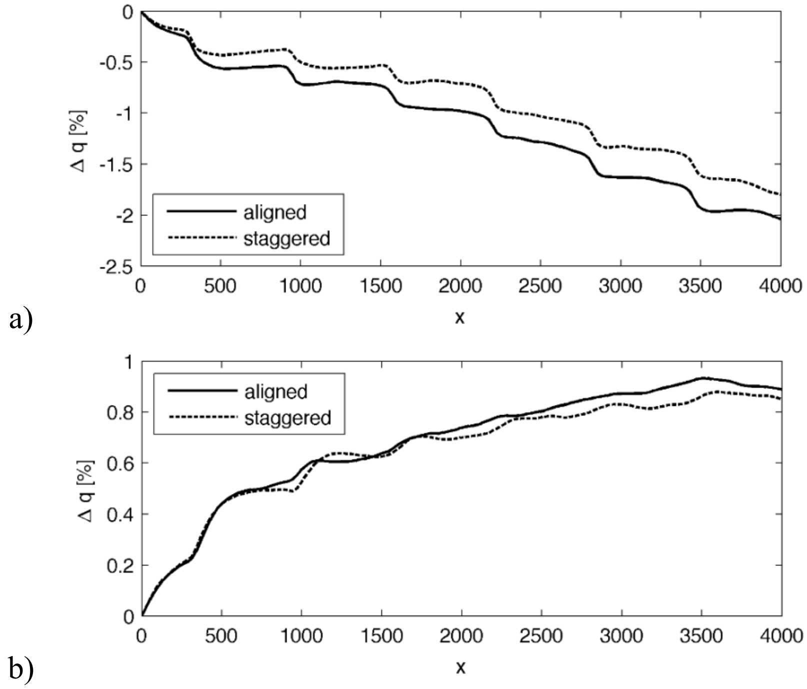

Figure 4.55 Variation of the relative humidity in the streamwise direction for a neutral stratification a) decrease (below the hub); b) increase (above the hub).

Figures 4.56 and 4.57 provide distributions of the maximum and minimum humidity as a function of lateral distance for both array configurations. Although more moderate with respect to magnitude relative to the stable cases, the lateral expansion associated with the accumulated wake is apparent. The absence of strong stable stratification results in the neutral distributions retaining a much greater degree of symmetry than the stable distributions. The influence of the drier air that is brought down on the right-hand side of the rotor disk and the moister air that is delivered upward on the left-hand side is seen in the distributions associated with the aligned configuration. The region of decrease below the turbine hub is observed to build toward the right while the region of increase above builds, albeit more subtle, toward the left. This contrast once again points toward the influence of the ground and the constraint it provides relative to the more diffuse area of change that builds aloft. Comparing the two array configurations, the staggered array configuration provides a much more diffuse area of change absent of channels of humidity change.

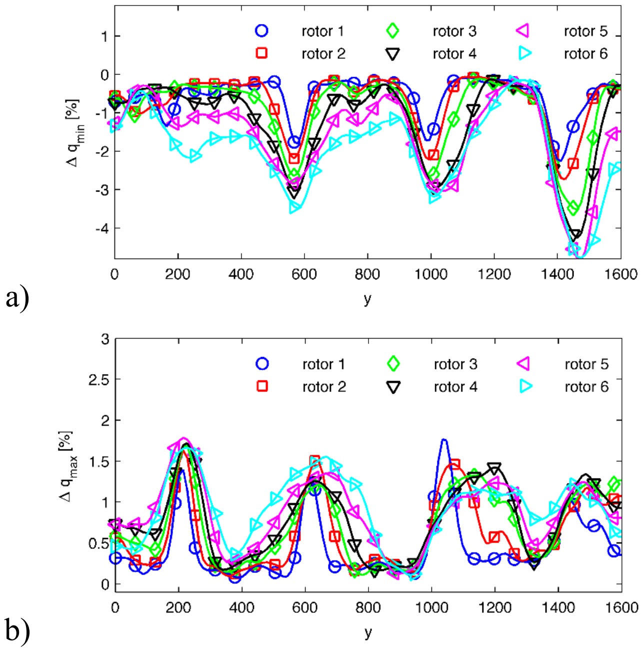

Figure 4.56 Variation of relative humidity with lateral direction for the aligned configuration (profile extracted 2 rotor diameters downstream of the noted rotor): a) decrease (below the hub); b) increase (above the hub).

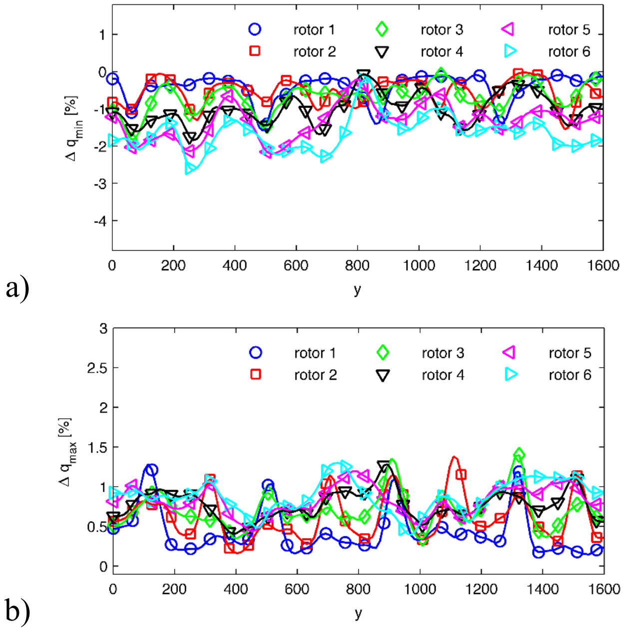

Figure 4.57 Variation of relative humidity with lateral direction for the staggered configuration (profile extracted 2 rotor diameters downstream of the noted rotor): a) decrease (below the hub); b) increase (above the hub).

Vertical profiles of averaged relative humidity at downstream intervals located within the wake are given in Figures 4.58 and 4.59. Inspection of the aligned array vertical distributions reinforce the idea of drier air aloft being delivered downward by the descending blade on the right-hand side of the turbine and building, slightly below the bottom of the turbine disk, in the direction of rotation (left). This results in a greater magnitude of humidity decrease to be realized on the right, compared to the left, side. The magnitude of change at any given level is also observed to increase with the transiting of subsequent downstream turbines. Review of Figure 4.59 shows how the staggered configuration of wind turbines hinders the development of a compounding wake and humidity change with downstream distance.

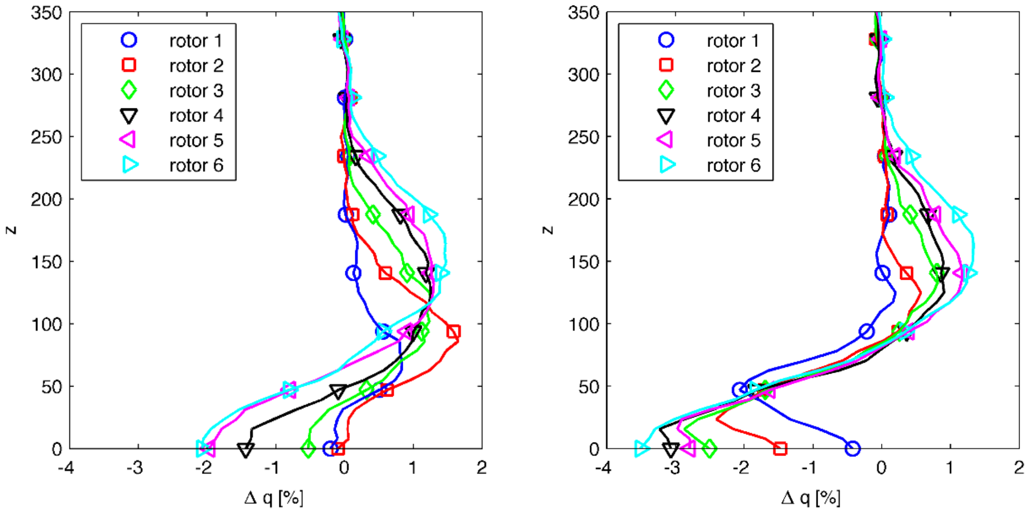

a) b)

Figure 4.58 Variation of relative humidity with vertical displacement for the aligned array configuration a) left side of the wake; b) right side of the wake.

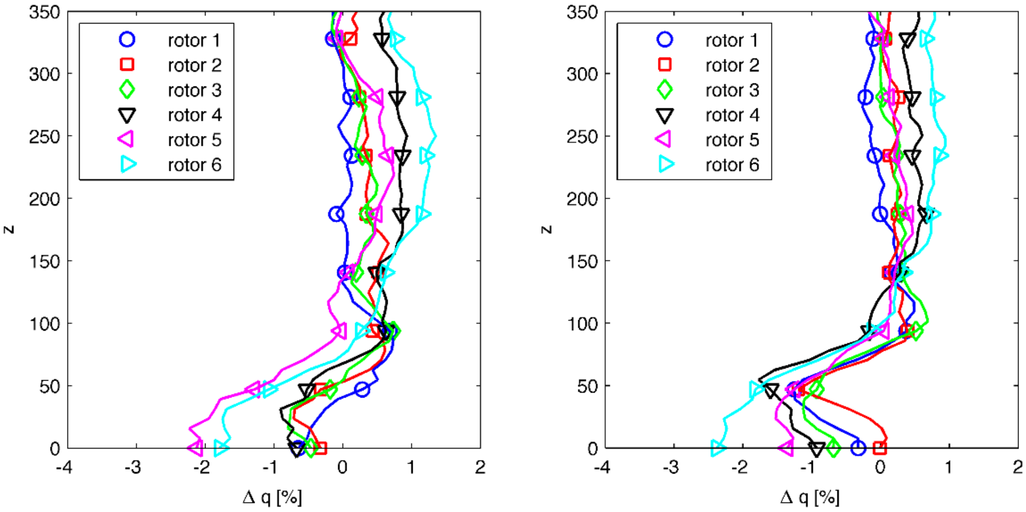

a)

b)

Figure 4.59 Variation of relative humidity with vertical displacement for the staggered array configuration: a) left side of the wake; b) right side of the wake.

CHAPTER V

FINAL CONCLUSIONS

5.1 Contribution

Wind energy is the fastest growing source of electricity generation [3]. While numerical simulation, and limited observations, have established that wind turbines have an impact on near-surface temperature, a thorough investigation of the broader impact that this growing source of electricity has on other aspects of near-surface meteorology has not been undertaken. Changes to near-surface relative humidity are of interest because of its impact on vegetation, the soil it grows in, and animals. Relative humidity affects the rate of evaporation from each of these. Numerical simulations that have investigated the WTABL produce temporal and spatially averaged output, while traditional measurement strategies lack the ability to provide either controlled or continuous measurements with high spatial resolution. The main objective of this research is to investigate the impact that wind turbines have on near-surface relative humidity, which is affected by changes to both temperature and humidity. Utilizing the recent availability of unmanned aerial systems (UAS), high resolution in-situ measurements of relative humidity were made. The use of an UAS demonstrated the successful instrumentation, safe flight and obtainment of high resolution relative humidity values in all three spatial directions. The implementation of the UAS provides proof of concept for a platform that can also be used for the measurement of other atmospheric parameters with high spatial resolution. Observations were qualitatively compared to LES, the most prominent investigation strategy to date. Constrained by current UAS technological limitations and regulatory restrictions, the investigation was extended to a 6 x 4 WTABL via LES but not tackled from the experimental standpoint. This novel multi-prong strategy provides new insight into how near-surface relative humidity is changed in both the near and far wake regions of wind turbines. This work effectively combines experimental observations with numerical simulation in the form of LES, thus allowing for a better understanding of near-surface meteorological changes brought about by wind turbines. The unique contributions and findings of the work can be summarized as follows:

- An unmanned aircraft has been successfully instrumented, safely flown, and measured relative humidity with high spatial resolution
- Relative humidity was observed to change behind a single wind turbine
    - In the presence of a positive humidity lapse rate, relative humidity decreased below the turbine hub height and increased above it
    - The maximum relative humidity decrease occurred between 1 and 2 rotor diameters downstream
    - Larger relative humidity deficits are observed on the right-hand side of the wake
    - The greatest relative humidity decrease is observed slightly below the lower turbine tip height
- Numerical simulation of relative humidity change compared favorably to experimental measurement

- LES of a wind farm revealed that areas of change in relative humidity differentially develop across varying array configurations and atmospheric stratifications
    - The magnitude of relative humidity change became greater with downstream distance
    - Areas of change grow predominately in the direction of turbine rotation and secondarily in all directions due to wake expansion
    - For a given stratification, the greatest decrease in relative humidity is observed in an aligned configuration
    - Regardless of array configuration, the magnitude of relative humidity change increased with stronger thermal stratification
    - The magnitude of relative humidity change varies very little with the wind turbine power coefficient
    - The magnitude of relative humidity change varies appreciably with surface moisture flux but the distinctive spatial characteristics of the humidity change remain consistent
- Relative humidity decreases over 3% were observed behind a single wind turbine and were as great as 2.5% for simulated cases
- Relative humidity decreases slightly over 5% were created by a compounding wake within the WTABL
- Relative humidity changes within a stably stratified WTABL are over an order of magnitude greater than changes within a neutral or unstable WTABL

5.2 Summary

The expense associated with field campaigns and limitations of previous measurement techniques have stymied the number of observational data sets examining changes to near-surface meteorology within WTABLs. This is especially true of data sets with high spatial resolution. Consequently, much of the investigation of the impact that wind turbines have on near-surface meteorology comes in the form of unsubstantiated LES. This research makes use of an instrumented UAS to gather high resolution in-situ field measurements of relative humidity within two state-of-the-art wind farms and compares this data to numerical experiments conducted using LES. Vertical, downstream, and lateral measurements made over the course of several days around a single wind turbine show very good qualitative agreement with all LES results. When similar thermal stratifications are compared, measurements and LES also show good quantitative agreement. Vertical measurement profiles, in the presence of a positive relative humidity lapse rate, show a general decrease in humidity below the turbine hub height and increase above it. The location of maximum decrease occurs slightly below the lower turbine tip height. Downstream observations show a maximum decrease to occur just beyond 1 rotor diameter downstream followed by a slower recovery. The effect of the turbine's rotation and the influence of the underlying surface manifests with an asymmetry in the lateral relative humidity change. Stably stratified LES results show relative humidity decreases as great as 2.5% downstream of the turbine while experimental measurement captured decreases just over 3%.

In order to analyze the accumulated change to relative humidity by compounding wakes, the numerical investigation was extended to a 6 x 4 WTABL. Analogous to experimental observation and numerical results around a single wind turbine, the greatest change in relative humidity is observed during stable conditions. This suggests that the wind turbines' enhancement of vertical mixing plays a larger role when the ABL is more strongly thermally stratified and consequently less well mixed. These results show a somewhat uniform and continuous increase in relative humidity at and above the upper-turbine tip height and a more complex decrease in relative humidity below the turbine hub height. Each of these areas of relative humidity change predominately grows in the direction of turbine rotation while slowly broadening in all directions with wake expansion. In a stable WTABL the decrease in relative humidity is reduced when the array is laid out in a staggered configuration. The magnitude of the decrease in relative humidity in the unstable scenario appears to be independent of the array configuration but is a full order of magnitude smaller than the change observed in the stable environment.

While this research has made use of a novel two-prong complementary strategy, namely experimental measurement with a UAS and numerical investigation via LES, additional opportunities exist for garnering new insight and extending the scope of the work. Additional insight can be gathered through measurements with increased resolution in areas of identified dramatic relative humidity change. The extension of the domain in the downstream direction, with an increase in the number of rows and grid points, also affords the opportunity for additional numerical insight in regard to how the change in relative humidity might attain a fully developed state in a stable WTABL. However, the most exciting possibility for new, complementary insight has recently been made available through new rules issued by the FAA under Part 107 of the Federal Aviation Regulations (FAR). Part 107 operational limitations now allow flight above 400 feet

AGL if within 400 feet of a structure. Therefore, measurements can now be obtained up to 400 feet above the upper turbine tip height of the wind turbine. Such measurements could provide further insight into the region of relative humidity increase, within the vicinity of the upper turbine tip height, along with new insight into how other scalar quantities are impacted by entrainment above the rotor swept area.

REFERENCES

[1] (2008). *20% wind energy by 2030: Increasing wind energy's contribution to U.S. electricity supply*.

[2] (2015). *Wind vision: a new era for wind power in the United States*.

[3] (2016). *International Energy Outlook 2016*.

[4] T. W. House. (2016). *Leaders' Statement on a North American Climate, Clean Energy, and Environment Partnership*. Available: https://www.whitehouse.gov/the-press-office/2016/06/29/leaders-statement-north-american-climate-clean-energy-and-environment

[5] W. E. Forum, "Renewable Infrastructure Investment Handbook: A Guide for Institutional Investors," ed, 2016.

[6] R. B. Stull, *An Introduction to Boundary Layer Meteorology*, 1 ed. (Atmospheric and Oceanographic Sciences Library). Netherlands: Springer, 1988, p. 670.

[7] G. L. Geernaert, *Surface layer* (Encyclopedia of atmospheric sciences). Amsterdam: Elsevier Academic Press, 2003, p. 7.

[8] W. Zhang, C. D. Markfort, and F. Porté-Agel, "Experimental study of the impact of large-scale wind farms on land–atmosphere exchanges," *Environmental Research Letters,* vol. 8, no. 1, 2013.

[9] L. Zhou, Y. Tian, S. B. Roy, C. Thorncroft, L. F. Bosart, and Y. Hu, "Impacts of wind farms on land surface temperature," *Nature Climate Change,* vol. 2, no. 7, pp. 539-543, 2012.

[10] M. Abkar and F. Porté-Agel, "Renewable," *Renewable Energy,* Article vol. 70, pp. 142-152, 10/1/October 2014 2014.

[11] M. Calaf, C. Meneveau, and J. Meyers, "Large eddy simulation study of fully developed wind-turbine array boundary layers," *Physics of Fluids,* Article vol. 22, no. 1, p. 015110, 2010.

[12] W. Yu-Ting and P.-A. Fernando, "Atmospheric Turbulence Effects on Wind-Turbine Wakes: An LES Study," *Energies, Vol 5, Iss 12, Pp 5340-5362 (2012),* article no. 12, p. 5340, 2012.

[13] A. Sescu and C. Meneveau, "Large-Eddy Simulation and Single-Column Modeling of Thermally Stratified Wind Turbine Arrays for Fully Developed, Stationary Atmospheric Conditions," *Journal of Atmospheric & Oceanic Technology,* Article vol. 32, no. 6, pp. 1144-1162, 2015.

[14] S. B. Roy, "Simulating impacts of wind farms on local hydrometeorology," *JOURNAL OF WIND ENGINEERING AND INDUSTRIAL AERODYNAMICS,* vol. 99, no. 4, pp. 491-498, // 2011.

[15] C. M. Smith, R. J. Barthelmie, and S. C. Pryor, "In situ observations of the influence of a large onshore wind farm on near-surface temperature, turbulence intensity and wind speed profiles," *Environmental Research Letters,* vol. 8, no. 3, p. 034006, 07// 2013.

[16] R. A. Harris, Z. Liming, and X. Geng, "Satellite Observations of Wind Farm Impacts on Nocturnal Land Surface Temperature in Iowa," *Remote Sensing,* Article vol. 6, no. 12, pp. 12234-12246, 2014.

[17] M. Calaf, M. B. Parlange, and C. Meneveau, "Large eddy simulation study of scalar transport in fully developed wind-turbine array boundary layers," *Physics of Fluids,* Article vol. 23, no. 12, p. 126603, 2011.

[18] R. Stoll and F. Porté-Agel, "Surface Heterogeneity Effects on Regional-Scale Fluxes in Stable Boundary Layers: Surface Temperature Transitions," *Journal of the Atmospheric Sciences,* Article vol. 66, no. 2, pp. 412-431, 2009.

[19] D. A. Rajewski *et al.*, "Changes in fluxes of heat, H2O, and CO2 caused by a large wind farm," *Agricultural and Forest Meteorology,* Article vol. 194, pp. 175-187, 8/15/15 August 2014 2014.

[20] D. B. Barrie and D. B. Kirk-Davidoff, "Weather response to a large wind turbine array," *Atmospheric Chemistry & Physics,* Article vol. 10, no. 2, pp. 769-775, 2010.

[21] C. Wang and R. G. Prinn, "Potential climatic impacts and reliability of very large-scale wind farms," *Atmospheric Chemistry & Physics,* Article vol. 10, no. 4, pp. 2053-2061, 2010.

[22] D. B. Kirk-Davidoff and D. W. Keith, "On the Climate Impact of Surface Roughness Anomalies," *Journal of the Atmospheric Sciences,* Article vol. 65, no. 7, pp. 2215-2234, 2008.

[23] A. C. Fitch, "Climate Impacts of Large-Scale Wind Farms as Parameterized in a Global Climate Model," *Journal of Climate,* Article vol. 28, no. 15, pp. 6160-6180, 2015.

[24] S. B. Roy, S. W. Pacala, and R. L. Walko, "Can large wind farms affect local meteorology? (DOI 10.1029/2004JD004763)," (in English), *JOURNAL OF GEOPHYSICAL RESEARCH -ALL SERIES-,* vol. 109, no. 19, p. D19101, // 2004.

[25] S. B. Pope, *Turbulent flows*. U.K.: Cambridge University Press, 2000.

[26] H. Lu and F. Porté-Agel, "Large-eddy simulation of a very large wind farm in a stable atmospheric boundary layer," *Physics of Fluids,* Article vol. 23, no. 6, p. 065101, 2011.

[27] W. Yu-Ting and F. Porté-Agel, "Atmospheric Turbulence Effects on Wind-Turbine Wakes: An LES Study," *Energies (19961073),* Article vol. 5, no. 12, pp. 5340-5362, 2012.

[28] M. Abkar and F. Porté-Agel, "The Effect of Free-Atmosphere Stratification on Boundary-Layer Flow and Power Output from Very Large Wind Farms," *Energies (19961073),* Article vol. 6, no. 5, pp. 2338-2361, 2013.

[29] J. D. Mirocha *et al.*, "Investigating wind turbine impacts on near-wake flow using profiling lidar data and large-eddy simulations with an actuator disk model," *Journal of Renewable & Sustainable Energy,* Article vol. 7, no. 4, pp. 1-21, 2015.

[30] D. Allaerts and J. Meyers, "Large eddy simulation of a large wind-turbine array in a conventionally neutral atmospheric boundary layer," *Physics of Fluids,* Article vol. 27, no. 6, pp. 1-22, 2015.

[31] M. Abkar and F. Porté-Agel, "Influence of atmospheric stability on wind-turbine wakes: A large-eddy simulation study," *Physics of Fluids,* Article vol. 27, no. 3, pp. 1-19, 2015.

[32] C. VerHulst and C. Meneveau, "Large eddy simulation study of the kinetic energy entrainment by energetic turbulent flow structures in large wind farms," *Physics of Fluids,* Article vol. 26, no. 2, pp. 1-20, 2014.

[33] C. VerHulst and C. Meneveau, "Altering Kinetic Energy Entrainment in Large Eddy Simulations of Large Wind Farms Using Unconventional Wind Turbine Actuator Forcing," *Energies (19961073),* Article vol. 8, no. 1, pp. 370-386, 2015.

[34] S. B. Roy, J. J. Traiteur, and S. H. Schneider. (2010) Impacts of wind farms on surface air temperatures. [research article]. 17899.

[35] M. J. Lauridsen, "Impact of Wind Turbine Wakes on the Atmospheric Surface Layer: Decrease in Stability and Dew Duration," E. S. Takle and D. A. Rajewski, Eds., ed. Ames, Iowa: Department of Geological and Atmospheric Sciences, Iowa State University, 2012.

[36] D. A. Rajewski *et al.*, "CROP WIND ENERGY EXPERIMENT (CWEX)," *Bulletin of the American Meteorological Society,* Article vol. 94, no. 5, pp. 655-672, 2013.

[37] M. Henschen *et al.*, "Do Wind Turbines Affect Weather Conditions?: A Case Study in Indiana," ed: Purdue University, 2011.

[38] J. M. Walsh-Thomas, G. Cervone, P. Agouris, and G. Manca, "Further evidence of impacts of large-scale wind farms on land surface temperature," *Renewable and Sustainable Energy Reviews,* Review Article vol. 16, pp. 6432-6437, 10/1/October 2012 2012.

[39] L. Zhou, Y. Tian, S. Baidya Roy, Y. Dai, and H. Chen, "Diurnal and seasonal variations of wind farm impacts on land surface temperature over western Texas," *Climate Dynamics,* Article vol. 41, no. 2, pp. 307-326, 2013.

[40] L. M. Slawsky, Z. Liming, S. Baidya Roy, X. Geng, M. Vuille, and R. A. Harris, "Observed Thermal Impacts of Wind Farms Over Northern Illinois," *Sensors (14248220),* Article vol. 15, no. 7, pp. 14981-15005, 2015.

[41] T. G. Konrad, M. L. Hill, J. R. Rowland, and J. H. Meyer, "A Small, Radio-Controlled Aircraft as a Platform for Meteorological Sensors," *Johns Hopkins APL Tech Digest,* vol. 10, pp. 11-19, 1970.

[42] R. Austin, J. A. Schetz, Ed. *Unmanned Aircraft Systems: UAVS Design, Development and Deployment*. Reston, Virginia: American Institute of Aeronautics and Astronautics, Inc., 2010.

[43] J. Selker, S. Tyler, C. Higgins, and M. G. Wing, "Drone Squadron To Take Earth Monitoring To New Heights," *Earth & Space Science News,* vol. 96, no. 19, p. 32, 2015.

[44] J. Jacob, "Unmanned Aircraft in Meteorology and Atmospheric Physics," in *AUVSI Xponential*, New Orleans, LA, 2016.

[45] J. Elston, B. Argrow, M. Stachura, D. Weibel, D. Lawrence, and D. Pope, "Overview of Small Fixed-Wing Unmanned Aircraft for Meteorological Sampling," *Journal of Atmospheric & Oceanic Technology,* Article vol. 32, no. 1, pp. 97-115, 2015.

[46] J. Egger *et al.*, "Diurnal Winds in the Himalayan Kali Gandaki Valley. Part III: Remotely Piloted Aircraft Soundings," *Monthly Weather Review,* Article vol. 130, no. 8, p. 2042, 2002.

[47] T. Spiess, J. Bange, M. Buschmann, and P. Vörsmann, "First application of the meteorological Mini-UAV 'M2AV'," *Meteorologische Zeitschrift,* vol. 16, no. 2, p. 159, 04/01/Number 2/April 2007 2007.

[48] "The Small Unmanned Meteorological Observer SUMO: A new tool for atmospheric boundary layer research," *Anthropologischer Anzeiger,* vol. 69, no. 3, p. 141, 07//7/1/2012 2012.

[49] J. Reuder, P. Brisset, M. Jonassen, M. Müller, and S. Mayer, "The Small Unmanned Meteorological Observer SUMO: A new tool for atmospheric boundary layer research," *Meteorologische Zeitschrift,* vol. 18, no. 2, p. 141, 04/01/Number 2/April 2009 2009.

[50] N. Dias, J. Goncalves, and A. Luciano, "Probing the Atmospheric Boundary-layer with a Cost-effective Mini-UAV," vol. 30, ed. Asia: AsiaFlux Newsletter, 2009.

[51] A. Kroonenberg, S. Martin, F. Beyrich, and J. Bange, "Spatially-Averaged Temperature Structure Parameter Over a Heterogeneous Surface Measured by an Unmanned Aerial Vehicle," *Boundary-Layer Meteorology,* Article vol. 142, no. 1, pp. 55-77, 2012.

[52] T. Bonin, P. Chilson, B. Zielke, and E. Fedorovich, "Observations of the Early Evening Boundary-Layer Transition Using a Small Unmanned Aerial System," *Boundary-Layer Meteorology,* Article vol. 146, no. 1, pp. 119-132, 2013.

[53] D. A. Lawrence and B. B. Balsley, "High-Resolution Atmospheric Sensing of Multiple Atmospheric Variables Using the DataHawk Small Airborne Measurement System," *Journal of Atmospheric & Oceanic Technology,* Article vol. 30, no. 10, pp. 2352-2366, 2013.

[54] C. Wainwright, T. Bonin, P. Chilson, J. Gibbs, E. Fedorovich, and R. Palmer, "Methods for Evaluating the Temperature Structure-Function Parameter Using Unmanned Aerial Systems and Large-Eddy Simulation," *Boundary-Layer Meteorology,* Article vol. 155, no. 2, pp. 189-208, 2015.

[55] B. R. Elbing and R. J. Gaeta, "Integration of Infrasonic Sensing with UAS," presented at the AIAA atmospheric and space environments, Washington, D.C, 2016.

[56] J. J. Cassano, "Observations of atmospheric boundary layer temperature profiles with a small unmanned aerial vehicle," *Antarctic Science,* Article vol. 26, no. 2, pp. 205-213, 2014.

[57] B. M. Witte, C. Schlagenhauf, J. Mullen, J. P. Helvey, M. A. Thamann, and S. Bailey, "Fundamental Turbulence Measurement with Unmanned Aerial Vehicles," presented at the AIAA atmospheric and space environments, Washington, D.C, 2016.

[58] B. D. Reineman, L. Lenain, N. M. Statom, and W. K. Melville, "Development and Testing of Instrumentation for UAV-Based Flux Measurements within Terrestrial and Marine Atmospheric Boundary Layers," *Journal of Atmospheric & Oceanic Technology,* Article vol. 30, no. 7, pp. 1295-1319, 2013.

[59] B. Balsley, D. Lawrence, R. Woodman, and D. Fritts, "Fine-Scale Characteristics of Temperature, Wind, and Turbulence in the Lower Atmosphere (0-1,300m) Over the South Peruvian Coast," *Boundary-Layer Meteorology,* vol. 147, pp. 165-178, 2013.

[60] M. O. Jonassen, H. ÓLafsson, H. ÁGÚStsson, Ó. RÖGnvaldsson, and J. Reuder, "Improving High Resolution Numerical Weather Simulations by Assimilating Data from an Unmanned Aerial System," *Monthly Weather Review,* Article vol. 140, no. 11, pp. 3734-3756, 2012.

[61] J. Dyer, L. Wasson, and R. Moorhead, "Boundary Layer Measurements Over Land Use/Cover Discontinuities Using a Small UAS (Invited)," presented at the AIAA atmospheric and space environments, Washington, D.C, 2016.

[62] S. Mayer, A. Sandvik, M. Jonassen, and J. Reuder, "Atmospheric profiling with the UAS SUMO: a new perspective for the evaluation of fine-scale atmospheric models," *Meteorology & Atmospheric Physics,* Article vol. 116, no. 1/2, pp. 15-26, 2012.

[63] E. W. Frew *et al.*, "Toward an Autonomous Airborne Scientist for Studying Severe Local Storms," presented at the AIAA atmospheric and space environments, Washington, D.C, 2016.

[64] J. Reuder, M. Jonassen, and H. Ólafsson, "The Small Unmanned Meteorological Observer SUMO: Recent developments and applications of a micro-UAS for atmospheric boundary layer research," *Acta Geophysica,* vol. 60, no. 5, p. 1454, 10// 2012.

[65] S. Mayer, M. Jonassen, A. Sandvik, and J. Reuder, "Profiling the Arctic Stable Boundary Layer in Advent Valley, Svalbard: Measurements and Simulations," *Boundary-Layer Meteorology,* Article vol. 143, no. 3, pp. 507-526, 2012.

[66] "Application of remotely piloted aircraft systems in observing the atmospheric boundary layer over Antarctic sea ice in winter," ed: WILEY-BLACKWELL PUBLISHING, 2015., 2015.

[67] J. Reuder, P. Brisset, M. Jonassen, M. Müller, and S. Mayer, "SUMO: A small unmanned meteorological observer for atmospheric boundary layer research," *IOP Conference Series: Earth & Environmental Science,* vol. 1, no. 1, p. 1, 01// 2008.

[68] S. Martin, J. Bange, and F. Beyrich, "Meteorological profiling of the lower troposphere using the research UAV "M²AV Carolo"," *Atmospheric Measurement Techniques,* Article vol. 4, no. 4, pp. 705-716, 2011.

[69] D. E. Cook, P. A. Strong, S. A. Garrett, and R. E. Marshall, "A small unmanned aerial system (UAS) for coastal atmospheric research: preliminary results from New Zealand," *Journal of the Royal Society of New Zealand,* Article vol. 43, no. 2, pp. 108-115, 2013.

[70] N. Dias, J. Gonçalves, L. Freire, T. Hasegawa, and A. Malheiros, "Obtaining Potential Virtual Temperature Profiles, Entrainment Fluxes, and Spectra from Mini Unmanned Aerial Vehicle Data," *Boundary-Layer Meteorology,* Article vol. 145, no. 1, pp. 93-111, 2012.

[71] G. Giebel *et al.*, *Autonomous Aerial Sensors for Wind Power Meteorology - A Pre-Project*. Denmark, Europe: Danmarks Tekniske Universitet, Risø Nationallaboratoriet for Bæredygtig Energi, 2012.

[72] "Autonomous aerial sensors for wind power meteorology," ed: EWEA, 2011., 2011.

[73] M. Mansour, G. Kocer, C. Lenherr, N. Chokani, and R. S. Abhari, "Seven-sensor fast-response probe for full-scale wind turbine flowfield measurements," *Journal of Engineering for Gas Turbines and Power,* no. 8, p. 81601, 2011.

[74] G. Kocer, M. Mansour, N. Chokani, R. S. Abhari, and M. Müller, "Full-Scale Wind Turbine Near-Wake Measurements Using an Instrumented Uninhabited Aerial Vehicle," *Journal of Solar Energy Engineering,* Article vol. 133, no. 4, pp. 41011.1-41011.8, 2011.

[75] J. Reuder and M. O. Jonassen, "First Results of Turbulence Measurements in a Wind Park with the Small Unmanned Meteorological Observer SUMO," *Energy Procedia,* Review Article vol. 24, pp. 176-185, 1/1/2012 2012.

[76] L. Båserud, M. Flügge, A. Bhandari, and J. Reuder, "Characterization of the SUMO Turbulence Measurement System for Wind Turbine Wake Assessment," *Energy Procedia,* Article vol. 53, pp. 173-183, 1/1/2014 2014.

[77] G. E. Company. (2015). *Best-In-Class Capacity Factor GE's 1.7-100*. Available: https://renewables.gepower.com/content/dam/gepower-renewables/global/en_US/documents/product-brochures/GEA18628H%20Wind_1.7-100_Brochure_R1.pdf

[78] Gamesa. (2015). *Gamesa 2.0-2.5 MW Technological Evolution*. Available: http://www.gamesacorp.com/recursos/doc/productos-servicios/aerogeneradores/catalogo-g9x-20-mw-eng.pdf

[79] Rotronic. (2017). *The Capacitive Humidity Sensor*. Available: https://www.rotronic.com/en-us/humidity_measurement-feuchtemessung-mesure_de_l_humidite/capacitive-sensors-technical-notes-mr.

[80] U. S. Institute, "Small UAS Safety," Orlando, FL: Unmanned Safety Institute, 2015.

[81] D. C. Wilcox, *Turbulence modeling for CFD.* Canada: DCW Industries, La Canada, CA., 1998.

[82] A. Kolmogorov, N., "Dissipation of energy in locally isotropic turbulence," *Dokl. Akad. Nauk SSSR* vol. 32, no. 1, pp. 16-18, 1941.

[83] J. Blazek, *Computational Fluid Dynamics: Principles and Applications*, second ed. London: Elsevier, 2005, p. 470.

[84] D. K. Lilly, "The representation of small-scale turbulence in numerical simulation experiments, in Proceedings of the IBM Scientific Computing Symposium on Environmental Sciences", Yorktown Heights, NY, USA, 1967, p. 167.

[85] F. Porte-Agel, Meneveau, C. and Parlange, M.B., "A scale-dependent dynamic model for large-eddy simulations: application to a neutral atmospheric boundary layer," *J. Fluid Mech.,* no. 415, pp. 261-284, 2000.

[86] E. Bou-Zeid, C. Meneveau, and M. B. Parlange, "A scale-dependent Lagrangian dynamic model for large eddy simulation of complex turbulent flows," ed. Switzerland, Europe, 2005.

[87] R. J. A. M. Stevens, J. Graham, and C. Meneveau, "A concurrent precursor inflow method for Large Eddy Simulations and applications to finite length wind farms," *Renewable Energy,* Author abstract p. 46, 2014.

[88] A. Sescu and C. Meneveau, "A control algorithm for statistically stationary large-eddy simulations of thermally stratified boundary layers," *Quarterly Journal of the Royal Meteorological Society,* Report no. 683, p. 2017, 2014.

[89] A. M. Obukhov, "Turbulence in a thermally inhomogeneous atmosphere," *Bound.-Layer Meteor.,* no. 2, pp. 7-29, 1946.

[90] A. S. Monin, "Turbulence in the atmospheric surface layer," *Coll. Sci. Inf. Hydrometeor. Ser. USSR.,* no. 1, pp. 13-27, 1950.

[91] A. S. Monin and A. M. Obukhov, "Dimensionless characteristics of turbulence in the atmospheric surface layer," *Dok. AN SSSR,* no. 93, pp. 223-226, 1953.

[92] A. S. O. Monin, A. M., "Basic laws of turbulent mixing in the ground layer of the atmosphere," *Tr. Geofiz. Inst. Akad. Nauk SSSR,* no. 151, pp. 163-187, 1954.

[93] J. A. Businger, J. C. Wyngaard, Izumi, and E. F. Bradley, "Flux-Profile Relationships in the Atmospheric Surface Layer," *Journal of the Atmospheric Sciences,* vol. 28, pp. 181-189, 1971.

[94] S. Orszag, "Numerical simulation of incompressible flows within simple boundaries: accuracy," *Journal of Fluid Mechanics,* vol. 49, no. 1, pp. 75- 112, 1971.

[95] R. Miller, *Introduction to Differential Equations*, Second ed. Englewood Cliffs, NJ: Prentice-Hall, Inc., 1991, p. 618.

[96] Y.-T. Wu and F. Porté-Agel, "Large-Eddy Simulation of Wind-Turbine Wakes: Evaluation of Turbine Parametrisations," *Boundary-Layer Meteorology,* vol. 138, no. 3, pp. 345-366, 2011.

[97] E. Kulunk, "Aerodynamics of Wind Power," in *Fundamental and Advanced Topics in Wind Power*, R. Carriveau, Ed.: InTech, 2011.

[98] J. Meyers *et al.*, "Large Eddy Simulations of large wind-turbine arrays in the atmospheric boundary layer," presented at the 48th AIAA Aerospace Sciences Meeting Including the New Horizons Forum and Aerospace Exposition, Orlando, Florida, 2010.

[99] J. Meyers and C. Meneveau, "Flow visualization using momentum and energy transport tubes and applications to turbulent flow in wind farms," *Journal of Fluid Mechanics,* vol. 715, pp. 335-358, 2013.

[100] J. N. Sorensen and W. Z. Shen, "Numerical modeling of wind turbine wakes," *J. Fluids Eng.,* vol. 124, pp. 393-399, 2002.

[101] R. Dovich, *Quality Engineering Statistics*. Milwaukee, WI: ASQ Quality Press, 1992.

[102] R. B. Stull, *Meteorology for Scientists and Engineers*, 2 ed. Belmont, CA: Gary Garlson, 2000, p. 502.

[103] J. F. Manwell, J. G. McGowan, and A. L. Rogers, *Wind Energy Explained*, 2 ed. West Sussex, United Kingdom: Wiley, 2009.

[104] M. M. Cairns, Ed. *Glossary of Meteorology*, 2 ed. American Meteorological Society, 2000.

APPENDIX A

FAA COMPLIANCE

The research nature of the field campaign categorizes the operation as a commercial endeavor. Consequently, the FAA was petitioned and it was determined that the aircraft met the conditions of Section 333 of the FAA Modernization and Reform Act of 2012 that allows relief from Title 14 of the Code of Federal Regulations (CFR) part 21, Certification Procedures for Products and Parts, Subpart H—Airworthiness Certificates, and associated noise certification and testing requirements of part 36. Of direct operational significance to the field campaign were the following conditions and limitations associated with the Section 333 exemption:

- Operations are limited to the DJI Inspire 1.
- The unmanned aircraft (UA) must be operated at an altitude of no more than 400 AGL.
- A visual observer (VO) must be used for all operations.
- The UA must be operated within visual line of sight (VLOS) of the pilot-in-command (PIC) and VO at all times.
- The VO and PIC must be able to communicate verbally at all times.
- Following any maintenance or alteration that affects the UAS operation or flight characteristics, a functional test flight must be conducted.
- The operator is responsible for maintaining and inspecting the UAS, along with complying with all manufacturer safety bulletins, to ensure that the UAS is in a condition for safe operation.
- Prior to each flight, the PIC must conduct a pre-flight inspection and determine the UAS is in a condition for safe flight.

- All UAS operations may not be conducted during night, as defined in 14 CFR § 1.1.
- All operations must be conducted under visual meteorological conditions (VMC).
- The PIC must be a FAA certificated pilot.
- The UA may not operate within 5 nautical miles of an airport reference point.
- The UA must maintain basic visual flight reference (VFR) visibility and cloud clearance requirements.
- The UA must maintain an adequate power level for the UA to complete the intended operation with at least 5 minutes of power remaining.
- The UA must remain clear and give way to all manned aviation operations and activities at all times.
- All operations conducted over private or controlled-access property must receive permission from the property owner.

A copy of the Section 333 exemption is available in Appendix B.

A Section 333 exemption is automatically issued with a "blanket" nationwide Certificate of Authorization (COA). At the time of original issuance of the Section 333 exemption the blanket COA, accompanying the exemption, put forth a few restrictions. The UAS was required to fly below 200 feet with additional limitations imposed around airports, restricted airspace, and other densely populated areas. With the desire to operate up to 400 feet AGL, a separate COA was pursued, allowing flight up to 400 feet AGL. However, on March 29, 2016, the FAA announced a decision to raise the operating altitude associated with the blanket COA to 400 feet AGL. As a result, further pursuit of an additional COA was suspended. The existence of any NOTAMs, that further curtailed operations, was investigated and none pertaining to the measurement region were found.

Shortly before the commencement of flight testing of the UAS, the FAA opened up the web-based registration system, designed exclusively for sUAS, to commercial operators. This negated the previous need to register the sUAS with an N number under the FAA's legacy paper-based system that was used for both manned and unmanned aircraft. The resulting registration certificate is found in Appendix C.

Per the requirement of the FAA, a distant (D) NOTAM was filed with flight service prior to 24 hours before the commencement of the measurement campaign and was maintained for the duration of the field campaign. A latitude and longitude were provided, along with a radius of operation.

APPENDIX B

FAA SECTION 333 EXEMPTION

B.1 FAA Section 333 Exemption

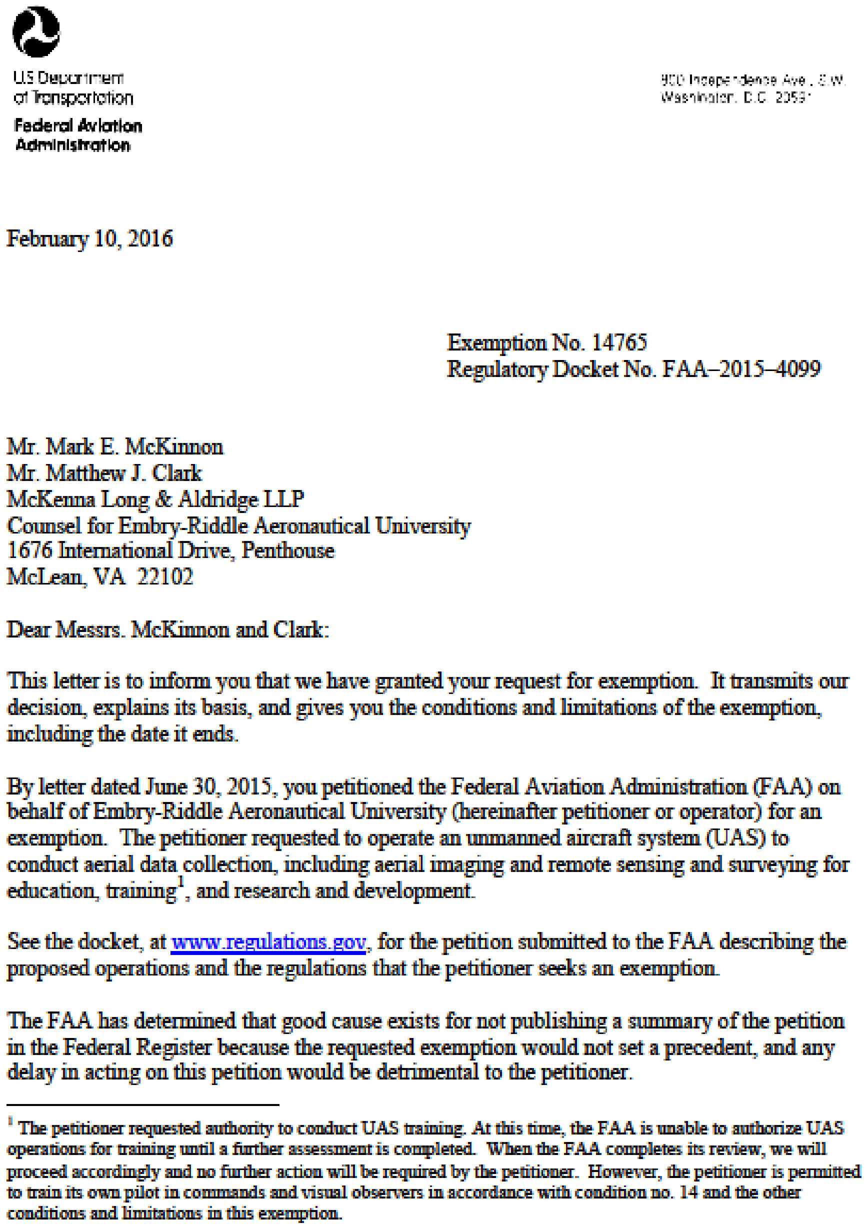

U.S. Department
of Transportation
**Federal Aviation
Administration**

800 Independence Ave., S.W.
Washington, D.C. 20591

February 10, 2016

Exemption No. 14765
Regulatory Docket No. FAA–2015–4099

Mr. Mark E. McKinnon
Mr. Matthew J. Clark
McKenna Long & Aldridge LLP
Counsel for Embry-Riddle Aeronautical University
1676 International Drive, Penthouse
McLean, VA 22102

Dear Messrs. McKinnon and Clark:

This letter is to inform you that we have granted your request for exemption. It transmits our decision, explains its basis, and gives you the conditions and limitations of the exemption, including the date it ends.

By letter dated June 30, 2015, you petitioned the Federal Aviation Administration (FAA) on behalf of Embry-Riddle Aeronautical University (hereinafter petitioner or operator) for an exemption. The petitioner requested to operate an unmanned aircraft system (UAS) to conduct aerial data collection, including aerial imaging and remote sensing and surveying for education, training[1], and research and development.

See the docket, at www.regulations.gov, for the petition submitted to the FAA describing the proposed operations and the regulations that the petitioner seeks an exemption.

The FAA has determined that good cause exists for not publishing a summary of the petition in the Federal Register because the requested exemption would not set a precedent, and any delay in acting on this petition would be detrimental to the petitioner.

---

[1] The petitioner requested authority to conduct UAS training. At this time, the FAA is unable to authorize UAS operations for training until a further assessment is completed. When the FAA completes its review, we will proceed accordingly and no further action will be required by the petitioner. However, the petitioner is permitted to train its own pilot in commands and visual observers in accordance with condition no. 14 and the other conditions and limitations in this exemption.

Airworthiness Certification

The UAS proposed by the petitioner are the SenseFly EBee, DJI Inspire 1, Draganflyer X4-ES, Latitude HQ-40A, Mikrokopter Rotorcraft, Embry-Riddle Aeronautical University ERFC UAS.

In accordance with the statutory criteria provided in Section 333 of Public Law 112–95 in reference to 49 U.S.C. § 44704, and in consideration of the size, weight, speed, and limited operating area associated with the aircraft and its operation, the Secretary of Transportation has determined that this aircraft meets the conditions of Section 333. Therefore, the FAA finds that relief from 14 CFR part 21, *Certification procedures for products and parts, Subpart H—Airworthiness Certificates*, and any associated noise certification and testing requirements of part 36, is not necessary.

The Basis for Our Decision

You have requested to use a UAS for aerial data collection[2]. The FAA has issued grants of exemption in circumstances similar in all material respects to those presented in your petition. In Grants of Exemption Nos. 11062 to Astraeus Aerial (*see* Docket No. FAA–2014–0352), 11109 to Clayco, Inc. (*see* Docket No. FAA–2014–0507), 11112 to VDOS Global, LLC (*see* Docket No. FAA–2014–0382), 11213 to Aeryon Labs, Inc. (*see* Docket No. FAA–2014–0642), and 12645 to Allied Drones (*see* Docket No. FAA-2014-0804), the FAA found that the enhanced safety achieved using an unmanned aircraft (UA) with the specifications described by the petitioner and carrying no passengers or crew, rather than a manned aircraft of significantly greater proportions, carrying crew in addition to flammable fuel, gives the FAA good cause to find that the UAS operation enabled by this exemption is in the public interest.

Having reviewed your reasons for requesting an exemption, I find that—

- They are similar in all material respects to relief previously requested in Grant of Exemption Nos. 11062, 11109, 11112, 11213, and 12645;
- The reasons stated by the FAA for granting Exemption Nos. 11062, 11109, 11112, 11213, and 12645 also apply to the situation you present; and
- A grant of exemption is in the public interest.

---

[2] Aerial data collection includes any remote sensing and measuring by an instrument(s) aboard the UA. Examples include imagery (photography, video, infrared, etc.), electronic measurement (precision surveying, RF analysis, etc.), chemical measurement (particulate measurement, etc.), or any other gathering of data by instruments aboard the UA.

Our Decision

In consideration of the foregoing, I find that a grant of exemption is in the public interest. Therefore, pursuant to the authority contained in 49 U.S.C. 106(f), 40113, and 44701, delegated to me by the Administrator, Embry-Riddle Aeronautical University is granted an exemption from 14 CFR §§ 61.23(a) and (c), 61.101(e)(4) and (5), 61.113(a), 61.315(a), 91.7(a), 91.119(c), 91.121, 91.151(a)(1), 91.405(a), 91.407(a)(1), 91.409(a)(1) and (2), and 91.417(a) and (b), to the extent necessary to allow the petitioner to operate a UAS to perform aerial data collection. This exemption is subject to the conditions and limitations listed below.

Conditions and Limitations

In this grant of exemption, Embry-Riddle Aeronautical University is hereafter referred to as the operator.

Failure to comply with any of the conditions and limitations of this grant of exemption will be grounds for the immediate suspension or rescission of this exemption.

1. Operations authorized by this grant of exemption are limited to the SenseFly EBee, DJI Inspire 1, Draganflyer X4-ES, Latitude HQ-40A, Mikrokopter Rotorcraft, Embry-Riddle Aeronautical University ERFC UAS when weighing less than 55 pounds including payload. Proposed operations of any other aircraft will require a new petition or a petition to amend this exemption.

2. Operations for the purpose of closed-set motion picture and television filming are not permitted.

3. The UA may not be operated at a speed exceeding 87 knots (100 miles per hour). The exemption holder may use either groundspeed or calibrated airspeed to determine compliance with the 87 knot speed restriction. In no case will the UA be operated at airspeeds greater than the maximum UA operating airspeed recommended by the aircraft manufacturer.

4. The UA must be operated at an altitude of no more than 400 feet above ground level (AGL). Altitude must be reported in feet AGL.

5. The UA must be operated within visual line of sight (VLOS) of the PIC at all times. This requires the PIC to be able to use human vision unaided by any device other than corrective lenses, as specified on the PIC's FAA-issued airman medical certificate or U.S. driver's license.

6. All operations must utilize a visual observer (VO). The UA must be operated within the visual line of sight (VLOS) of the PIC and VO at all times. The VO may be used

to satisfy the VLOS requirement as long as the PIC always maintains VLOS capability. The VO and PIC must be able to communicate verbally at all times; electronic messaging or texting is not permitted during flight operations. The PIC must be designated before the flight and cannot transfer his or her designation for the duration of the flight. The PIC must ensure that the VO can perform the duties required of the VO.

7. This exemption and all documents needed to operate the UAS and conduct its operations in accordance with the conditions and limitations stated in this grant of exemption, are hereinafter referred to as the operating documents. The operating documents must be accessible during UAS operations and made available to the Administrator upon request. If a discrepancy exists between the conditions and limitations in this exemption and the procedures outlined in the operating documents, the conditions and limitations herein take precedence and must be followed. Otherwise, the operator must follow the procedures as outlined in its operating documents. The operator may update or revise its operating documents. It is the operator's responsibility to track such revisions and present updated and revised documents to the Administrator or any law enforcement official upon request. The operator must also present updated and revised documents if it petitions for extension or amendment to this grant of exemption. If the operator determines that any update or revision would affect the basis upon which the FAA granted this exemption, then the operator must petition for an amendment to its grant of exemption. The FAA's UAS Integration Office (AFS–80) may be contacted if questions arise regarding updates or revisions to the operating documents.

8. Any UAS that has undergone maintenance or alterations that affect the UAS operation or flight characteristics, e.g., replacement of a flight critical component, must undergo a functional test flight prior to conducting further operations under this exemption. Functional test flights may only be conducted by a PIC with a VO and must remain at least 500 feet from other people. The functional test flight must be conducted in such a manner so as to not pose an undue hazard to persons and property.

9. The operator is responsible for maintaining and inspecting the UAS to ensure that it is in a condition for safe operation.

10. Prior to each flight, the PIC must conduct a pre-flight inspection and determine the UAS is in a condition for safe flight. The pre-flight inspection must account for all potential discrepancies, e.g., inoperable components, items, or equipment. If the inspection reveals a condition that affects the safe operation of the UAS, the aircraft is prohibited from operating until the necessary maintenance has been performed and the UAS is found to be in a condition for safe flight.

11. The operator must follow the UAS manufacturer's maintenance, overhaul, replacement, inspection, and life limit requirements for the aircraft and aircraft components.

12. Each UAS operated under this exemption must comply with all manufacturer safety bulletins.

13. Under this grant of exemption, a PIC must hold either an airline transport, commercial, private, recreational, or sport pilot certificate. The PIC must also hold a current FAA airman medical certificate or a valid U.S. driver's license issued by a state, the District of Columbia, Puerto Rico, a territory, a possession, or the Federal government. The PIC must also meet the flight review requirements specified in 14 CFR § 61.56 in an aircraft in which the PIC is rated on his or her pilot certificate.

14. The operator may not permit any PIC to operate unless the PIC demonstrates the ability to safely operate the UAS in a manner consistent with how the UAS will be operated under this exemption, including evasive and emergency maneuvers and maintaining appropriate distances from persons, vessels, vehicles and structures. PIC qualification flight hours and currency must be logged in a manner consistent with 14 CFR § 61.51(b). Flights for the purposes of training the operator's PICs and VOs (training, proficiency, and experience-building) and determining the PIC's ability to safely operate the UAS in a manner consistent with how the UAS will be operated under this exemption are permitted under the terms of this exemption. However, training operations may only be conducted during dedicated training sessions. During training, proficiency, and experience-building flights, all persons not essential for flight operations are considered nonparticipants, and the PIC must operate the UA with appropriate distance from nonparticipants in accordance with 14 CFR § 91.119.

15. UAS operations may not be conducted during night, as defined in 14 CFR § 1.1. All operations must be conducted under visual meteorological conditions (VMC). Flights under special visual flight rules (SVFR) are not authorized.

16. The UA may not operate within 5 nautical miles of an airport reference point (ARP) as denoted in the current FAA Airport/Facility Directory (AFD) or for airports not denoted with an ARP, the center of the airport symbol as denoted on the current FAA-published aeronautical chart, unless a letter of agreement with that airport's management is obtained or otherwise permitted by a COA issued to the exemption holder. The letter of agreement with the airport management must be made available to the Administrator or any law enforcement official upon request.

17. The UA may not be operated less than 500 feet below or less than 2,000 feet horizontally from a cloud or when visibility is less than 3 statute miles from the PIC.

18. For tethered UAS operations, the tether line must have colored pennants or streamers attached at not more than 50 foot intervals beginning at 150 feet above the surface of the earth and visible from at least one mile. This requirement for pennants or streamers is not applicable when operating exclusively below the top of and within 250 feet of any structure, so long as the UA operation does not obscure the lighting of the structure.

19. If the UAS loses communications or loses its GPS signal, the UA must return to a pre-determined location within the private or controlled-access property.

20. The PIC must abort the flight in the event of unpredicted obstacles or emergencies.

21. The PIC is prohibited from beginning a flight unless (considering wind and forecast weather conditions) there is enough available power for the UA to conduct the intended operation and to operate after that for at least 5 minutes or with the reserve power recommended by the manufacturer if greater.

22. Air Traffic Organization (ATO) Certificate of Waiver or Authorization (COA). All operations shall be conducted in accordance with an ATO-issued COA. The exemption holder may apply for a new or amended COA if it intends to conduct operations that cannot be conducted under the terms of the enclosed COA.

23. All aircraft operated in accordance with this exemption must be identified by serial number, registered in accordance with 14 CFR part 47, and have identification (N–Number) markings in accordance with 14 CFR part 45, Subpart C. Markings must be as large as practicable.

24. Documents used by the operator to ensure the safe operation and flight of the UAS and any documents required under 14 CFR §§ 91.9 and 91.203 must be available to the PIC at the Ground Control Station of the UAS any time the aircraft is operating. These documents must be made available to the Administrator or any law enforcement official upon request.

25. The UA must remain clear and give way to all manned aviation operations and activities at all times.

26. The UAS may not be operated by the PIC from any moving device or vehicle.

27. All Flight operations must be conducted at least 500 feet from all nonparticipating persons, vessels, vehicles, and structures unless:
    a. Barriers or structures are present that sufficiently protect nonparticipating persons from the UA and/or debris in the event of an accident. The operator must ensure that nonparticipating persons remain under such protection. If a situation arises where nonparticipating persons leave such protection and are within 500 feet of

the UA, flight operations must cease immediately in a manner ensuring the safety of nonparticipating persons; and

b. The owner/controller of any vessels, vehicles or structures has granted permission for operating closer to those objects and the PIC has made a safety assessment of the risk of operating closer to those objects and determined that it does not present an undue hazard.

The PIC, VO, operator trainees or essential persons are not considered nonparticipating persons under this exemption.

28. All operations shall be conducted over private or controlled-access property with permission from the property owner/controller or authorized representative. Permission from property owner/controller or authorized representative will be obtained for each flight to be conducted.

29. Any incident, accident, or flight operation that transgresses the lateral or vertical boundaries of the operational area as defined by the applicable COA must be reported to the FAA's UAS Integration Office (AFS–80) within 24 hours. Accidents must be reported to the National Transportation Safety Board (NTSB) per instructions contained on the NTSB Web site: www.ntsb.gov.

If this exemption permits operations for the purpose of closed-set motion picture and television filming and production, the following additional conditions and limitations apply.

30. The operator must have a motion picture and television operations manual (MPTOM) as documented in this grant of exemption.

31. At least 3 days before aerial filming, the operator of the UAS affected by this exemption must submit a written Plan of Activities to the local Flight Standards District Office (FSDO) with jurisdiction over the area of proposed filming. The 3-day notification may be waived with the concurrence of the FSDO. The plan of activities must include at least the following:
    a. Dates and times for all flights;
    b. Name and phone number of the operator for the UAS aerial filming conducted under this grant of exemption;
    c. Name and phone number of the person responsible for the on-scene operation of the UAS;
    d. Make, model, and serial or N–Number of UAS to be used;
    e. Name and certificate number of UAS PICs involved in the aerial filming;
    f. A statement that the operator has obtained permission from property owners and/or local officials to conduct the filming production event; the list of those who gave permission must be made available to the inspector upon request;
    g. Signature of exemption holder or representative; and

   h. A description of the flight activity, including maps or diagrams of any area, city, town, county, and/or state over which filming will be conducted and the altitudes essential to accomplish the operation.

32. Flight operations may be conducted closer than 500 feet from participating persons consenting to be involved and necessary for the filming production, as specified in the exemption holder's MPTOM.

Unless otherwise specified in this grant of exemption, the UAS, the UAS PIC, and the UAS operations must comply with all applicable parts of 14 CFR including, but not limited to, parts 45, 47, 61, and 91.

This exemption terminates on February 28, 2018, unless sooner superseded or rescinded.

Sincerely,

/s/
John S. Duncan
Director, Flight Standards Service

Enclosure

APPENDIX C

FAA SMALL UAS CERTIFICATE OF REGISTRATION

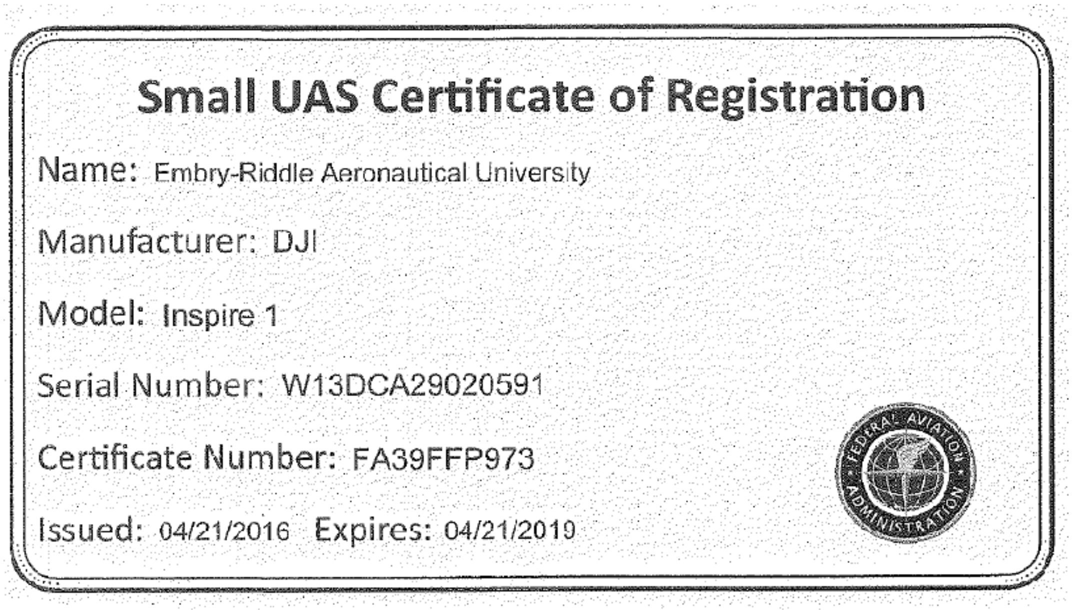

Small UAS Certificate of Registration

Name: Embry-Riddle Aeronautical University

Manufacturer: DJI

Model: Inspire 1

Serial Number: W13DCA29020591

Certificate Number: FA39FFP973

Issued: 04/21/2016 Expires: 04/21/2019

Figure C.1 FAA Small UAS Certificate of Registration

APPENDIX D

DATA LOGGING CODE

D.1 Data logging code

```
#include <SD.h>
#include <SPI.h>
#include <SoftwareSerial.h>


SoftwareSerial GPSModule(3, 1); //Rx, Tx
int updates;
int failedUpdates;
int pos;
int stringplace = 0;
const int variable = 1;

const int ledPin = 13;
String timeUp;
String nmea[15];

void setup() {
  // put your setup code here, to run once:
 Serial.begin(57600);
 GPSModule.begin(9600);

  Serial.print("Initializing SD card...");

  if (!SD.begin(4))
    {
      Serial.println("initialization failed!");
      return;
    }
  Serial.println("initialization done.");

 File logFile = SD.open("Log.csv", FILE_WRITE);
 if (logFile);

  logFile.println(", , ,");
  String header = "Time, Latitude, Hemisphere, Longitude, Hemishpere,
Fix, Altitude(MSL/M), Altitude(WGS84/M), Temperature, Humidity";
  logFile.println(header);
  logFile.close();
  Serial.println(header);

   pinMode(ledPin, OUTPUT);
   pinMode(7, INPUT);

}
void loop()
{
  //int sensorval = digitalRead(7);


//if(sensorval == HIGH)
{
  //while(variable == 1)
```

```
  {

    GPSModule.flush();
    while (GPSModule.available() > 0)
      {
        GPSModule.read();
      }
//GPS gathering time
    if (GPSModule.find("$GPGGA,"))
      {
        String tempMsg = GPSModule.readStringUntil('\n');
        for (int i = 0; i < tempMsg.length(); i++)
          {
            if (tempMsg.substring(i, i + 1) == ",")
              {
                nmea[pos] = tempMsg.substring(stringplace, i);
                stringplace = i + 1;
                pos++;
              }
            if (i == tempMsg.length() - 1)
              {
                nmea[pos] = tempMsg.substring(stringplace, i);
              }
          }
        updates++;
   //for (int i = 0; i < 9; i++)
    {
      //Serial.print(nmea[0]);
      //Serial.println("");
    }
      }
   else
      {
         failedUpdates++;
      }
    stringplace = 0;
    pos = 0;
//Temperature Reading
    int tempvalue; //Create an integer variabl
    int ftemp;
    tempvalue=analogRead(A2);      //Read the analog port 0 and store
the value in val
    float Voltage = tempvalue*((5.0/1023)*10);
    float temp = (-40+(Voltage*10));
    ftemp = ((temp*1.8)+32);
//Humidity Reading
    int humvalue; //Create an integer variabl
    int htemp;
    humvalue=analogRead(A1);      //Read the analog port 0 and store
the value in val
    float HVoltage = humvalue*((5.0/1023)*100);

//Create data string for storing to SD card
//CSV format
```

```
    String dataString = String(nmea[0]) + ", " + String(nmea[1]) + ", "
+ String(nmea[2]) + ", " + String(nmea[3]) + ", " + String(nmea[4]) +
", " + String(nmea[5]) + ", " + String(nmea[8]) + ", " +
String(nmea[10]) + ", " + String(temp) + ", " + String(HVoltage);

//Open a file to write to
    File logFile = SD.open("Log.csv", FILE_WRITE);
    if (logFile)
      {
        logFile.println(dataString);
        logFile.close();
        //Serial.println(dataString);
      }
    Serial.println(dataString);

    delay(500);

  }
  }
 }
```

APPENDIX E

FLIGHT CARDS

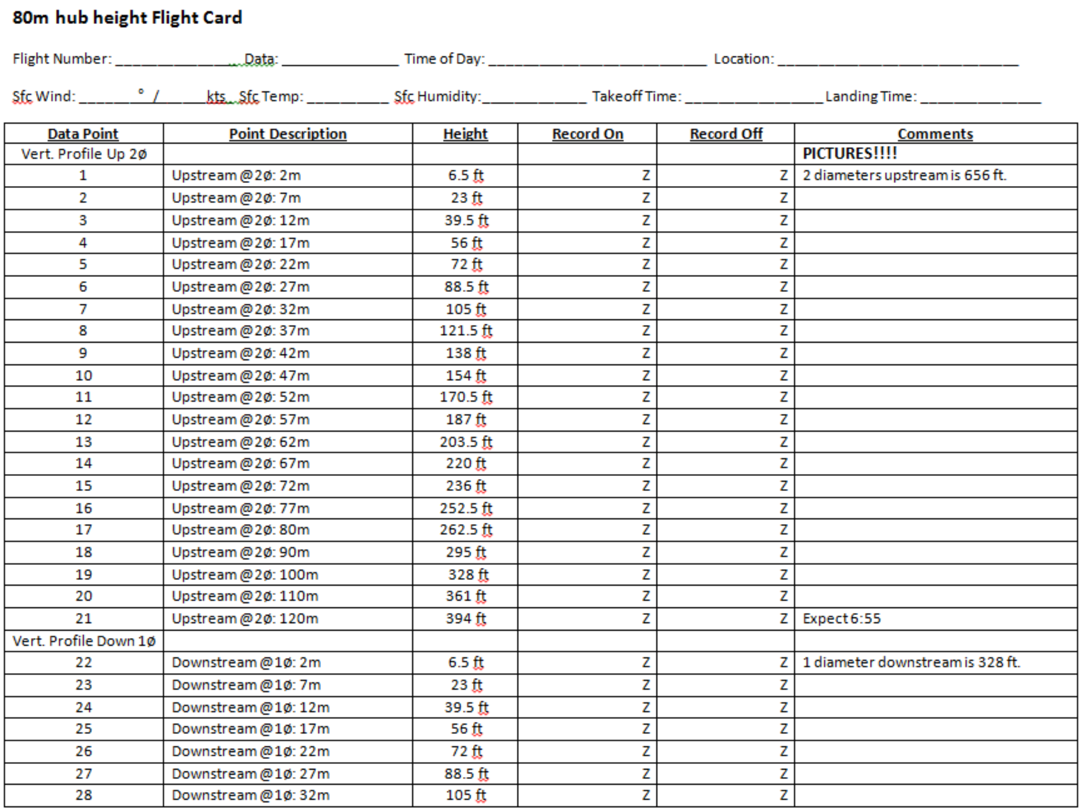

80m hub height Flight Card

Flight Number: _______________ Data: _______________ Time of Day: ____________________________ Location: _______________________________

Sfc Wind: ________° / ______kts. Sfc Temp: __________ Sfc Humidity:____________ Takeoff Time: __________________ Landing Time: _______________

Data Point	**Point Description**	**Height**	**Record On**	**Record Off**	**Comments**
Vert. Profile Up 2ø					**PICTURES!!!!**
1	Upstream @2ø: 2m	6.5 ft	Z	Z	2 diameters upstream is 656 ft.
2	Upstream @2ø: 7m	23 ft	Z	Z	
3	Upstream @2ø: 12m	39.5 ft	Z	Z	
4	Upstream @2ø: 17m	56 ft	Z	Z	
5	Upstream @2ø: 22m	72 ft	Z	Z	
6	Upstream @2ø: 27m	88.5 ft	Z	Z	
7	Upstream @2ø: 32m	105 ft	Z	Z	
8	Upstream @2ø: 37m	121.5 ft	Z	Z	
9	Upstream @2ø: 42m	138 ft	Z	Z	
10	Upstream @2ø: 47m	154 ft	Z	Z	
11	Upstream @2ø: 52m	170.5 ft	Z	Z	
12	Upstream @2ø: 57m	187 ft	Z	Z	
13	Upstream @2ø: 62m	203.5 ft	Z	Z	
14	Upstream @2ø: 67m	220 ft	Z	Z	
15	Upstream @2ø: 72m	236 ft	Z	Z	
16	Upstream @2ø: 77m	252.5 ft	Z	Z	
17	Upstream @2ø: 80m	262.5 ft	Z	Z	
18	Upstream @2ø: 90m	295 ft	Z	Z	
19	Upstream @2ø: 100m	328 ft	Z	Z	
20	Upstream @2ø: 110m	361 ft	Z	Z	
21	Upstream @2ø: 120m	394 ft	Z	Z	Expect 6:55
Vert. Profile Down 1ø					
22	Downstream @1ø: 2m	6.5 ft	Z	Z	1 diameter downstream is 328 ft.
23	Downstream @1ø: 7m	23 ft	Z	Z	
24	Downstream @1ø: 12m	39.5 ft	Z	Z	
25	Downstream @1ø: 17m	56 ft	Z	Z	
26	Downstream @1ø: 22m	72 ft	Z	Z	
27	Downstream @1ø: 27m	88.5 ft	Z	Z	
28	Downstream @1ø: 32m	105 ft	Z	Z	

Figure E.1 Flight test card for 80 meter hub height wind turbines.

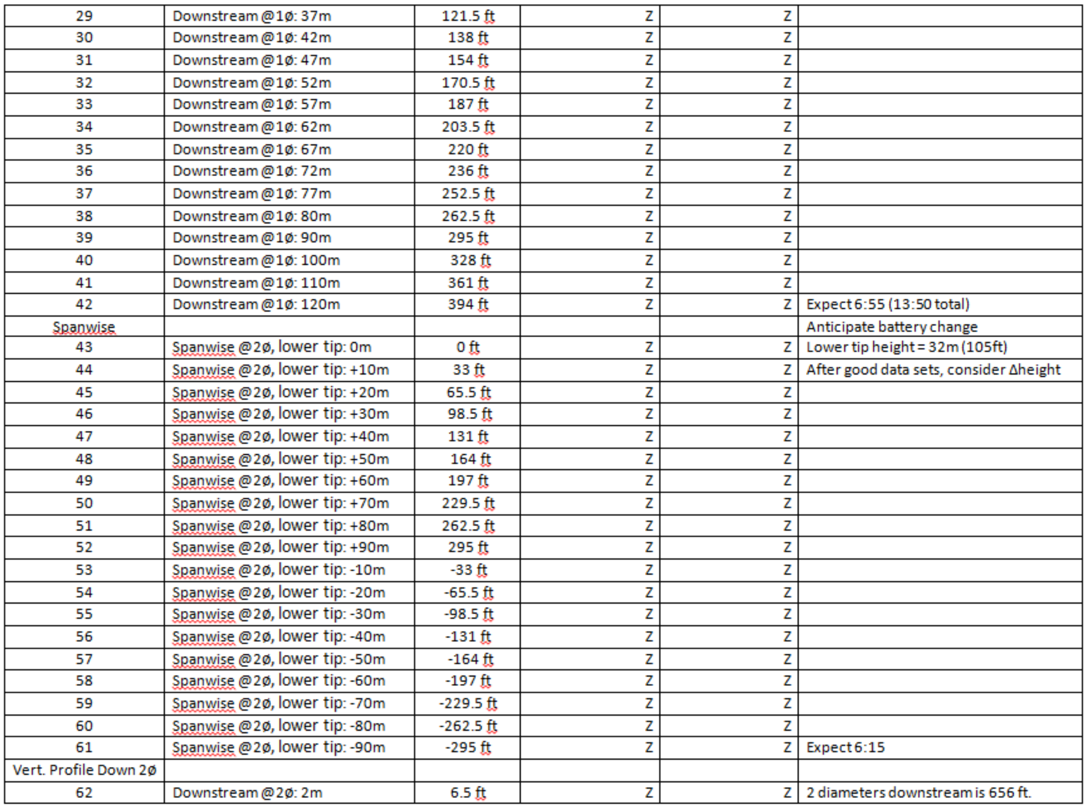

29	Downstream @1ø: 37m	121.5 ft	Z	Z	
30	Downstream @1ø: 42m	138 ft	Z	Z	
31	Downstream @1ø: 47m	154 ft	Z	Z	
32	Downstream @1ø: 52m	170.5 ft	Z	Z	
33	Downstream @1ø: 57m	187 ft	Z	Z	
34	Downstream @1ø: 62m	203.5 ft	Z	Z	
35	Downstream @1ø: 67m	220 ft	Z	Z	
36	Downstream @1ø: 72m	236 ft	Z	Z	
37	Downstream @1ø: 77m	252.5 ft	Z	Z	
38	Downstream @1ø: 80m	262.5 ft	Z	Z	
39	Downstream @1ø: 90m	295 ft	Z	Z	
40	Downstream @1ø: 100m	328 ft	Z	Z	
41	Downstream @1ø: 110m	361 ft	Z	Z	
42	Downstream @1ø: 120m	394 ft	Z	Z	Expect 6:55 (13:50 total)
Spanwise					Anticipate battery change
43	Spanwise @2ø, lower tip: 0m	0 ft	Z	Z	Lower tip height = 32m (105ft)
44	Spanwise @2ø, lower tip: +10m	33 ft	Z	Z	After good data sets, consider Δheight
45	Spanwise @2ø, lower tip: +20m	65.5 ft	Z	Z	
46	Spanwise @2ø, lower tip: +30m	98.5 ft	Z	Z	
47	Spanwise @2ø, lower tip: +40m	131 ft	Z	Z	
48	Spanwise @2ø, lower tip: +50m	164 ft	Z	Z	
49	Spanwise @2ø, lower tip: +60m	197 ft	Z	Z	
50	Spanwise @2ø, lower tip: +70m	229.5 ft	Z	Z	
51	Spanwise @2ø, lower tip: +80m	262.5 ft	Z	Z	
52	Spanwise @2ø, lower tip: +90m	295 ft	Z	Z	
53	Spanwise @2ø, lower tip: -10m	-33 ft	Z	Z	
54	Spanwise @2ø, lower tip: -20m	-65.5 ft	Z	Z	
55	Spanwise @2ø, lower tip: -30m	-98.5 ft	Z	Z	
56	Spanwise @2ø, lower tip: -40m	-131 ft	Z	Z	
57	Spanwise @2ø, lower tip: -50m	-164 ft	Z	Z	
58	Spanwise @2ø, lower tip: -60m	-197 ft	Z	Z	
59	Spanwise @2ø, lower tip: -70m	-229.5 ft	Z	Z	
60	Spanwise @2ø, lower tip: -80m	-262.5 ft	Z	Z	
61	Spanwise @2ø, lower tip: -90m	-295 ft	Z	Z	Expect 6:15
Vert. Profile Down 2ø					
62	Downstream @2ø: 2m	6.5 ft	Z	Z	2 diameters downstream is 656 ft.

Figure E.1 (Continued)

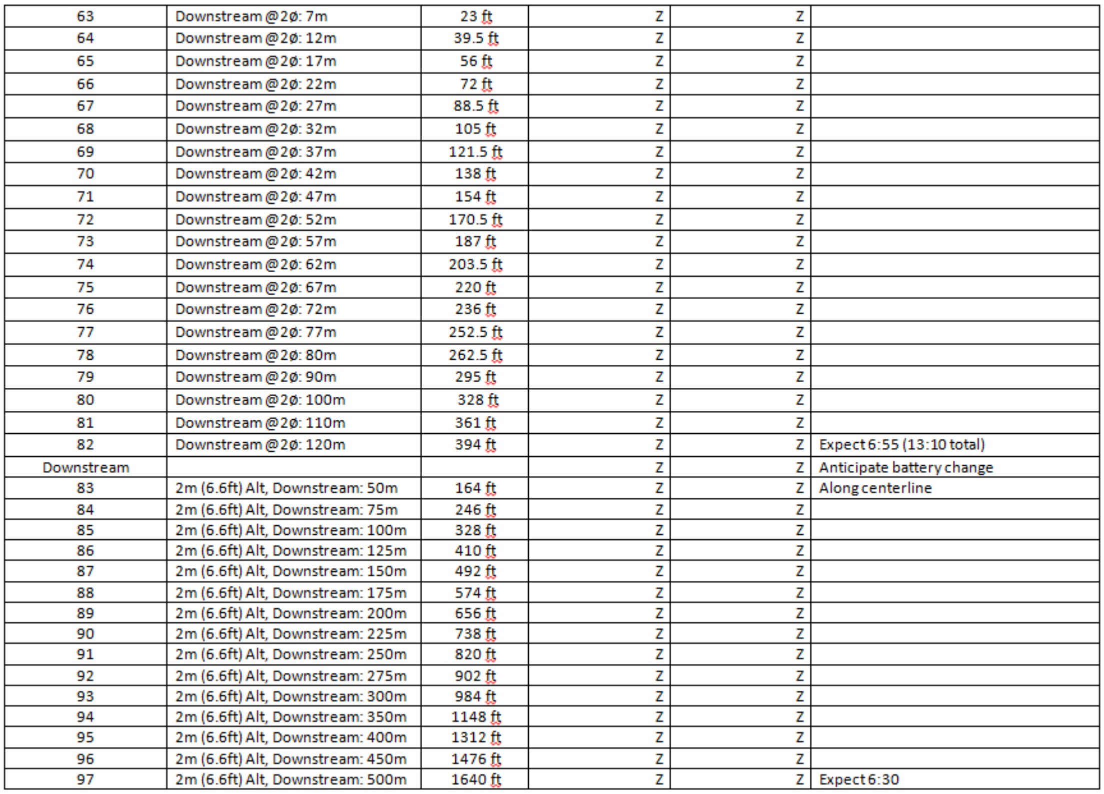

63	Downstream @2ø: 7m	23 ft	Z	Z	
64	Downstream @2ø: 12m	39.5 ft	Z	Z	
65	Downstream @2ø: 17m	56 ft	Z	Z	
66	Downstream @2ø: 22m	72 ft	Z	Z	
67	Downstream @2ø: 27m	88.5 ft	Z	Z	
68	Downstream @2ø: 32m	105 ft	Z	Z	
69	Downstream @2ø: 37m	121.5 ft	Z	Z	
70	Downstream @2ø: 42m	138 ft	Z	Z	
71	Downstream @2ø: 47m	154 ft	Z	Z	
72	Downstream @2ø: 52m	170.5 ft	Z	Z	
73	Downstream @2ø: 57m	187 ft	Z	Z	
74	Downstream @2ø: 62m	203.5 ft	Z	Z	
75	Downstream @2ø: 67m	220 ft	Z	Z	
76	Downstream @2ø: 72m	236 ft	Z	Z	
77	Downstream @2ø: 77m	252.5 ft	Z	Z	
78	Downstream @2ø: 80m	262.5 ft	Z	Z	
79	Downstream @2ø: 90m	295 ft	Z	Z	
80	Downstream @2ø: 100m	328 ft	Z	Z	
81	Downstream @2ø: 110m	361 ft	Z	Z	
82	Downstream @2ø: 120m	394 ft	Z	Z	Expect 6:55 (13:10 total)
Downstream			Z	Z	Anticipate battery change
83	2m (6.6ft) Alt, Downstream: 50m	164 ft	Z	Z	Along centerline
84	2m (6.6ft) Alt, Downstream: 75m	246 ft	Z	Z	
85	2m (6.6ft) Alt, Downstream: 100m	328 ft	Z	Z	
86	2m (6.6ft) Alt, Downstream: 125m	410 ft	Z	Z	
87	2m (6.6ft) Alt, Downstream: 150m	492 ft	Z	Z	
88	2m (6.6ft) Alt, Downstream: 175m	574 ft	Z	Z	
89	2m (6.6ft) Alt, Downstream: 200m	656 ft	Z	Z	
90	2m (6.6ft) Alt, Downstream: 225m	738 ft	Z	Z	
91	2m (6.6ft) Alt, Downstream: 250m	820 ft	Z	Z	
92	2m (6.6ft) Alt, Downstream: 275m	902 ft	Z	Z	
93	2m (6.6ft) Alt, Downstream: 300m	984 ft	Z	Z	
94	2m (6.6ft) Alt, Downstream: 350m	1148 ft	Z	Z	
95	2m (6.6ft) Alt, Downstream: 400m	1312 ft	Z	Z	
96	2m (6.6ft) Alt, Downstream: 450m	1476 ft	Z	Z	
97	2m (6.6ft) Alt, Downstream: 500m	1640 ft	Z	Z	Expect 6:30

Figure E.1 (Continued)

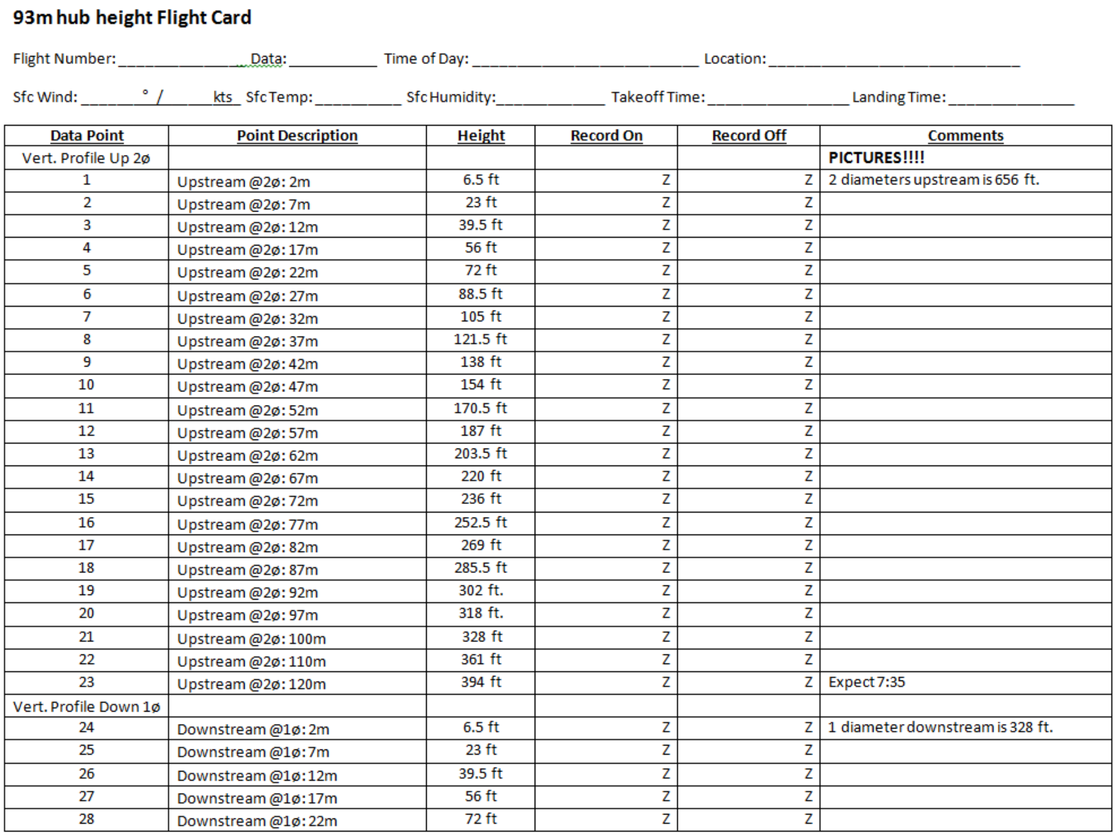

93m hub height Flight Card

Flight Number:______________Data:__________ Time of Day: ___________________________ Location: ______________________________

Sfc Wind: ______° / ______kts Sfc Temp:__________ Sfc Humidity:_____________ Takeoff Time:________________ Landing Time:______________

Data Point	Point Description	Height	Record On	Record Off	Comments
Vert. Profile Up 2ø					**PICTURES!!!!**
1	Upstream @2ø: 2m	6.5 ft	Z	Z	2 diameters upstream is 656 ft.
2	Upstream @2ø: 7m	23 ft	Z	Z	
3	Upstream @2ø: 12m	39.5 ft	Z	Z	
4	Upstream @2ø: 17m	56 ft	Z	Z	
5	Upstream @2ø: 22m	72 ft	Z	Z	
6	Upstream @2ø: 27m	88.5 ft	Z	Z	
7	Upstream @2ø: 32m	105 ft	Z	Z	
8	Upstream @2ø: 37m	121.5 ft	Z	Z	
9	Upstream @2ø: 42m	138 ft	Z	Z	
10	Upstream @2ø: 47m	154 ft	Z	Z	
11	Upstream @2ø: 52m	170.5 ft	Z	Z	
12	Upstream @2ø: 57m	187 ft	Z	Z	
13	Upstream @2ø: 62m	203.5 ft	Z	Z	
14	Upstream @2ø: 67m	220 ft	Z	Z	
15	Upstream @2ø: 72m	236 ft	Z	Z	
16	Upstream @2ø: 77m	252.5 ft	Z	Z	
17	Upstream @2ø: 82m	269 ft	Z	Z	
18	Upstream @2ø: 87m	285.5 ft	Z	Z	
19	Upstream @2ø: 92m	302 ft.	Z	Z	
20	Upstream @2ø: 97m	318 ft.	Z	Z	
21	Upstream @2ø: 100m	328 ft	Z	Z	
22	Upstream @2ø: 110m	361 ft	Z	Z	
23	Upstream @2ø: 120m	394 ft	Z	Z	Expect 7:35
Vert. Profile Down 1ø					
24	Downstream @1ø: 2m	6.5 ft	Z	Z	1 diameter downstream is 328 ft.
25	Downstream @1ø: 7m	23 ft	Z	Z	
26	Downstream @1ø: 12m	39.5 ft	Z	Z	
27	Downstream @1ø: 17m	56 ft	Z	Z	
28	Downstream @1ø: 22m	72 ft	Z	Z	

Figure E.2 Flight test card for 93 meter hub height wind turbines

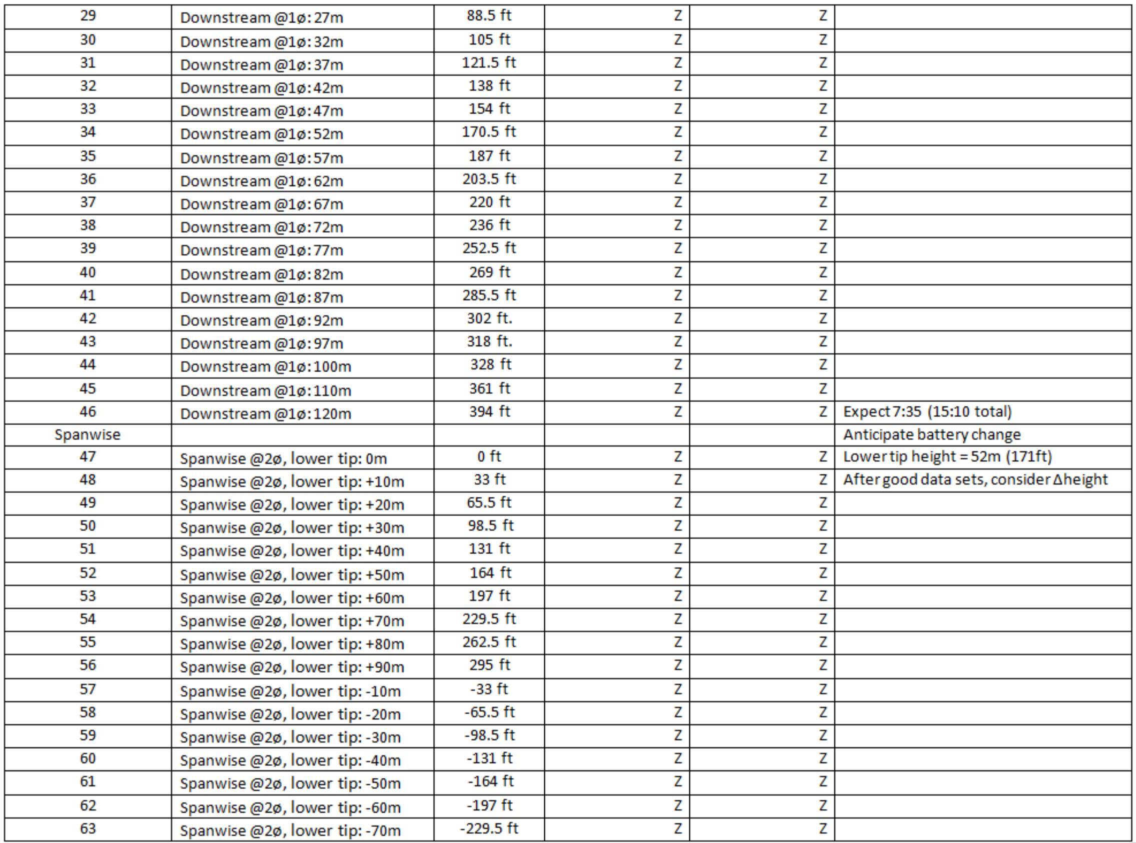

29	Downstream @1ø: 27m	88.5 ft	Z	Z	
30	Downstream @1ø: 32m	105 ft	Z	Z	
31	Downstream @1ø: 37m	121.5 ft	Z	Z	
32	Downstream @1ø: 42m	138 ft	Z	Z	
33	Downstream @1ø: 47m	154 ft	Z	Z	
34	Downstream @1ø: 52m	170.5 ft	Z	Z	
35	Downstream @1ø: 57m	187 ft	Z	Z	
36	Downstream @1ø: 62m	203.5 ft	Z	Z	
37	Downstream @1ø: 67m	220 ft	Z	Z	
38	Downstream @1ø: 72m	236 ft	Z	Z	
39	Downstream @1ø: 77m	252.5 ft	Z	Z	
40	Downstream @1ø: 82m	269 ft	Z	Z	
41	Downstream @1ø: 87m	285.5 ft	Z	Z	
42	Downstream @1ø: 92m	302 ft.	Z	Z	
43	Downstream @1ø: 97m	318 ft.	Z	Z	
44	Downstream @1ø: 100m	328 ft	Z	Z	
45	Downstream @1ø: 110m	361 ft	Z	Z	
46	Downstream @1ø: 120m	394 ft	Z	Z	Expect 7:35 (15:10 total)
Spanwise					Anticipate battery change
47	Spanwise @2ø, lower tip: 0m	0 ft	Z	Z	Lower tip height = 52m (171ft)
48	Spanwise @2ø, lower tip: +10m	33 ft	Z	Z	After good data sets, consider Δheight
49	Spanwise @2ø, lower tip: +20m	65.5 ft	Z	Z	
50	Spanwise @2ø, lower tip: +30m	98.5 ft	Z	Z	
51	Spanwise @2ø, lower tip: +40m	131 ft	Z	Z	
52	Spanwise @2ø, lower tip: +50m	164 ft	Z	Z	
53	Spanwise @2ø, lower tip: +60m	197 ft	Z	Z	
54	Spanwise @2ø, lower tip: +70m	229.5 ft	Z	Z	
55	Spanwise @2ø, lower tip: +80m	262.5 ft	Z	Z	
56	Spanwise @2ø, lower tip: +90m	295 ft	Z	Z	
57	Spanwise @2ø, lower tip: -10m	-33 ft	Z	Z	
58	Spanwise @2ø, lower tip: -20m	-65.5 ft	Z	Z	
59	Spanwise @2ø, lower tip: -30m	-98.5 ft	Z	Z	
60	Spanwise @2ø, lower tip: -40m	-131 ft	Z	Z	
61	Spanwise @2ø, lower tip: -50m	-164 ft	Z	Z	
62	Spanwise @2ø, lower tip: -60m	-197 ft	Z	Z	
63	Spanwise @2ø, lower tip: -70m	-229.5 ft	Z	Z	

Figure E.2 (Continued)

64	Spanwise @2ø, lower tip: -80m	-262.5 ft	Z	Z	
65	Spanwise @2ø, lower tip: -90m	-295 ft	Z	Z	Expect 6:15
Vert. Profile Down 2ø					
66	Downstream @2ø: 2m	6.5 ft	Z	Z	2 diameters downstream is 656 ft.
67	Downstream @2ø: 7m	23 ft	Z	Z	
68	Downstream @2ø: 12m	39.5 ft	Z	Z	
69	Downstream @2ø: 17m	56 ft	Z	Z	
70	Downstream @2ø: 22m	72 ft	Z	Z	
71	Downstream @2ø: 27m	88.5 ft	Z	Z	
72	Downstream @2ø: 32m	105 ft	Z	Z	
73	Downstream @2ø: 37m	121.5 ft	Z	Z	
74	Downstream @2ø: 42m	138 ft	Z	Z	
75	Downstream @2ø: 47m	154 ft	Z	Z	
76	Downstream @2ø: 52m	170.5 ft	Z	Z	
77	Downstream @2ø: 57m	187 ft	Z	Z	
78	Downstream @2ø: 62m	203.5 ft	Z	Z	
79	Downstream @2ø: 67m	220 ft	Z	Z	
80	Downstream @2ø: 72m	236 ft	Z	Z	
81	Downstream @2ø: 77m	252.5 ft	Z	Z	
82	Downstream @2ø: 82m	269 ft	Z	Z	
83	Downstream @2ø: 87m	285.5 ft	Z	Z	
84	Downstream @2ø: 92m	302 ft.	Z	Z	
85	Downstream @2ø: 97m	318 ft.	Z	Z	
86	Downstream @2ø: 100m	328 ft	Z	Z	
87	Downstream @2ø: 110m	361 ft	Z	Z	
88	Downstream @2ø: 120m	394 ft	Z	Z	Expect 7:35 (13:50 total)
Downstream			Z	Z	Anticipate battery change
89	2m (6.6ft) Alt, Downstream: 50m	164 ft	Z	Z	Along centerline
90	2m (6.6ft) Alt, Downstream: 75m	246 ft	Z	Z	
91	2m (6.6ft) Alt, Downstream: 100m	328 ft	Z	Z	
92	2m (6.6ft) Alt, Downstream: 125m	410 ft	Z	Z	
93	2m (6.6ft) Alt, Downstream: 150m	492 ft	Z	Z	
94	2m (6.6ft) Alt, Downstream: 175m	574 ft	Z	Z	
95	2m (6.6ft) Alt, Downstream: 200m	656 ft	Z	Z	
96	2m (6.6ft) Alt, Downstream: 225m	738 ft	Z	Z	
97	2m (6.6ft) Alt, Downstream: 250m	820 ft	Z	Z	
98	2m (6.6ft) Alt, Downstream: 275m	902 ft	Z	Z	
99	2m (6.6ft) Alt, Downstream: 300m	984 ft	Z	Z	
100	2m (6.6ft) Alt, Downstream: 350m	1148 ft	Z	Z	
101	2m (6.6ft) Alt, Downstream: 400m	1312 ft	Z	Z	
102	2m (6.6ft) Alt, Downstream: 450m	1476 ft	Z	Z	
103	2m (6.6ft) Alt, Downstream: 500m	1640 ft	Z	Z	Expect 6:30

Figure E.2 (Continued)

APPENDIX F

GLOSSARY OF TERMS

Capacity factor:	The average power generated divided by the rated peak power [103].
Capping inversion:	A statically stable layer at the top of the atmospheric boundary layer [104].
Civil twilight:	The period between astronomical sunrise or sunset and the time when the sun's unrefracted center is at an elevation of -6° [104].
Cultivar:	A plant variety.
Entrainment:	The mixing of environmental air into a preexisting organized air current [104].
Inversion:	A departure from the usual decrease of temperature with altitude [104].
Lapse rate:	The decrease of an atmospheric variable with height [104].
Latent heat:	The specific enthalpy difference between two phases of a substance at the same temperature [104].
Mesoscale:	Pertaining to atmospheric phenomenon having horizontal scales ranging from a few to several hundred kilometers [104].
Mixing ratio:	The ratio of the mass of a variable atmospheric constituent to the mass of dry air [104].
Neutral atmosphere:	An atmosphere in which potential temperature is constant with altitude [6].

Potential temperature:	The temperature that an unsaturated parcel of dry air would have if brought adiabatically and reversibly from its initial state to a standard pressure, typically 1000 mb [104].
Relative humidity:	The ratio of vapor pressure to the saturation vapor pressure with respect to water [104].
Sensible heat:	The outcome of heating a surface without evaporating water from it [104].
Sounding:	A vertical penetration of the atmosphere for scientific observation [104].
Stable atmosphere:	An atmosphere in which potential temperature increases with altitude [6].
Unstable atmosphere:	An atmosphere in which potential temperature increases with altitude [6].
Virtual potential temperature:	The theoretical potential temperature of dry air that would have the same density as moist air [104].